Wrocław University of Technology
Centre of Advanced Materials and Nanotechnology

Materials Science
Poland

Vol.24 • No. 2/1 • 2006

Oficyna Wydawnicza Politechniki Wrocławskiej

Materials Science is an interdisciplinary journal devoted to experimental and theoretical research into the synthesis, structure, properties and applications of materials.

Among the materials of interest are:

- glasses and ceramics
- sol-gel materials
- photoactive materials (including materials for nonlinear optics)
- laser materials
- photonic crystals
- semiconductor micro- and nanostructures
- piezo-, pyro- and ferroelectric materials
- high-T_c superconductors
- magnetic materials
- molecular materials (including polymers) for use in electronics and photonics
- novel solid phases
- other novel and unconventional materials

The broad spectrum of the areas of interest reflects the interdisciplinary nature of materials research. Papers covering the modelling of materials, their synthesis and characterisation, physicochemical aspects of their fabrication, properties and applications are welcome. In addition to regular papers, the journal features issues containing conference papers, as well as special issues on key topics in materials science.

Materials Science is published under the auspices of the Centre of Advanced Materials and Nanotechnology of the Wrocław University of Technology, in collaboration with the Institute of Low Temperatures and Structural Research of the Polish Academy of Sciences and the Wrocław University of Economics.

All accepted papers are placed on the Web page of the journal and are available at the address:
http://MaterialsScience.pwr.wroc.pl

Materials Science is abstracted/indexed in: Chemical Abstracts; Materials Science Citation Index; Science Citation Index Expanded.

The Journal is supported by the State Committee for Scientific Research

Editorial Office

Tomasz Fałat
Karol Langner

Printed in Poland

Drukarnia Oficyny Wydawniczej Politechniki Wrocławskiej
Zam. nr 436/2006.

Contents

Materials Science-Poland, Vol. 24, No. 2/1, 2006

Experimental investigation of the friction coefficient between aluminium and steel

M. JAVADI[1], M. TAJDARI[2*]

Islamic Azad University, Tehran South Branch, Iran

[2]Faculty of Material and Manufacturing Technologies,
Malek Ashtar University of Technology, Tehran, Iran

The coefficient of friction for steel–aluminium contact surfaces has been determined. The test was conducted by using a testing machine active on the basis of the twist-compression test. A flat plate of aluminium was placed under pressure between two steel dies. One of the dies (the upper one) was capable of rotating while the other (the lower one) was stationary and attached to a load cell that was used for measuring the torque and force on the flat plate. By using a strain bridge data logger, the coefficient of friction can be found within 0.75-second intervals. The results show that the friction coefficient for steel-aluminium interfaces started at an initial value of 0.2, increased to almost 0.8 in the elastic region, and then decreased to the value of 0.6 in the plastic region.

Key words: *friction; coefficient; steel; aluminium*

1. Introduction

The coefficient of friction is one of the parameters describing the amount of resistance to the relative motion of two sliding objects. Historically, Leonardo Da Vinci (1508) showed that friction force was proportional to load [1], and Amonton (1700) formulated the relationship [2] that shear stress is proportional to normal stress by the coefficient of friction.

The earliest attempts to explain friction were based on interactions of surface asperities. It is now widely accepted, however, that although mechanical interactions play their part, the high coefficient of friction seen in clean environments may only be explained in terms of adhesion between contacting asperities. From this point of view,

[*]Corresponding author, e-mail: tajdari@yahoo.com

two well-known theories of friction have been introduced [3]: adhesive theory of friction and junction growth theory.

With the assumptions made by the adhesive theory of friction, the value of the coefficient of friction, μ, will be nearly equal to 0.2. Contaminant films will lead to even lower values of μ. In high vacuum conditions, experimentally determined values of the friction coefficient of six or more have been recorded, which clearly cannot be explained by a simple model. It is this discrepancy between experiment and theory that led to junction growth theory [3].

The principal error in the simple adhesive theory lays in the oversimplification of the laws governing plastic contact. The problem is essentially that of defining a yield criterion in a three-dimensional stress system, and may be treated within the classical plasticity theory. It is not acceptable to consider the normal and tangential stresses separately. The governing equation for the coefficient of friction in this theory is assumed to be:

$$\mu = \frac{\tau}{\sigma} = \frac{m_c}{\left[\alpha(1-m_c^2)^{1/2}\right]} \tag{1}$$

where τ is tangential stress due to friction, σ is normal stress at the area of contact, α is a constant determined by the asperity geometry and m_c is the friction factor. The relationship shows that any value between zero and infinity may be obtained merely by changing the value of m_c. For clean surfaces, m_c will tend to unity and μ to infinity.

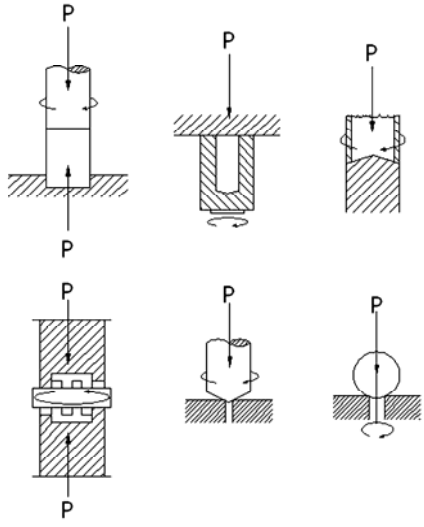

Fig. 1. Various types of twist-compression tests

Several types of experimental methods have been employed to find the friction coefficient, most of them [4] using pressure pins [5], pin on desk test [6] and twist-compression test.

In various forms of the twist-compression test [6] (Fig. 1), normal pressure is combined with continued sliding over the same surface area by rotation of a die or the specimen. Thus, the coefficient of friction is calculated by:

$$\mu = \frac{T}{rN} \tag{2}$$

where T is the torque applied, N is the normal force, and r is the mean radius.

In the following section, a new form of this test is introduced by a new, patented apparatus [7].

2. Experimental procedure

A new testing machine has been designed and made on the basis of the twist-compression test, as shown in Figure 2 [7].

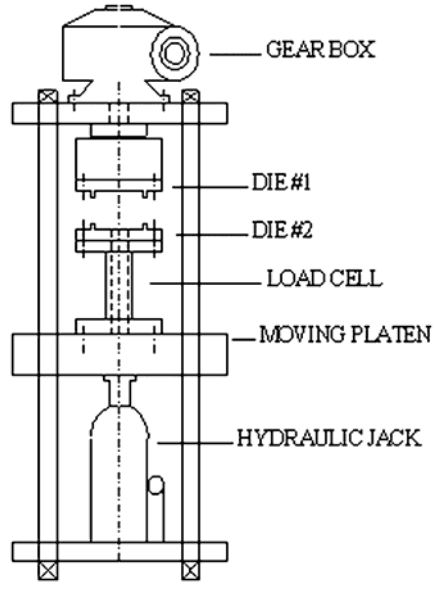

Fig. 2. Testing apparatus [7]

Although the basis of this testing apparatus is twist-compression, a new configuration of applying the load and torque are used (Fig. 3), which has not been introduced by the other configurations shown in Figure 1.

A flat aluminium plate 1 mm thick, with a yield stress of 210 MPa, is placed between two hardened steel dies (die #1 and die #2). Each die has an annular shaped edge 1 mm thick and with a mean radius of 30 mm. The aluminium plate is pressed between two dies by using a hydraulic jack. At the same time, die #1 is rotated by means of a gearbox, while the pressure is increased by the hydraulic jack and die #2 is

rotationally fixed, and the load cell attached to it will measure the applied normal force and torque applied. The measured torque is certainly due to frictional load transferred from the upper to the lower die. Since the annular shaped edge has a diameter larger than 20 times its thickness, it is supposed that it will apply a uniform, normal, and shear stress on the aluminium plate. The torque is transferred by the plate to die #2 with almost no error, and its value is equal to the shear (friction) force multiplied by the mean radius of the annular shaped edge. Equation (2) can be used for computing the friction coefficient.

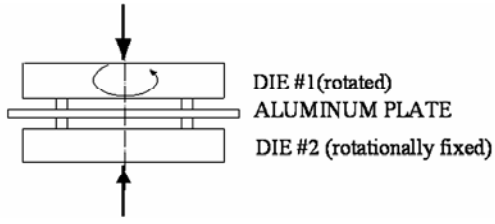

Fig. 3. Configuration of the applied torsional and normal load

Two 45 degree strain gauge rosettes are installed onto the load cell which can measure the load and torque applied to the plate. The load cell is connected to a strain-measuring device, TQ E31 strain bridge data logger which sends the measured strains to a computer by an RS232 connection. A complete strain read-out takes approximately 0.75 sec. The load cell was calibrated for the applied force and torque. By using a calibration curve and applying simple formulas, the normal and shear stress were found. The coefficient of friction is found by simply dividing the shear stress by the normal stress. It must be noted that both shear and normal stresses are apparent stresses. Before each test, the plate and dies were carefully cleaned and degreased with acetone. For preventing the error due to die pick-up after each test, the dies were smoothed with 400 grid abrasive paper in order to form a uniform surface.

3. Results

The results of shear stress versus normal stress and of the friction coefficient versus normal stress are shown for several tests in Figures 4 and 5, respectively. The stresses are obtained simply by dividing the load by the area of contact of the annular shaped edge. For calculating the friction coefficient, Equation (2) was used. The friction load was calculated by dividing the torque measured with the load cell by the mean radius of annular shaped edge.

It can be seen from Figure 4 that the shear stress dependence on the normal stress exhibits three regions. The first region (at low normal stresses) has a low slope which increases (region two) until the shear stress becomes constant (region three).

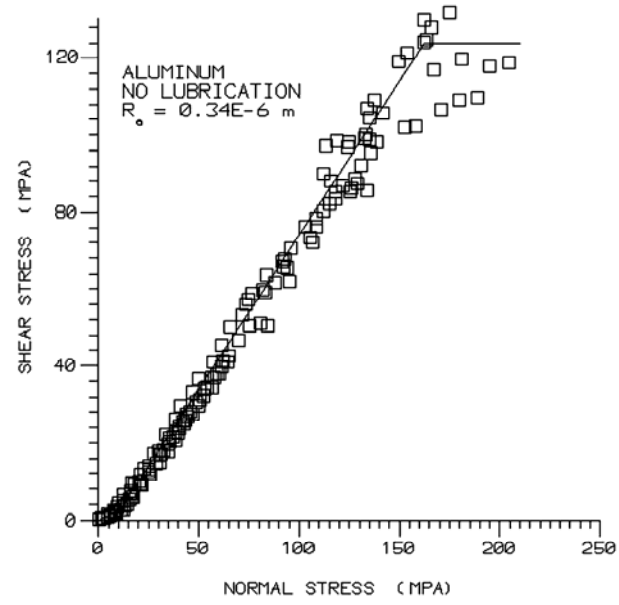

Fig. 4. Experimental results of shear stress vs. normal stress

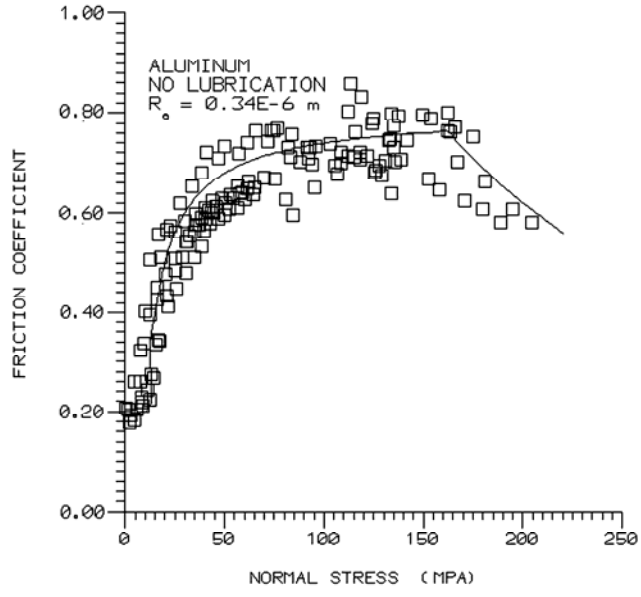

Fig. 5. Experimental results of the friction coefficient vs. normal stress

In Figure 5, it can be seen that the coefficient of friction starts with an initial value of 0.2, and then increases to a maximum of 0.8. After that, it decreases to 0.6 at the highest normal stresses applied in our experiments.

An initial value of 0.2 for the coefficient of friction has been reported by several researchers [8, 9], while a high value of 1.2 has been reported for steady state conditions [10]. The experiments showed that at low normal stresses the adhesive theory of friction can be used, while for higher normal stresses the junction growth theory must be applied due to a higher value of m_c.

For the third region, in which μ decreases, the coefficient of friction follows the formula:

$$\mu = \frac{k}{\sigma} \tag{3}$$

Although τ in Eq. (3) reached the value k, σ did not reach the yield stress. Therefore, when σ equals σ_y (yield stress), the coefficient of friction tends to 0.6. For higher normal stress, for instance $3\sigma_y$ at forging, the coefficient of friction reaches 0.2, in accordance with the data of Van Rooyen and Backofen [5].

References

[1] HOCKETT J.F., Int. J. Mech. Sci., 9 (1967), 233.
[2] KUMAR S., *Principle of Metal Working*, Oxford and IBH Publishing Co., New Delhi, 1976.
[3] MITCHELL L.A., OSGOOD C., Wear, 40 (1976), 203.
[4] MALE A.T., COCKCROFT M.G., J. Inst. Metals, 93 (1964), 38.
[5] VAN ROYEN G.T., BACKOFEN W.A., Int. J. Mech. Sci., 1 (1960), 1.
[6] SCHEY J.A., *Tribology in Metalworking: Friction, Lubrication and Wear*, American Society for Metals Metals Park, OH(1983).
[7] Patent No. 29326, 9 February 2004, Iran.
[8] SUCH N.P., SIN H.C., Wear, 69 (1981), 91.
[9] MAHDAVIAN S.M., MAI Y.W., COTTEREL B., Wear, 82 (1982), 221.
[10] RABINOWICZ E., *Friction and Wear of Materials*, Wiley, New York, 1995.

Received 11 April 2005
Revised 18 June 2005

Materials Science-Poland, Vol. 24, No. 2/1, 2006

Cobalt nanoparticles processed by thermal decomposition of metal-containing monomers

E. SÓWKA[1], M. LEONOWICZ[1*], B. ANDRZEJEWSKI[2],
A. D. POMOGAILO[3], G. I. DZHARDIMALIEVA[3]

[1]Faculty of Materials Science and Engineering, NanoCentre,
Warsaw University of Technology, Wołoska 145, 02-507 Warsaw, Poland

[3]Institute of Molecular Physics, Polish Academy of Sciences,
M. Smoluchowskiego 17, 60-179 Poznań, Poland

[3]Institute of Chemical Physics Russian Academy of Sciences, Chernogolovka, Russia

Polymer matrix ferromagnetic nanocomposites, containing Co nanocrystallites, were processed by an innovative fabrication method that uses the frontal polymerisation of cobalt acrylamid complexes, followed by subsequent thermolysis at 873 and 1073 K. The thermolysis products were in the form of irregular powder particles, with a broad size distribution, from 10 up to 300 μm. The powder particles contained nanocrystallites of Co with a mean size in the range 12–15 nm, depending on the thermolysis temperature. The hysteresis loops recorded for materials processed at 873 and 1073 K proved that coercivity depends on the processing temperature and very slightly on the measurement temperature. The thermolysis product, processed at 873 K, showed soft magnetic properties. The particles were randomly distributed and their size and agglomeration could be controlled by the processing variables.

Key words: cobalt nanoparticles; ferromagnetic nanocomposite; magnetic nanostructure

1. Introduction

Nanoparticles exhibit unique physical properties due to surface or quantum-size effects. Particular attention has recently been focused on magnetic nanoparticles and substantial progress has been achieved in this field. This is mainly due to advances in processing methods and the development of characterization techniques. Substantial achievements in the field made it possible to produce metallic or oxide particles embedded in various organic or inorganic matrices. In those systems, such phenomena as

[*]Corresponding author, e-mail: mkl@inmat.pw.edu.pl

giant magnetoresistance, a strong magnetocaloric effect and many others have been found. The composites containing cobalt nanoparticles focus particular attention due to their potential applications in high-density digital magnetic recording. As a principle, the magnetic recording material should combine ferromagnetic particles of sufficiently high coercivity to prevent demagnetisation, uniformly distributed in a non-magnetic matrix. Magnetic Co nanoparticles have been investigated in a number of works [1–10]. A general conclusion, however, is that their properties strongly depend on the processing method and parameters applied.

Generally, all processing techniques base on the idea of encapsulating metallic nanoparticles in a protective stabilising preventing their oxidation. The material most often employed is carbon, however polymeric insulating layers are also very common. Recently, spherical cobalt nanoparticles, encapsulated in carbon shells with the sizes of 10–100 nm, were prepared using arc discharge between carbon electrodes in a He atmosphere, with the anode filled with cobalt [11]. Boron and cobalt powders were exposed to a mixture of H_2 and NH_3 gases at 1073 K for 3 hours in order to prepare 20–60 nm Co particles, covered with 5 nm thick BN layers [12]. Widely used is also the deposition of Co nanoparticles on substrates. An example of this method is low-energy cluster beam deposition (LECBD), which was applied for the preparation of 3 nm Co nanoparticles on niobium foil [13]. One of the most promising routes for processing nanomaterials with stable structures and properties is nanoparticle synthesis in various matrices. Using this method, self-aggregated nanoparticles of Co in perfluorinated sulfo-cation membrane were prepared by the ion-exchange method. The Co crystallites had a mean radius of 3.8 nm and exhibited superparamagnetic properties with a blocking temperature between 800 and 300 K, depending on the Co concentration [14]. Particles 4 nm in radius were also obtained by thermal decomposition of Co formate in a polyethylene melt in mineral oil. In this case, the blocking temperature was above 600 K [15]. This fact points to a substantial influence of the processing method and resulting concentration of particles, their shape, agglomeration, etc. on physical magnetic properties. An extended review of the processing methods used for Co nanoparticles can be found in [16].

In the current study, nanocomposites containing Co nanoparticles were prepared by frontal polymerisation of acrylamide (AAm) monomers and subsequent thermolysis. This process generally comprises three stages: (i) the formation of an AAm metal nitrate complex by replacing the water of crystallization in crystal hydrates by AAm molecules, (ii) frontal polymerisation of acrylamide monomers, (iii) conversion of the polymer into a nanocomposite by thermolysis. In the last stage, nanoparticles of metals or their oxides, embedded in a stabilizing polymer matrix, are formed.

2. Experimental

The acrylamide metal nitride complex, $[Co(CH_2{=}CHCONH_2)_4(H_2O)_2]^{2+}$, was obtained by a substitution reaction of crystalline inorganic hydrate by acrylamide. Fron-

tal polymerisation of the Co acrylamide complex was carried out at atmospheric pressure and in air. The initiation temperature was 433 K, and further polymerisation occurred at 483 K, with the front velocity equal to $4.8 \cdot 10^{-2}$ cm/s. The process of frontal polymerisation is accompanied by melting of the monomer. The melting and formation of the polymer matrix promote the encapsulation of nitrite groups and prevent their further decay.

Co-containing nanocomposites are formed in the process of thermolysis of the polymeric matrix. The thermolysis was carried out in a self-generated atmosphere at temperatures of 873 K and 1073 K. The procedures applied to the specimens are summarized in Table 1. The thermolysis products were cooled slowly in the reactor to room temperature. The solid products, formed during thermolysis, consisted of cobalt nanoparticles and an amorphous matrix which protected the metal crystallites from oxidation. EDS analysis of the amorphous matrix revealed the presence of carbon, nitrogen, and oxygen atoms. Further studies of this product are in progress. A more detailed description of the processing route, as well as the products, can be found in [17].

Table 1. Characteristics of the studied specimens

Specimen number	Processing history
1	acrylamide complex formation – monomer
2	acrylamide complex formation – monomers; frontal polymerisation of the monomer
3	acrylamide complex formation – monomers; frontal polymerisation of the monomer thermolysis of the polymer at 873 K for 95 min
4	acrylamide complex formation – monomers; frontal polymerisation of the monomer thermolysis of the polymer at 1073 K for 120 min

The structures of the materials after all processing stages were studied using X-ray diffraction (Philips X-pert, Cu-Kα). The crystallite size was evaluated from the line broadening of the X-ray peaks using the Scherrer method. The microstructure was studied with a Hitachi S-3500N scanning electron microscope and high resolution JEM 3010 transmission electron microscope. The hysteresis loops were recorded at temperatures of 50, 100 and 250 K using a Faraday balance. Zero-field-cooled (ZFC) and field-cooled (FC) magnetisation curves were studied versus temperature in the field of 5×10^{-3} T.

3. Results and discussion

Acrylamide monomers of Co (II) exhibit a complex crystalline structure (Fig. 1a), composed of octahedral cations $[Co(CH_2{=}CHCONH_2)_4(H_2O)_2]^{2+}$ of $\bar{1}$ symmetry and NO_3^- anions interconnected by a system of hydrogen bonds [19].

After frontal polymerisation, the colour of the specimen changed from pink to dark cherry. The process led to the decomposition of the crystalline structure and amorphisation of the material (Fig. 1b), accompanied by a mass loss. It is believed that the starting monomers initially lose one water molecule, leading to the hydrate. The loss of a second water molecule promotes the formation of the anhydrous phase and finally the polymerisation of the material [17].

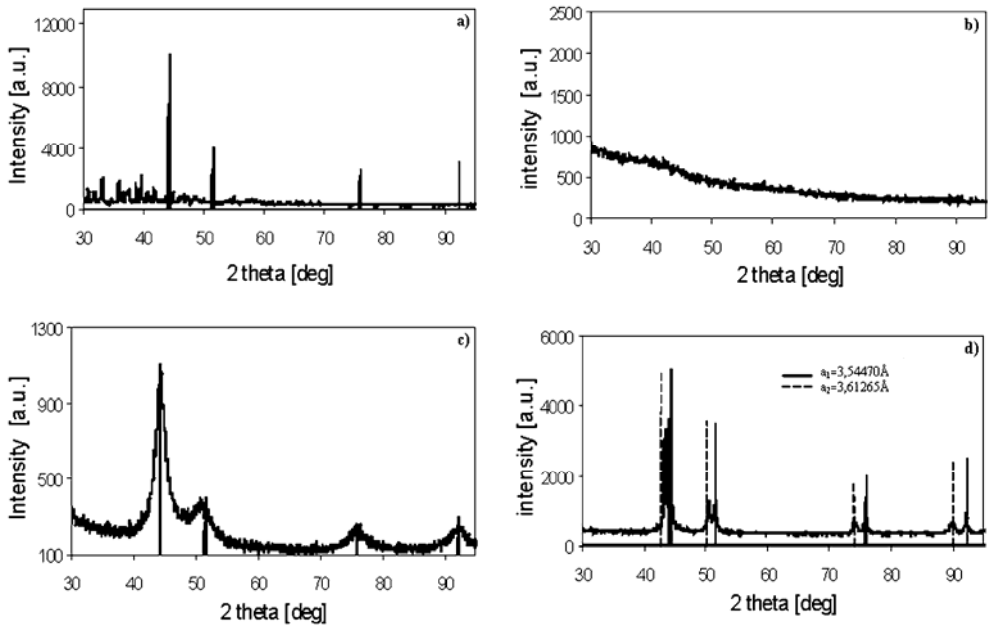

Fig. 1. X-ray patterns of: a) $[Co(CH_2{=}CHCONH_2)_4(H_2O)_2]^{2+}$ complex, (specimen 1), b) the material after frontal polymerisation (specimen 2), c) the material after thermolysis at 873 K (specimen 3), d) the material after thermolysis at 1073 K (specimen 4)

The thermolysis dramatically changes the structure of the material. Distinct crystalline reflections appeared in the pattern. The spectra obtained at various thermolysis temperatures were somewhat different, however. The diffraction pattern for the specimen thermolysed at 873 K matched well the FCC cobalt lines, with the lattice parameter a_1 = 3.54470 Å (Fig. 1c). The material thermolysed at 1073 K showed two coexisting types of metallic cobalt, both having a FCC structure, with lattice parameters a_1 = 3.54470 Å and a_2 = 3.61265 Å, respectively (Fig. 1d). The formation of FCC cobalt nanocrystallites has been reported by several authors [20, 21].

Thermolysis products were in the form of irregular powder particles exhibiting high porosity and a broad distribution of sizes, ranging from 10 to 300 μm (Fig. 2).

TEM images gave a more detailed insight into the microstructure and morphology of the nanocomposites (Fig. 3). The crystallites obtained at the thermolysis temperature of 873 K showed individual spherical particles with a quite uniform size distribution between 12 and 15 nm. Increasing thermolysis temperature resulted in a partial

coarsening of the microstructure, which led to the appearance of some amount of large crystallites (over 20 nm) present together with small 12 nm particles.

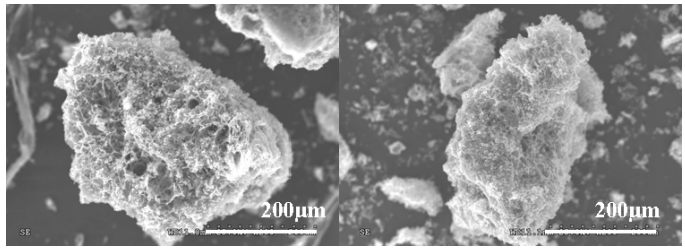

Fig. 2. SEM microstructures of powder particles obtained by thermolysis of frontally polymerised monomers (specimen 3)

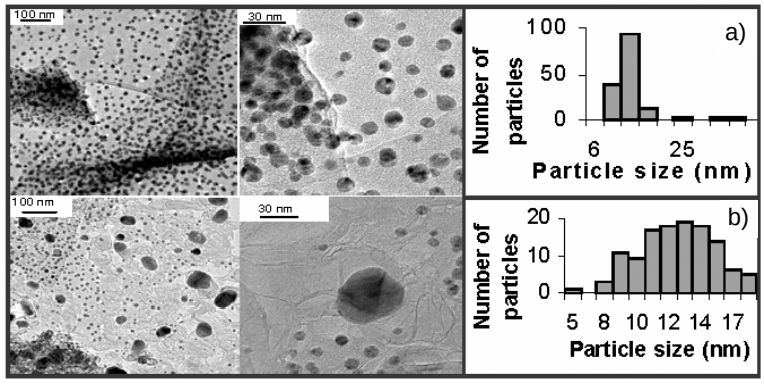

Fig. 3. TEM microstructures of nanocomposites obtained by thermolysis of frontally polymerised material at different temperatures: a) 873 K (specimen 3) and b) 1073 K (specimen 4)

The crystallites are embedded in a matrix consisting mostly of carbon which protects them from oxidation. The structure of the matrix is currently under investigation.

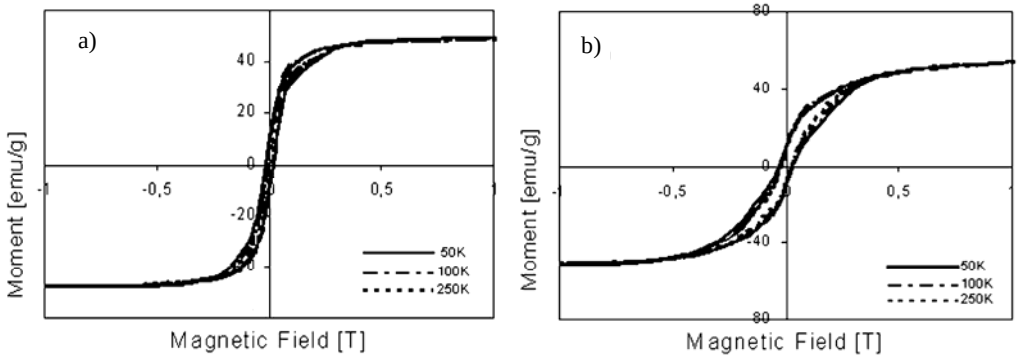

Fig. 4. Hysteresis loops of the nanocomposites after frontal polymerisation and thermolysis at: a) 873 K (specimen 3), b) 1083 K (specimen 4)

The hysteresis loops recorded at 50, 100, and 250 K are shown in Figure 4. The loops are closed and symmetrical with respect to the origin of the coordinate system. The shape of the loops evidences the ferromagnetic character of the material. No evidence of superparamagnetism was observed. The coercivity depends on the measurement temperature and very slightly decreases with increasing temperature. At room temperature, the material thermolysed at 873 K showed soft magnetic properties with a coercivity of 0.01 T. A somewhat higher coercivity was observed for the material thermolysed at 1023 K. This may be related to the formation of two crystallographic forms of cobalt, differing in their lattice constants and magnetic anisotropy field. The remanence could not be measured accurately, because the specimens were compacted with additional resin.

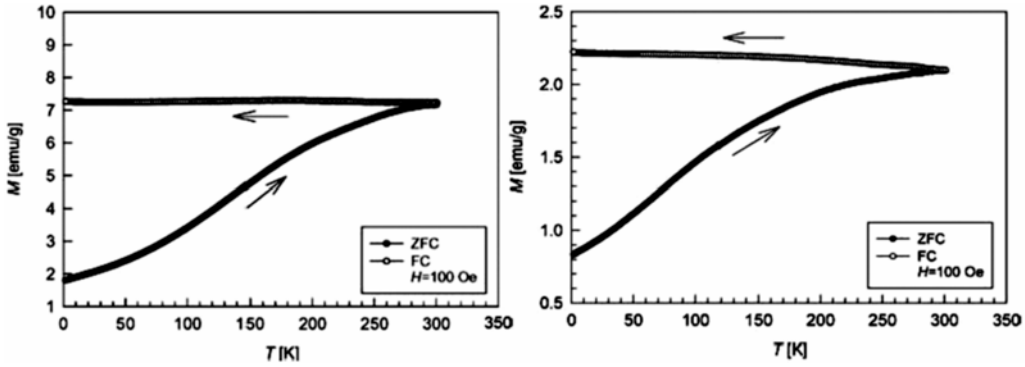

Fig. 5. ZFC and FC curves versus temperature for nanocomposites obtained by thermolysis of frontally polymerised material at different temperatures: a) 873 K (specimen 3), b) 1073 K (specimen 4)

In Figure 5, the zero-field-cooled (ZFC) and field-cooled (FC) magnetisation curves as a function of temperature, taken in the field of 5×10^{-3} T, are presented. Both dependences look similar and the magnetisations of the FC curves are almost independent of temperature. The magnetisation of the ZFC curves increases with increasing temperature, however no distinct maximum representing a blocking temperature is seen. The ZFC and FC magnetisation curves show irreversibility up to 300 K, but their shapes are characteristic of a system dominated by interparticle interactions rather than superparamagnetism.

4. Conclusions

Cobalt nanoparticles with a mean size in the range 12–15 nm can be prepared by the frontal polymerisation and thermolysis of acrylamid cobalt nitrate complex. The particle size strongly depends on the thermolysis temperature. The application of this procedure stabilizes the nanostructure, enables spherical nanoparticles to be processed within a narrow window of sizes, and protects the crystallites from oxidation. The

particles exhibit ferromagnetic properties. Their room temperature coercivity depends on the thermolysis temperature, and higher temperatures result in higher coercivity. The magnetic behaviour of the nanocomposites is dominated by interparticle dipolar interactions.

Acknowledgement

Financial support from the State Committee of Scientific Research (grant PBZ-KBN-095/T08/2003) is gratefully acknowledged.

References

[1] O'GRADY K., LAIDLER H., J. Magn. Magn. Mater., 200 (1999), 616.
[2] WOODS S.I., KIRTLEY J.R., SUN S., KOCH R.H., Phys. Rev. Lett., 87 (2001), 137205.
[3] PENG D.L., SUMIYAMA K., HIHARA T., YAMAMURO S., KONNO T.J., Phys. Rev. B., 61 (2000), 3103.
[4] JAMET M., WERNSDOEFER W., THIRION C., MAILLY D., DUPUIS V., MELION P., PEREZ A., Phys. Rev. Lett., 86 (2001), 4676.
[5] BONARD J.M., SERAPHIN S., WEGROWE J.E., JIAO J., CHATELAIN A., Chem. Phys. Lett., 343 (2001), 251.
[6] DONG X.L., ZHANG Z.D., JIN S.R., KIM B.K., J. Magn. Magn. Mater., 210 (2000), 143.
[7] SUN S., MURRAY C.B., DOYLE H., Mater. Res. Symp. Proc., 577 (1999), 385.
[8] BI H., LI S., JIANG X., DU Y., YANG C., Phys. Lett. A, 307 (2003), 69.
[9] TOMITA S., HIKITA M., FUJII M., HAYASHI S., AKAMATSU K., DEKI S., YASUDA H., J. Appl. Phys., 88 (2000), 5452.
[10] GUBIN S.P., Colloids Surf. A: Phys. Chem. Eng. Aspects, 202 (2002), 155.
[11] SAITO Y., MA J., NAKASHIMA J., MASUDA M., Z. Phys. D: At. Mol. Clusters, 40 (1997), 170.
[12] KITAHARA H., OKU T., HIRANO T., SUGANUMA K., Diamond Relat. Mater., 10 (2001), 1210.
[13] JAMET M., WERNSDORFER W., THIRION C., MAILLY D., DUPUIS V., MÉLINON P., PÉREZ A., Phys. Rev. Lett., 86 (2001), 4676.
[14] PARK I.-W., YOON M., KIM Y.M., KIM Y., YOON H., SONG H.J., VOLKOV V., AVILOV A., PARK Y.J., Solid State Comm., 44 (2003), 385.
[15] GUBIN S.P., SPICHKIN YU.I., KOKSHAROV YU.A., YURKOV G.YU., KOZINKIN A.V., NEDOSEIKINA T.I., KOROBOV M.S., TISHIN A.M., J. Magn. Magn. Mater., 265 (2003), 234.
[16] GUBIN S.P., KOKSHAROV YU.A., Inorg. Mater., 38 (2002) 11, 1085.
[17] POMOGAILO A.D., DZHARDIMALEVA G.I., Polymer Sci. Ser. A, 46 (2004), 250.
[18] SAVOSTYANOV V.S., PONOMAREV V.I., POMOGAILO A.D., SELENOVA B.S., IVLEVA I.N., STARIKOV A.G., ATOVMYAN L.O., Izv. Akad. Nauk SSSR, Ser. Khim., 4 (1990), 762.
[19] GONG. W., LI H., ZHAO Z., CHEN. J., J. Appl. Phys. 69 (1991), 5119.
[20] CHEN J.P., SORENSEN C.M., KLABUNDE. K.J., HADJIPANAYIS. G.C., Phys. Rev. B 51 (1995), 15.
[21] DONG X.L., ZHANG Z.D., JIN S.R., KIM B.K., J. Magn. Magn. Mater. 210 (2000) 143.

Received 4 May 2005
Revised 24 August 2005

Materials Science-Poland, Vol. 24, No. 2/1, 2006

Carburisation of Fe–Ni–Cr alloys at high temperatures

A. UL-HAMID[1*], H. M. TAWANCY[1], S. S. AL-JAROUDI[2],
A. I. MOHAMMED[1], N. M. ABBAS[1]

[1]Center for Engineering Research, Research Institute,
King Fahd University of Petroleum and Minerals, P. O. Box 1073, Saudi Arabia

[2]Saudi Aramco, Tanajib, P.O. Box 65, Saudi Arabia

A large number of radiant tubes belonging to an ethylene furnace of a petrochemical plant failed during service. All tubes exhibited severe carburisation, while some of them lost their structural integrity and sagged. The tube material was based on a Fe–Ni–Cr alloy system with three varying compositions. Scanning electron microscopy and energy dispersive X-ray spectroscopy were used to characterize the microstructure and elemental composition of the tube material. Microhardness was tested to determine their mechanical strength. Experimental results indicated that the sagged tubes exhibited a higher degree of carburisation as compared to other tubes. The microstructure of these tubes also revealed coarser Cr-carbide precipitation and a continuous carbide lattice at austenite grain boundaries. It was concluded that exposure to excessive temperature during service was responsible for the degradation of all tube materials. Based on the above results, it is recommended that better control of furnace temperature should be employed in order to avoid overheating during service.

Key words: *Fe–Ni–Cr alloy; carburisation; SEM; furnace tube; high temperature*

1. Introduction

Ethylene (C_2H_4) is generated by cracking ethane (C_2H_6) in pyrolysis furnaces. The simplest illustration of the decomposition of ethane molecules into ethylene is represented by the following formula:

$$C_2H_6 \rightarrow C_2H_4 + H_2$$

The process stream in a furnace consists of a mixture of steam and ethane, passed through a coil of reaction tubes externally heated to the temperatures of 950–1150 °C. The temperature of the gas is raised quickly, and it is passed through

*Corresponding author, e-mail: anwar@kfupm.edu.sa

the coil at a high velocity with a short residence time. The temperature in the reaction tube is approximately 850 °C. It is well known that the process of producing ethylene generates free carbon according to the following reaction [1]:

$$C_2H_4 \rightarrow CH_4 + C$$

Carbon is deposited at the internal surface of the tube wall as adherent coke. The coke is removed by shutting off the hydrocarbon feed and passing air and steam through the coil. Such a process is known as decoking. Frequent decoking accelerates the thermal damage of the tubes, while less frequent decoking increases the rate of carburisation. The nominal and measured compositions of tubes made of three different alloys are shown in Table 1. Nine tubes, each with a wall thickness of approximately 8 mm, were examined in this study. The objective of this investigation was to compare the performance of furnace tubes, identify the cause(s) of their failure, and determine their suitability for service at high temperatures.

Table 1. Nominal and measured chemical compositions (wt. %) of tube materials

Element	Chemical composition (wt. %)					
	Nominal			Measured		
	Tubes					
	1, 2	3–6	7–9	1, 2	3–6	7–9
	HK-40(A351)	HP 25Cr-35 Ni, MA	35Cr-45 Ni, MA			
Ni	19–22	35	45	21.0	37.7	52.8
Cr	23–27	25	35	22.2	16.3	31.5
Si	1.75[a]	2.5	2.5	1.8	4.5	1.7
Fe	46.7–57.7	Bal.	Bal.	55.1	41.6	14.0
C	0.35–0.45	0.45	0.45	ND	ND	ND
Mn	1.5[a]	–	–	ND	ND	ND
Nb	–	1.5	1.5	ND	ND	ND
Other[b]	–	Ti, Zr	Ti, Zr	ND	ND	ND

[a]Maximum value.
[b]Small amounts.
ND – not detected in the tube alloy matrix.

2. Experimental procedure

The tubes were sectioned and mounted in cross-sections for metallurgical evaluation in both polished and etched conditions. The samples were etched with a freshly prepared mixture of 20 wt. % nitric acid (HNO_3) and 4 wt. % hydrofluoric acid (HF). The etchant was obtained by mixing 200 cm^3 of concentrated 70 wt. % HNO_3 with 70 cm^3 of concentrated 49 wt. % HF and 670 cm^3 of distilled water [2]. Each of the specimens was immersed in the etchant for two hours at room temperature and then rinsed with distilled water before drying. Microstructural features of the scale, the carburised zone, and the underlying alloy were characterized using a scanning elec-

tron microscope (SEM), and their chemical compositions were determined using energy dispersive X-ray spectroscopy (EDS). Vickers microhardness tests were used to compare the mechanical strength of the samples. The internal surfaces of the tubes were tested for carburisation using a NACE standard [2].

3. Experimental results

3.1. Visual inspection

Visual inspection revealed that sagging in four tubes (Nos. 3–6) resulted in a considerable loss of shape. Sagging was not observed in other tube samples. The scale formed on the surface of the tubes was adherent and there was no evidence of flaking. Effects of general or localized wall thinning were not observed in any of the tube samples. Moreover, no crackings in the tube walls were evident.

The stresses resulting from gas pressure in the ethylene production process are relatively low and it is well known that the most common failure modes of furnace components are longitudinal creep-rupture and carburisation [1].

3.2. Material verification

Elemental analysis of each tube sample was performed using energy dispersive X-ray spectroscopy. Representative EDS spectra and measured compositions for each tube material, along with its nominal composition, are shown in Figs. 1a–c and Table 1. The difference in composition between the nominal and measured values is expected due to the exposure of tube material to elevated temperatures in service. This exposure results in the precipitation of M-carbides (where M is Cr, Nb) within the matrix and at the grain boundaries, thus altering the starting composition of the matrix. Within this limitation, the measured composition can be seen to be in agreement with the nominal composition, confirming the tube materials are HK-40 (for tubes 1-2), HP 25Cr-35Ni Micro Alloy (for tubes 3-6), and 35Cr-45Ni Micro Alloy (for tubes 7-9). Based on the nominal composition, these alloys are suitable for the kind of service conditions encountered in an ethylene furnace. Alloy HK-40 is Ni-Cr grade, suitable for low stress reformer catalyst tube designs with service temperatures up to 1025 °C. Increased levels of silicon provide improved carburisation resistance, to benefit low severity ethylene cracking furnace coils. Alloy HP 25Cr-35Ni MA is a micro-alloyed HP with small additions of Ti and rare earth elements, which is especially stable at high temperatures. This alloy forms tenacious oxide films that reduce surface oxidation at temperatures of 1150 °C. The third alloy, 35Cr-45Ni MA, can be used up to 1150 °C and possess good high temperature strength and carburisation resistance. This micro-alloy offers improved aged ductility and resistance to metal dusting. It is quite suitable for components operating in the hot zones of pyrolysis coils and components of reformer outlet manifolds.

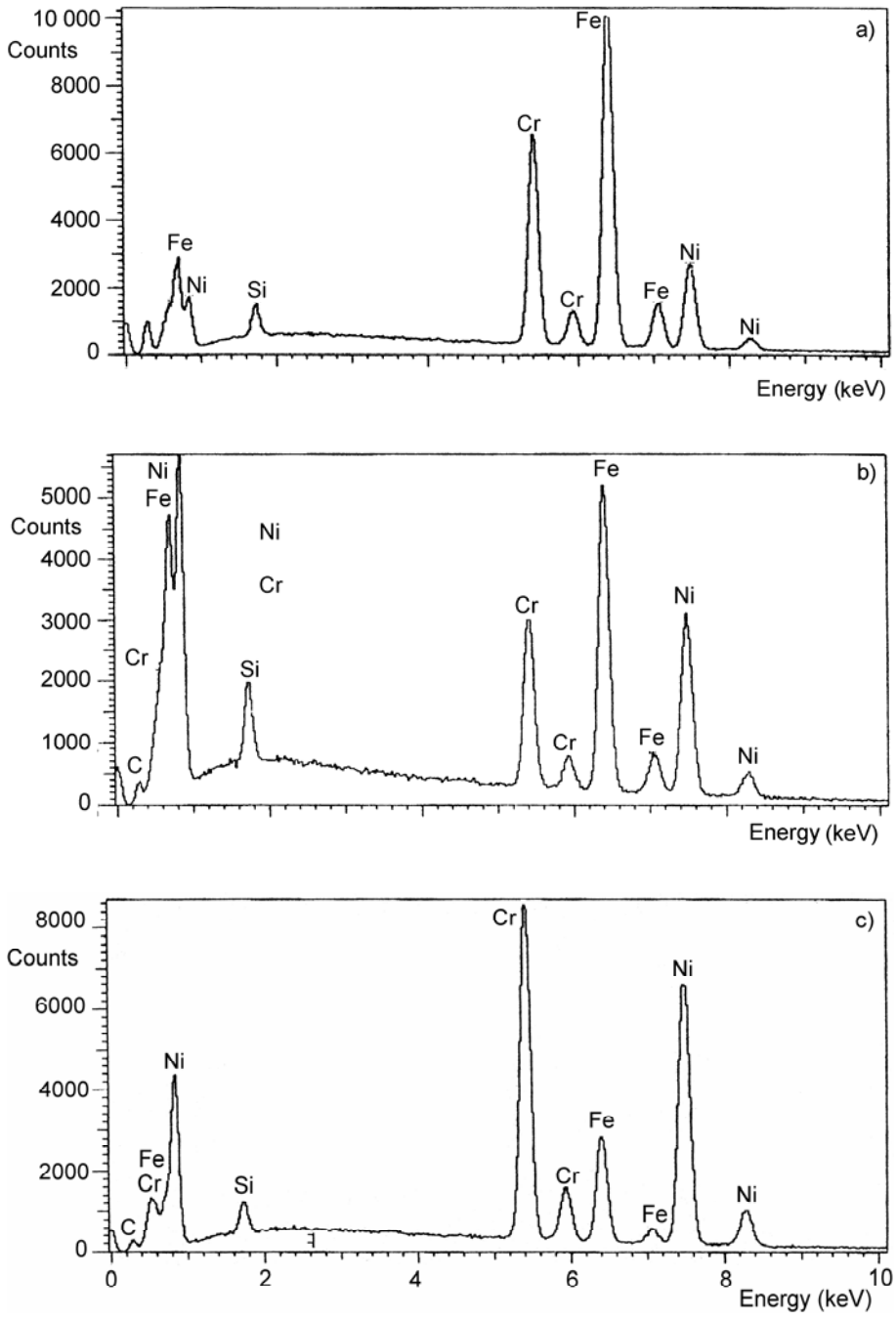

Fig. 1. Energy dispersive X-ray spectra derived from an uncarburised austenite region for verifying the furnace tube material: a) sample No. 2, b) sample No. 5, c) sample No. 8

3.3. Microstructure of furnace tube materials Nos. 1 and 2

A typical optical macrograph of a tube cross-section obtained from sample No. 1 is shown in Figure 2. The carburised zone was about 8 mm in depth. The average carburised depth in samples No. 1 and 2 was observed to be 22% of the tube wall thickness.

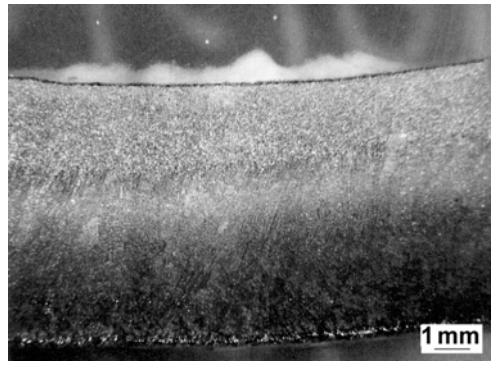

Fig. 2. Optical macrograph of a tube cross-section obtained from sample No. 1 showing the carburised region

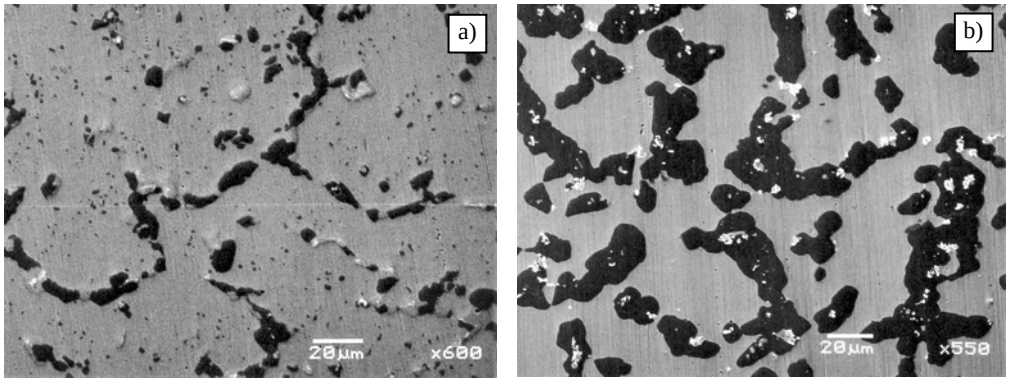

Fig. 3. Secondary electron SEM image obtained from (a) uncarburised and (b) carburised regions of sample No. 1

The microstructure of the uncarburised region is shown in a secondary electron SEM image in Figure 3a. The tube material consisted of relatively large equiaxed grains with precipitation at the grain boundaries. Energy dispersive X-ray spectroscopy revealed that the matrix was comprised of austenite (Fe–Cr–Ni solid solution) and that the grain boundary constituted a Cr-rich carbide. The austenite matrix also revealed the presence of coarse and fine particles of Cr-rich carbides. The microstructure of the carburised region for the same sample is shown in Figure 3b. It can be observed that the Cr-rich carbide precipitates present within the austenite grains are coarser in size compared to those in the uncarburised region.

3.4. Microstructure of furnace tube materials Nos. 3–6

Figure 4 shows the optical macrograph of a tube cross-section from this group of tubes (Nos. 3–6). It can be seen that more than 50% of the wall thickness exhibited signs of carburisation.

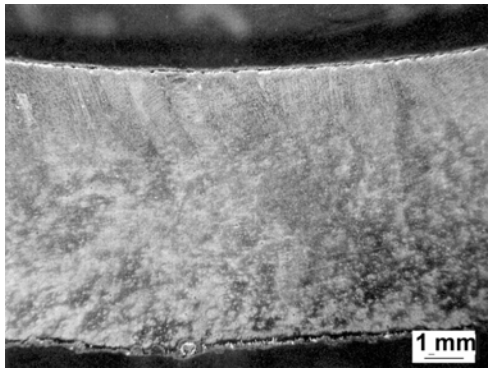

Fig. 4. Optical macrograph of a tube cross-section from sample No. 5 showing the carburised region

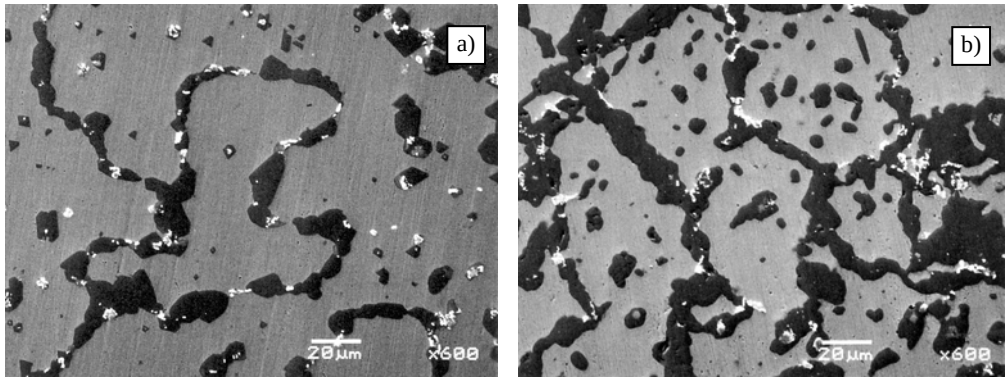

Fig. 5. Secondary electron SEM image obtained from uncarburised (a) and carburised (b) regions of tube sample No. 5

A typical microstructure obtained from an uncarburised region of tube sample No. 5 is shown in the secondary electron SEM image in Figure 5a. Compared to the uncarburised region of tube material No. 1 (see Figure 3a), the carbide precipitation appears relatively coarse both at the austenite grain boundaries and within the matrix itself. This is confirmed by the EDS analysis in which the Cr concentration was determined to be as low as 13 wt. % at various regions within the austenite. The depletion of Cr within the matrix indicates the tendency of Cr to diffuse and form Cr-rich carbides at the austenite grain boundaries and/or coarsen pre-existing carbides within the austenite. The diffusion of Cr is enhanced at elevated temperatures. The higher the temperature, the greater the carburised zone and the coarser the carbide precipitates.

The carburised region from the same sample shows a high degree of carbide precipitation at the grain boundaries and blocky carbide particles in the matrix as shown

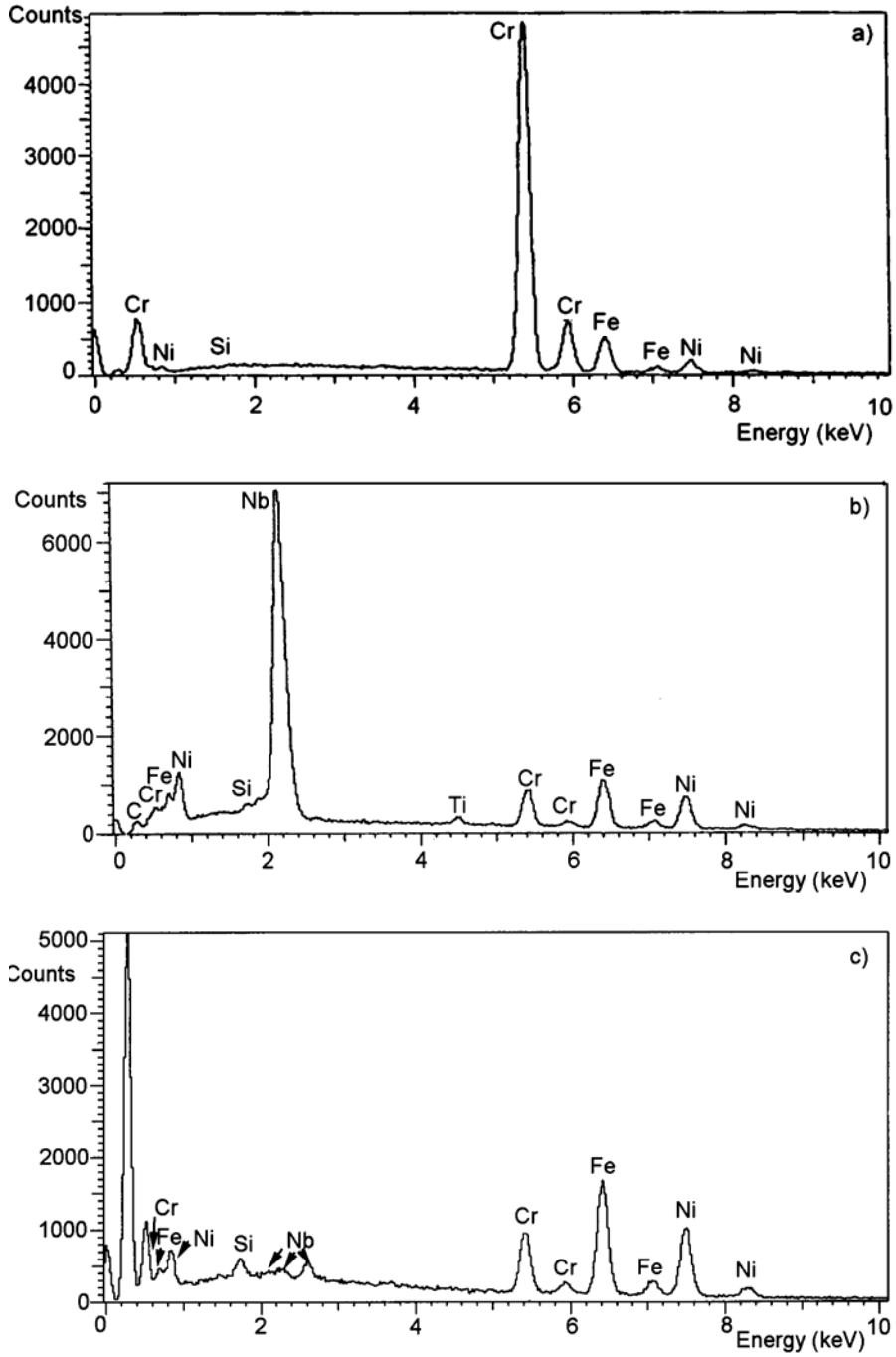

Fig. 6. Energy dispersive X-ray spectra obtained from grain boundary precipitates exhibiting Cr enrichment (a), white precipitates exhibiting Nb enrichment (b), and a carburised region near the tube inner surface (c)

by the SEM image in Figure 5b. The grain boundary precipitate predominantly comprises Cr, as shown by the EDS spectrum in Figure 6a, and is present in the form of a continuous lattice. The white precipitates adjacent to the grain boundaries are Nb-rich, as shown by the EDS spectrum in Figure 6b.

Relatively small additions of Nb to the resistant castings can increase their resistance to thermal shock. Furthermore, Nb acts as a carbide stabilizer by forming MC-type carbides, which prevent massive carbide precipitation at the grain boundaries. The presence of Nb was not detected during material verification by SEM/EDS, probably due to its low concentration within the exposed tube alloy matrix.

Table 2. Chemical composition (wt. %) of a carburised region of HP25-35 alloy

Element	Content (wt. %)
C	61.10
Si	0.83
Fe	16.74
Ni	14.34
Cr	6.79
Nb	0.22

EDS analysis of the carburised region near the inner tube surface (Fig. 6c) showed high C content; the quantified results are summarized in Table 2. Massive carbide precipitation at the austenite grain boundaries (forming a continuous lattice) and the presence of carbides as coarse blocky particles within the matrix indicate the exposure of the furnace tubes to an excessively high temperature that leads to heavy carburisation.

3.5. Microstructure of furnace tube materials Nos. 7–9

Optical and SEM micrographs of the cross-section of tube No. 9 are shown in Figures 7a, b, respectively. The carburised region was approximately 26% of the wall

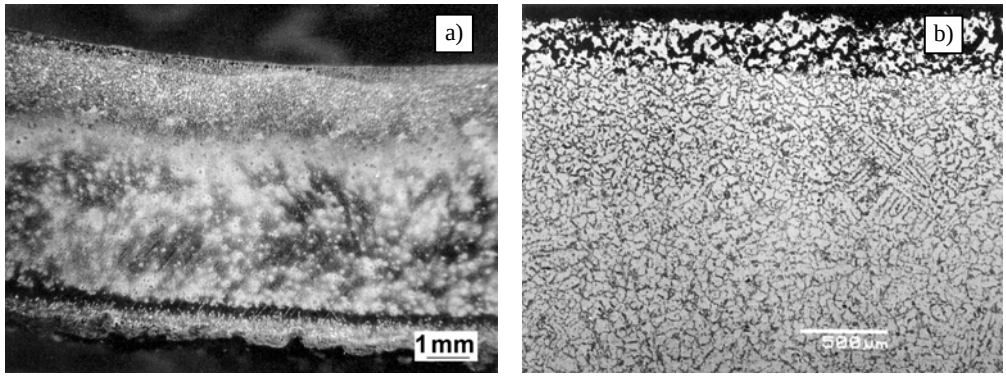

Fig. 7. Optical (a) and SEM (b) micrographs of the cross-section of tube No. 9 showing a carburised region

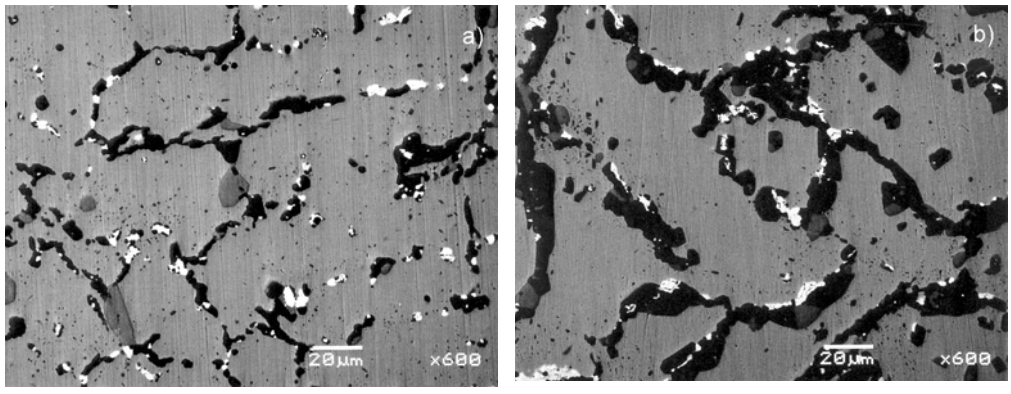

Fig. 8. Secondary electron SEM image obtained from uncarburised (a) and carburised (b) regions of tube sample No. 8

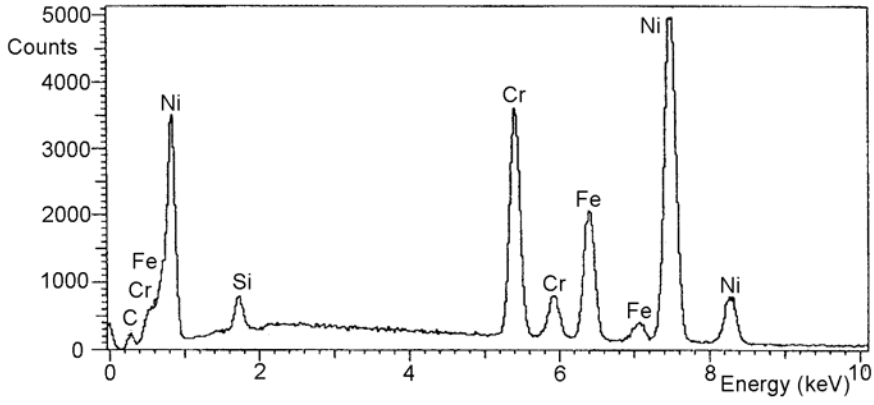

Fig. 9. Energy dispersive X-ray spectrum obtained from light grey precipitates, showing a large peak for Ni

thickness in these samples. Typical microstructures obtained from the uncarburised and carburised regions of the furnace tube material (Nos. 7–9) are shown in Figures. 8a, b, respectively. The microstructures comprised dark Cr-rich and white Nb-rich precipitates, along with greyish precipitates comparatively richer in Ni as shown by the EDS spectrum in Figure 9 and chemical composition in Table 3.

Table 3. Chemical composition of light grey precipitates from sample No. 8

Element	Content (wt. %)
Ni	63.1
Cr	19.8
Si	1.7
Fe	15.4

3.6. Analysis of the scale formed on the furnace tube material (Nos. 1–9)

A typical morphology of the scale formed at the internal surface of the furnace tubes is shown in the backscattered electron SEM image in Figures 10, 11. The scale was discontinuous and broken, thus providing minimal protection to the underlying alloy from diffusing species. The X-ray map and various EDS spectra obtained from the region (Fig. 11) revealed that the oxide formed at the surface was Cr-rich, while Fe and Ni could also be detected in the scale. In addition, Si and to some extent Cr-rich oxides were detected at the austenite grain boundaries just below the alloy surface. The Cr content of the austenite grains in this region was as low as 4.2 wt. %, which is inadequate to sustain a continuous protective Cr_2O_3 scale.

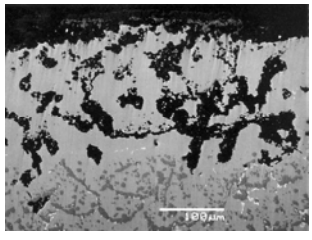

Fig. 10. Backscattered electron SEM image showing a typical morphology of scale formed at the internal surface of the tube material

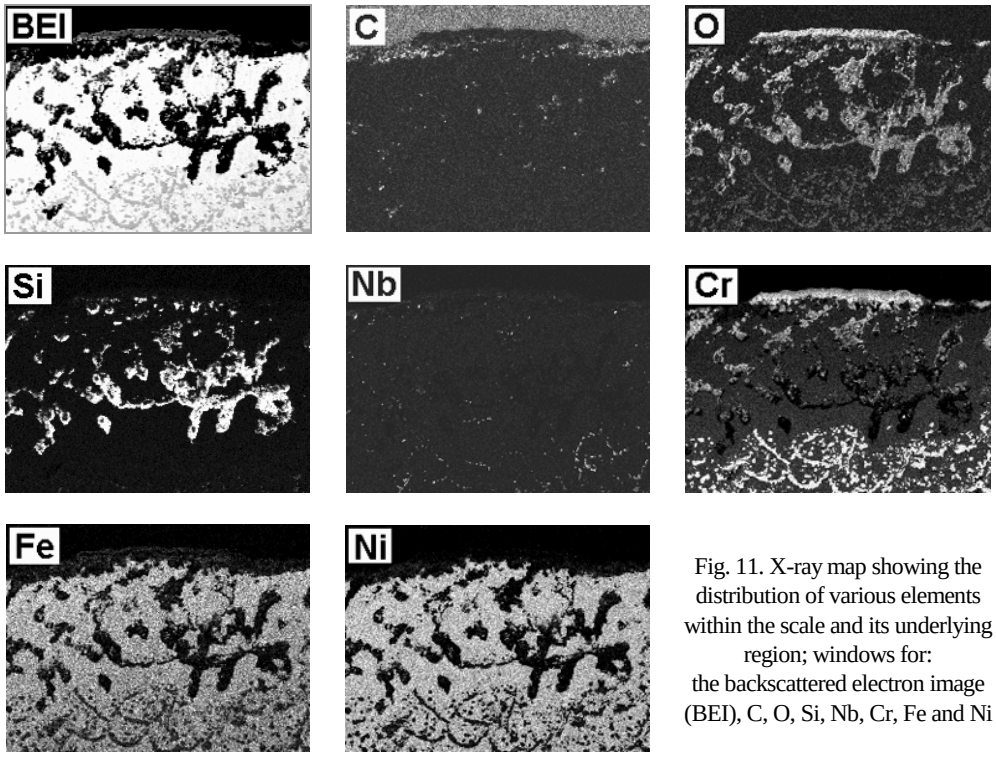

Fig. 11. X-ray map showing the distribution of various elements within the scale and its underlying region; windows for: the backscattered electron image (BEI), C, O, Si, Nb, Cr, Fe and Ni

Based on the above observations, it can be concluded that the alloys were incapable of developing a protective oxide scale. This could partly be due to the relatively low oxygen potential of environments typically encountered in ethylene production. The presence of a protective oxide scale can impede C diffusion into the alloy and play an important role in reducing the extent of carburisation. Earlier studies of carburisation have shown that in severely carburising environments, where the carbon activity reaches 1, Cr_2O_3-forming alloys develop surface carbide scales rather than oxide scales [3]. It is evident from the above results that the oxygen potential of the environment promoted the formation of an oxide scale. The scale was not protective, however, as indicated by the presence of voids, which permitted the penetration of carbon into the alloy substrate.

3.7. Microhardness measurements

At the inner surface of the tube, where carburisation was most severe, the average hardness was found to be HV 316 corresponding to HRC 32. Towards the outer surface, however, the average hardness was reduced to HV 216 corresponding to HB 206. In as-cast conditions, the room temperature hardness of these alloys is typically HB 171. Two factors can contribute to the observed hardening, namely a) carburisation and b) thermal aging. Hardening due to carburisation is expected to predominate near the inner surface of the tube. In contrast, the effect of thermal aging should progressively increase with depth from the inner surface. Increased hardness at the carburised zone can be attributed to the high degree of carbide precipitation and also to C pickup due to the carburising environment. Hardness measurements, combined with microstructural observations, suggest that carburisation led to the formation of a surface hardened layer of reduced ductility. The formation of this layer further confirms the inability of the alloy to form a continuous protective oxide scale at its surface.

4. Discussion

Carburisation occurs when C from the environment combines at elevated temperatures primarily with Cr and other carbide formers (Nb, W, Mo, Ti, etc.) present in the alloy. The carbides may be quite complex and form within the grains and along grain boundaries. They are hard and brittle. The overall effect is a drastic reduction of ductility at elevated temperatures, a reduction of oxidation resistance, and an adverse affect on creep strength. Carburisation is common in ethylene cracking furnaces due to the presence of high tube metal temperatures – up to 1150 °C (which is the practical upper limit for most heat resistant alloys) – and high carbon potentials associated with the hydrocarbon feedstock. The carburisation of furnace tubes is unpredictable and non-uniform in nature.

The typical microstructure of heat-resisting austenitic casting steels consists of an austenite matrix and carbide precipitates. The use of varying contents of Cr and Ni in these alloys allows properties such as, resistance to carburisation, and hot gas corrosion to be controlled strength at elevated temperatures. Nickel imparts the alloy with an increased resistance to carburisation, thermal shock, and thermal fatigue, while chromium provides increased corrosion and oxidation resistance [4]. Fine dispersion of carbides in the austenitic matrix increases high temperature strength to a considerable extent. Rapid cooling from a temperature near the melting point results in the supersaturation of C. Subsequent reheating (e.g. during service) results in carbide precipitation. The lower the reheating temperature, the finer the precipitated carbides. Finer dispersion of carbides increases the creep strength of the alloy. Exposure to high temperatures, however, results in the coarsening, agglomeration, and spheroidising of carbides, thus reducing their effectiveness as a source of strength. In addition, slow cooling from a high temperature results in carbide precipitation at austenite grain boundaries. A continuous lattice of carbides at the grain boundaries is undesirable, since they embrittle the alloy. The size of carbides can thus be useful in indicating whether the alloy has been exposed to excessive temperatures during service.

All the furnace tubes examined in this study exhibited carburisation. The average depth of the carburised zones in furnace tubes Nos. 3–6 was 58% of the total wall thickness, as compared to 22% for tubes Nos. 1–2 and 26% for tubes Nos. 7–9. Moreover, visual examination also revealed that tubes Nos. 3–6 were clearly sagged, indicating significant plastic deformation during service. Clearly, tubes Nos. 3–6 exhibited the most severe degradation amongst the studied samples. This was also confirmed by SEM/EDS examination, in which the microstructures of tubes Nos. 3–6 exhibited relatively coarse blocky carbides within the austenite matrix and a continuous carbide lattice at the grain boundaries. Massive precipitation of carbide phases is typical of carburisation [5, 6]. These observations suggest that the alloy had been exposed to an excessively high temperature during service. The hardness of the carburised zone was also found to be higher in tubes Nos. 3–6 as compared to the other tube materials, indicating a higher precipitation and C pickup by the alloy. The deposition of coke on the inner pipe wall also promotes C diffusion and the precipitation of secondary carbides within the alloy. As demonstrated earlier under the operating conditions, the tube alloy develops a non-protective surface oxide scale. Carbon deposited on the surface can readily penetrate the oxide scale into the alloy substrate, where it reacts with carbide-forming elements, particularly Cr, to form the observed Cr-rich carbides.

5. Conclusions

Experimental data shows that all the tube materials had undergone carburisation due to exposure to excessively high temperatures during service. Carburisation was

most severe in tubes Nos. 3–6, indicating that these could have been overheated for relatively longer periods during service compared to others.

The temperature of the furnace should be controlled closely, in order to avoid over-heating during ethylene production and decoking.

Acknowledgements

The authors wish to acknowledge the support of the Research Institute of King Fahd University of Petroleum and Minerals, Dhahran, Saudi Arabia.

References

[1] BLACKBURN J., [in:] *Carburization in High Temperature Process Plant Materials*, Colloquium Proceedings Coordinated by J. Norton, Commission of the European Communities, Luxembourg, Report No. EUR 7773, 1981, 7.
[2] NACE Standard TM 0498-98-Item No. 21235.
[3] LAI G. Y., [in:] *High Temperature Corrosion in Energy Systems*, M. F. Rothman (Ed.), TMS-AIME, Warrendale, Pennsylvania, 1985, 551.
[4] *ASM Metals Handbook, Properties and selection of metals*, Vol. 1, 8th Edition, 1977.
[5] TAWANCY H.M., ABBAS N.M., J. Mater. Sci., 26 (1992), 1061.
[6] SCHNAAS A., GRABKE H.J., Oxidation of Metals, 12 (1978), 387.

Received 16 May 2005
Revised 24 July 2005

Materials Science-Poland, Vol. 24, No. 2/1, 2006

Sliding wear, slurry erosive wear, and corrosive wear of aluminium/SiC composite

M. RAMACHANDRA[1*], K. RADHAKRISHNA[2]

[1]Department of Manufacturing Engineering, BMS College of Engineering, Bangalore 560 019, Karnataka, India.

[2]Department of Mechanical Engineering, BMS College of Engineering, Bangalore 560 019, India

In this study, an aluminium based metal matrix was reinforced with silicon carbide (SiC) particulates using the conventional vortex casting technique. Macro- and microstructural studies conducted on the samples revealed a near uniform distribution of SiC particulates. Sliding wear, slurry erosive wear, and corrosive wear of the as-cast metal matrix composite (MMC) were studied. It was found that sliding wear and slurry erosive wear resistance improved considerably with the addition of SiC particles, whereas corrosion resistance decreased. Microscopic examinations of the worn surfaces, wear debris, and subsurface show that the base alloy wears primarily due to micro-cutting. MMCs wear, however, because of micro-cutting, oxidation, plastic deformation, and thermal softening. In slurry erosive wear, the formation of a passive layer retarded the wear of the material. It was observed that pitting corrosion was the dominant mechanism. The bulk hardness increased with an increase in the percentage of SiC particulates. There was not much change in the density of MMCs compared to the base metal.

Key words: *metal matrix composite; MMC; Al-based MMC; SiC; mechanical properties; wear; corrosion*

1. Introduction

The emergence of modern processing techniques, coupled with the need for lighter materials with high strength and stiffness, has catalysed considerable scientific and technological interest in the development of high-performance composite materials as serious competitors to traditionally engineered alloys. The majority of such materials are metallic matrixes reinforced with a high strength, high modulus, and often brittle second phase, in the form of a fibre, particulate, or whiskers embedded in a ductile metal matrix. The reinforced metal matrix offers the potential for a sufficient improvement in efficiency, reliability, and mechanical performance over traditional

*Corresponding author, e-mail: m_rchandra@yahoo.co.in

monolithic alloys. Discontinuously reinforced aluminium matrix composites have emerged from the need for lightweight, highly rigid materials, which are desirable in applications such as high-speed reciprocation. Reinforcement usually comprises particles or whiskers of a ceramic such as silicon carbide, alumina, graphite, etc. A significant increase in stiffness and strength can be conferred with even small reinforcement volume fractions. Many of the applications, for which MMCs are desirable, also require enhanced tribological performance.

The wear resistance of composites has received much attention in the literature, but a direct comparison between findings is often difficult due to specific differences in the wear testing procedure. Work concerning the non-lubricated sliding wear behaviour of such materials has examined a number of variables [1], such as the contact pressure [2–4], sliding velocity [5, 6], temperature [7, 8], particle volume fraction [9, 10], and particle size [11]. A number of mechanisms have been proposed to explain the sliding wear behaviour of these composites, many of which are discussed in a review of the subject [12].

In recent years, considerable interest has been paid in extending the use of these composite materials in the marine environment [13]. This demands an examination of the corrosion as well as erosion–corrosion characteristics of the composite materials under a simulated marine environment. A few studies have been reported by different authors on the erosive–corrosive wear behaviour of Al alloys and composites [14]. It has been reported by a group of authors that the composites exhibit inferior wear resistance to that of alloys under corrosive media [15, 16]. Other groups have reported that composites have higher corrosion and erosive–corrosive wear resistance [17].

In the present investigation, aluminium-based metal matrix composites containing up to 15% weight percentage of SiC particulates, were successfully synthesized using the vortex method. Dry sliding wear, slurry erosive wear, and corrosive wear behaviour of the MMCs was investigated along with some of its mechanical properties.

2. Materials

The matrix material used in the experimental investigation was an aluminium alloy (Si – 7.2%), LM25, whose chemical composition is listed in Table 1. This alloy conforms to BS1490, and its SEM micrograph is shown in Fig. 1. LM25 is mainly used when good mechanical properties are required. It is, in practice, a general-purpose high strength-casting alloy. In its heat-treated form, its tensile strength can be increased from around 130–150 $N \cdot mm^{-2}$ to up to 230–280 $N \cdot mm^{-2}$. Aluminium and silicon alloys have no solid solubility below the eutectic, and the microstructure solidifies in the form of silicon particles in an aluminium matrix. Aluminium–silicon castings have good corrosion resistance and are used in the cases where particularly high strength is required.

Silicon carbide (SiC) used as reinforcement is a highly wear resistant and has good mechanical properties, including high-temperature strength and thermal shock resistance. The SEM micrograph of SiC used in the investigation is shown in Fig. 2. The average particle size was 10 μm, and particles were found to be irregularly shaped.

Table 1. Chemical composition of the aluminium base alloy (wt. %)

Si	Fe	Cu	Mn	Mg	Zn	Al
7.2	0.2	0.23	0.1	0.4	0.1	balance

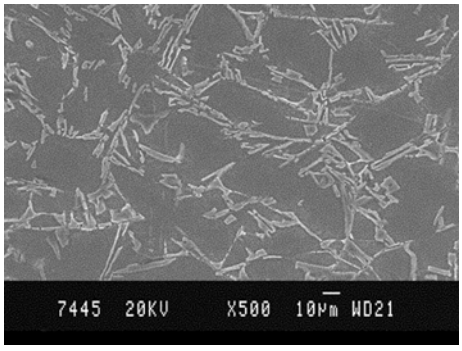

Fig. 1. Matrix material, A – Si 7.2%

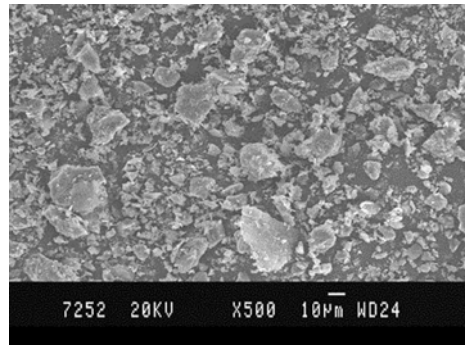

Fig. 2. Micrograph of silicon carbide particles

3. Experimental procedure

Processing. The synthesis of the metal matrix composite used in the present study was carried out by the stir casting method. Al–Si (7.2%) alloys in the form of ingots were used for the trials. The cleaned metal ingots were melted to the desired super heating temperature of 800 °C in graphite crucibles under a cover of flux in order to minimize the oxidation of the molten metal. A three-phase electrical resistance furnace with temperature controlling device was used for melting. For each melting, 3–4 kg of alloy was used. The super heated molten metal was degassed at a temperature of 780 °C. SiC particulates, preheated to around 500 °C, were then added to the molten metal and stirred continuously by a mechanical stirrer at 720 °C. The stirring time was between 5 and 8 minutes, and the impeller speed was 550 rpm. During stirring, magnesium was added in small quantities to increase the wettability of SiC particles. The dispersion of the preheated SiC particulates was achieved in accordance with the vortex method [18]. The melt, with the reinforced particulates, was poured into the dried, coated, cylindrical permanent metallic moulds 80 mm in diameter and 175 mm high. The pouring temperature was maintained at 680 °C. The same molten metal–SiC particle mixture was poured into strip and spiral fluidity dies for fluidity measurements. The melt was allowed to solidify in the moulds. For the purpose of comparison, the base alloy was cast under similar processing conditions.

Heat treatment. The metal matrix composites produced were exposed to solutionising and age hardening heat treatment, as shown in Figure 3. The solutionising treatment was applied for 16 hours at 525 ºC, and age hardening was done for 18 hours at 175 ºC.

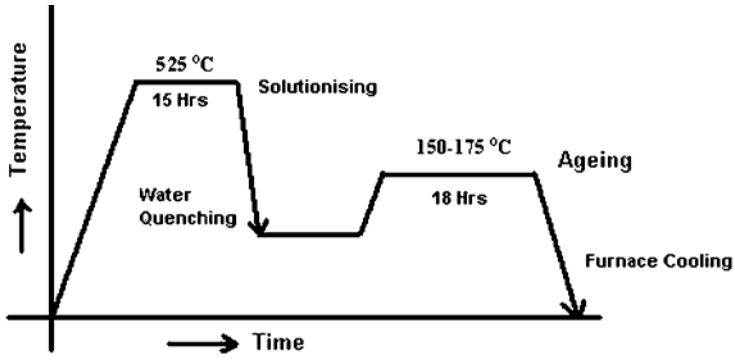

Fig. 3. Solutionising and ageing heat treatment cycle adapted to heat treat MMCs

Density. Density measurements were carried out on the base metal and reinforced samples using Archimedes principle [19]. The buoyant force on a submerged object is equal to the weight of the fluid displaced. This principle is useful for determining the volume and therefore the density of an irregularly shaped object, by measuring its mass in air and its effective mass when submerged in water (density = 1 g·cm^{-3}). This effective mass under water will be its actual mass minus the mass of the fluid displaced. The difference between the real and effective masses therefore gives the mass of the displaced water and allows the volume of the irregularly shaped object to be calculated. Mass divided by the volume thus determined gives a measure of the average density of the object.

Macro- and microstructural characterization. Macrostructural studies were conducted on the as-processed and machined composite castings in order to investigate the distribution of SiC particles retained in the metal matrix. Castings were plain turned on lathe to remove 5 mm of material and reveal the particle distribution on a macroscopic scale.

Microstructural characterization studies were conducted on unreinforced as well as on reinforced samples. This was accomplished by using a scanning electron microscope. The composite samples were metallographically polished prior to examination. Characterization was done in etched conditions. Etching was accomplished using Keller's reagent.

Bulk hardness and microhardness. Bulk hardness measurements were carried out on the base metal and composite samples by using the standard the Brinnel hardness test. The Brinell hardness measurements were carried out in order to investigate the influence of SiC particulate weight fractions on the matrix hardness. The applied load was 500 kgs, and the indenter was a steel ball 10 mm in diameter.

Microhardness measurements were carried out in order to investigate the influence of SiC particles on matrix hardness. The load applied was 50 g, and a Vickers indenter was used. Microhardness measurements were made on the particle and in its vicinity. Round specimens 20 mm in diameter were prepared and polished on differ-

ent grits of emery paper. Averages of 5 readings were taken for both bulk hardness and microhardness measurement.

Sliding wear. Two-body sliding wear tests were carried out on the prepared composite specimens. A computerized pin-on-disc wear test machine was used for these tests. The tangential friction force and wear in microns were monitored with the help of electronic sensors. These two parameters were measured as a function of load, sliding velocity, and per cent of SiC. For each type of material, tests were conducted at three different normal loads (4.9 N, 9.8 N, and 14.7 N), keeping the sliding speed fixed at 95 $m \cdot min^{-1}$. A cylindrical pin 5 mm in diameter and 40 mm long, prepared from composite casting, was loaded through a vertical specimen holder against a horizontal rotating disc. Before testing, the flat surface of a specimen was abraded using 2000 grit paper. The rotating disc was made of carbon steel, with a diameter of 50 mm and hardness of 64 HRC. Wear tests were carried out at room temperature without lubrication for about 140 minutes.

Corrosion wear. The oldest and most wildly used salt spray corrosion testing method was used in the investigation of the corrosive wear of MMCs. A fog of NaCl solution was introduced into a closed chamber, in which specimens were exposed at specific locations. The concentration of the NaCl solution was 3.5%. Corrosive fog was created by bubbling compressed air through hot deionised water. The salt solution was maintained at a temperature of 50 ºC. The specimens for fog corrosion were prepared by cutting specimens $10 \times 20 \times 5$ mm^3 in size from the composite castings. The surfaces of specimens were abraded using 600 grit size emery papers and degreased. Before testing, the specimens were weighed with an accuracy of 0.001 g and exposed to a corrosive atmosphere for a period of 240 h. The specimens were suspended in the corrosive chamber at regular intervals, exposing the abraded surface to salt solution fog. After corrosion testing, the specimens were immersed in Clark's solution for 5 minutes and gently cleaned with a soft brush to remove adhered particles. After drying thoroughly, the specimens were re-weighed to determine weight loss.

Slurry erosive wear. The experimental arrangement for slurry erosive wear consists of a stirrer, which can hold 4 specimens at a time, and a water-cooled pot. All 4 specimens were dipped in a slurry of distilled water and silica sand, and stirred at the speed of 376 $m \cdot min^{-1}$. The slurry was prepared by mixing 80-micron silica sand with distilled water in the ratio 1:2 (pH = 7.1). The slurry wear test was performed at ambient temperature, and the testing time was 14 h.

The specimens for the slurry erosive wear test were cut from composite ingots and plain turned to a diameter of 7 mm. Before testing, specimens were weighed with the accuracy of 0.001 g. After testing, specimens were dried and re-weighed to determine the percentage weight loss.

4. Results and discussion

4.1. Macrostructural and microstructural characterization

Macrostructural studies revealed a reasonably uniform distribution of SiC particles and a slight macro-segregation of particles in some places. The distribution of SiC particles is influenced by the tendency of particles to float due to density differences and interactions with the solidifying metal. It is therefore a strong function of the solidification rate and geometry of castings [20]. The photo macrograph in Figure 4 shows the distribution of SiC particles in a permanent mould cast ingot. A lower concentration of SiC particles was obtained at the top and a higher concentration at the bottom of the castings. The central 70–80% portion of the castings had a near uniform distribution of SiC particles.

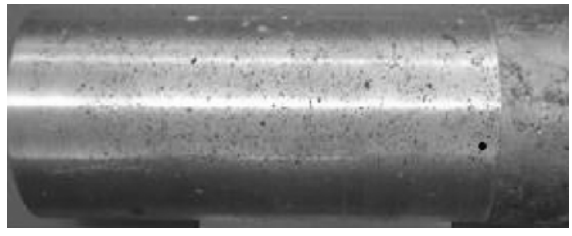

Fig. 4. Photo macrograph of MMC with 15% SiC particles

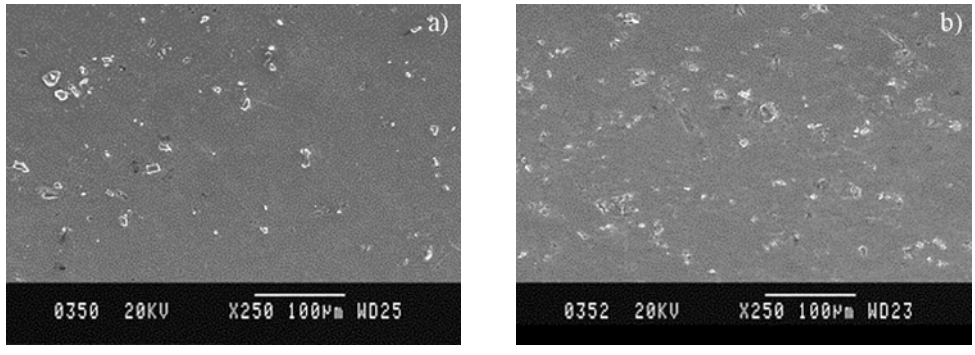

Fig. 5. SEM micrographs of: a) MMC with 5% SiC, b) MMC with 15% SiC particles

Figures 5a and b show the microstructure of MMC with SiC particle distribution in the matrix. The microstructure reveals that there are no voids or discontinuities and a reasonably uniform distribution of SiC particulates. There also was a slight agglomeration of SiC particles in the microscale, but good interfacial bonding between SiC particles and matrix material.

4.2. Fluidity

Fluidity measurements showed that the viscosity increases with increasing SiC content in the molten metal. Figures 6a and b show the photographs of spiral and strip fluidity. Figure 7 shows the results of strip and spiral fluidity. The base metal showed good flowability, and the metal matrix composite with 15% SiC poor flowability in both strip and spiral fluidity.

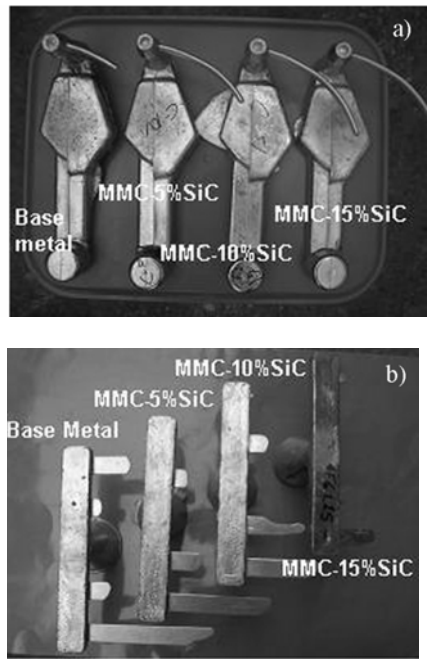

Fig. 6. Spiral fluidity castings (a) and strip fluidity castings (b)

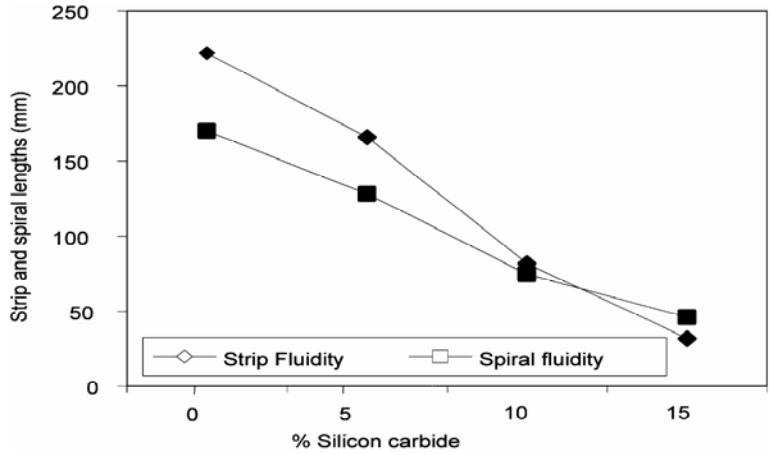

Fig. 7. Strip and spiral lengths for MMC with different SiC particles contents

4.3. Density and hardness measurements

The results of density measurements on the base metal and reinforced materials are shown in Figure 8. The results reveal that the presence of SiC particulates has little effect on the density of the MMCs. Since the density of the reinforced SiC particles is 2580 kg·mm^{-3} – almost the same as that of the base material (2630 kg·mm^{-3}) – not much change in the MMC density was observed.

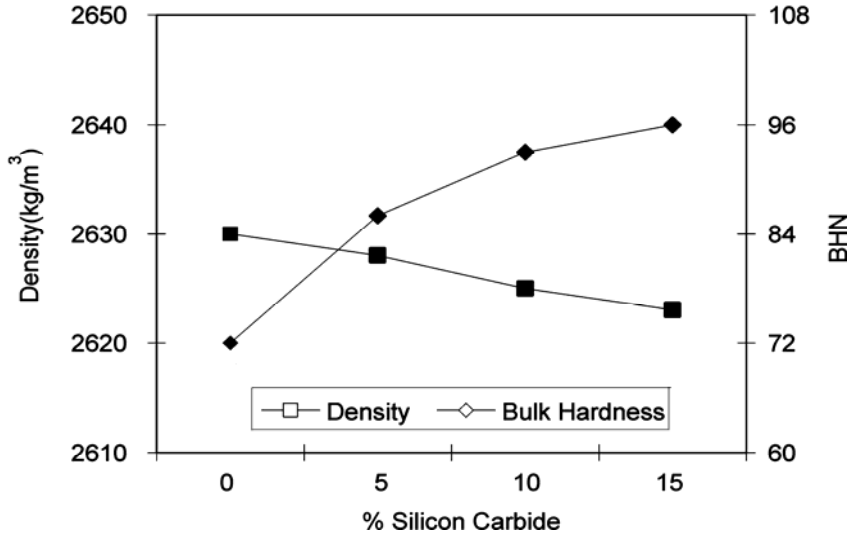

Fig. 8. Variation of density and bulk hardness with SiC contents

The results of microhardness measurements conducted on composite samples containing 15 wt. % of SiC particles are shown in Table 2. The measurements were performed using a 50 g load. The results indicate that hardness varies in the vicinity of SiC particulates, depending on the distance from the interface. The variation, however, does not show a clear trend. The hardness value is higher near the particle–matrix interface as compared to other regions. The lack of a clear trend in the variation of microhardness can be attributed to the influence of neighbouring particles, those beneath and on the sides, on the hardness of the matrix.

Table 2. Microhardness of MMC (SiC – 15 wt. %)

Distance [μm]	Test [Hv]		
	1	2	3
0	524	567	586
10	510	427	560
20	439	435	358
30	310	283	433
40	450	315	183

The results of bulk hardness measurements conducted on the monolithic and reinforced materials are as shown in Figure 8. The results reveal that an increase in the SiC particulate weight percentage in MMC increases the material bulk hardness.

4.4. Sliding wear behaviour

Figure 9 shows the results of the sliding wear behaviour of MMCs with 0%, 5%, 10%, and 15% of SiC. The normal load applied was 14.7 N, and the track velocity was 95 $m \cdot min^{-1}$. In all the test results it is evident that the resistance to wear increases with increasing silicon carbide content. The MMCs with low weight fractions of SiC underwent large wears, and the wear increased almost linearly with time. The base metal exhibits higher wear, and the MMC with 15% SiC showed lower wear.

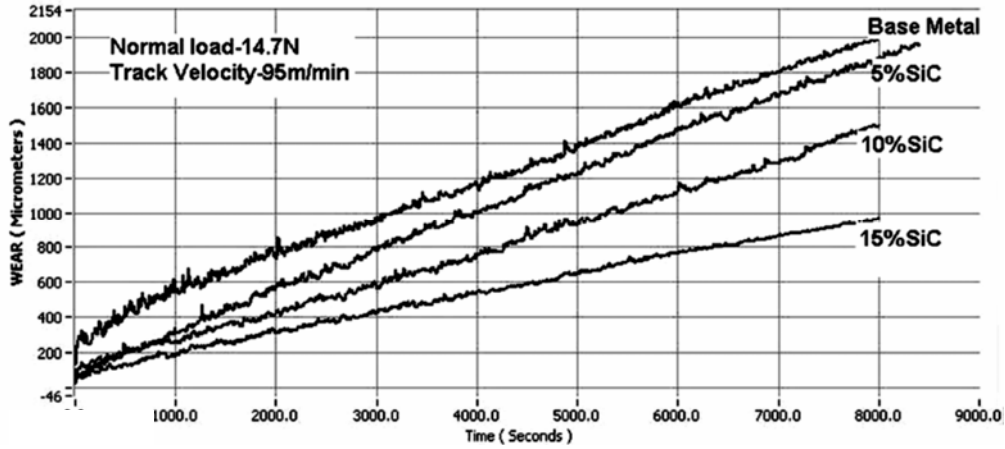

Fig. 9. Sliding wear behaviour of MMCs under different SiC contents

The amount of wear increases with increasing normal load. The sliding wear behaviour of MMC (15%SiC) for various normal loads is shown in Figure 10. With increasing normal load, MMCs underwent a transition from mild to severe wear.

Variation in sliding velocity was achieved by changing the rotational speed of the disc to 500 rpm, 600 rpm, 700 rpm and 800 rpm while keeping the track diameter constant at 30 mm. Figure 11 shows the wear behaviour curves for 15% of SiC MMC for the various sliding velocities. The amount of wear increased with increasing sliding velocity, undergoing a transition from mild to severe wear.

Optical microscopic examinations of the worn pin surfaces identified different wear mechanisms, working either alone or in combination, under the various sliding conditions. These are: abrasion, oxidation, adhesion, and thermal softening. In the following sections, the observed wear mechanisms are discussed in relation to the sliding conditions and wear rates, in order to better understand the tribological characteristics.

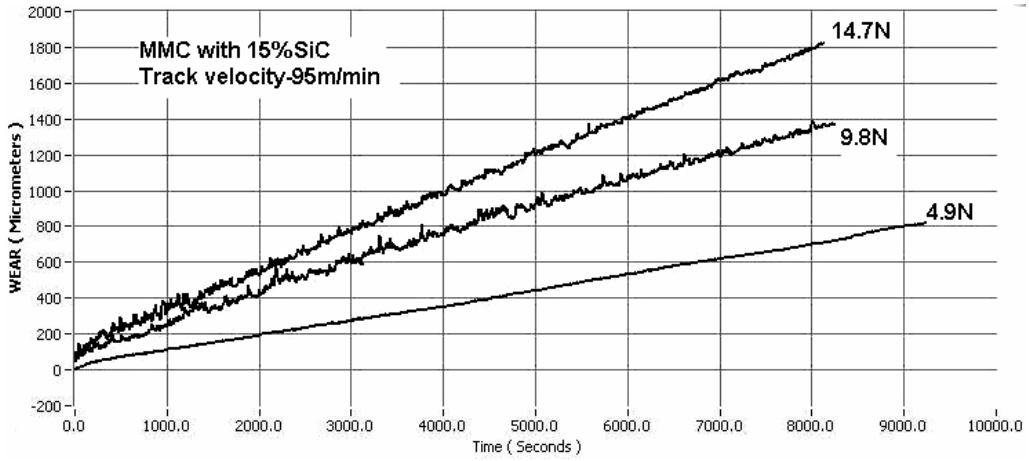

Fig. 10. Sliding wear behaviour of MMCs under different normal loads

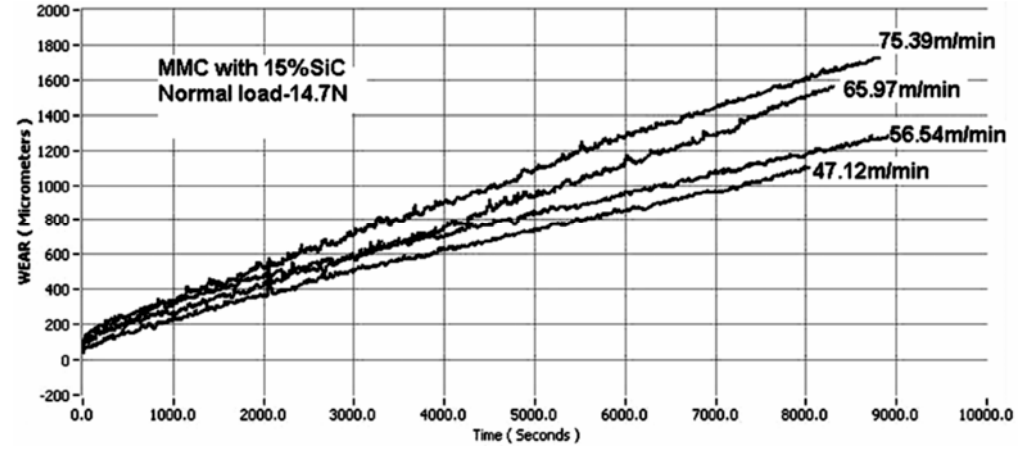

Fig. 11. Sliding wear behaviour of MMCs at different sliding velocities

Abrasion. A number of grooves, mostly parallel to the sliding direction, is evident on all the worn pins (Fig. 12). Grooving appears more severe at higher loads, 14.7N, and higher sliding velocities, 95 $m \cdot min^{-1}$ (Fig. 13). Grooves were less severe for lower loads and lower speeds. Such features are characteristics of abrasion, in which hard asperities of the steel counterface, or hard reinforced particles in between the contacting surfaces, plough or cut into the pin, causing wear by removing small fragments of material. The abrasion took place primarily via ploughing, in which material is displaced on either side of the abrasion groove without being removed, or through wedge forming, where tiny wedge-shaped fragments are worn only during initial contact with an abrasive particle [21]. The abrasion is extensive in the Al/SiC composites tested, due to the presence of dislodged and fractured SiC, which become trapped in the sliding interface and gets embedded in the counterface, contributing to three body abra-

sive wear. In addition, fractured SiC particles trapped between the sliding surfaces would also cause the abrasion of the steel disc, as would work-hardened fragments of matrix alloy and steel.

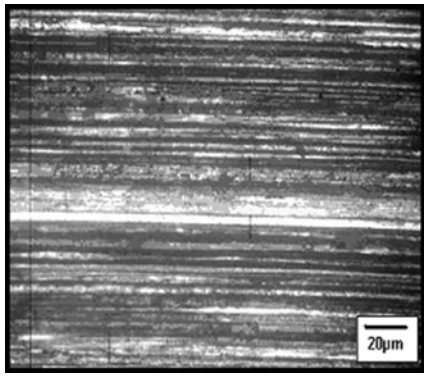

Fig. 12. Wear grooves on the worn pin surface

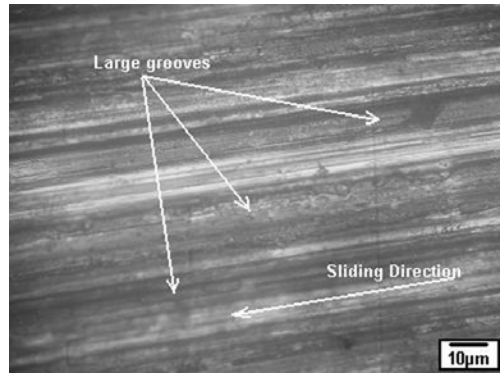

Fig. 13. Severe and large wear grooves

Oxidation. Under the optical microscope, dark surfaces are found to be covered extensively by a thin layer of fine particles (Fig. 14). Large amounts of fine powder are also present in the wear debris. These characteristics are indicative of oxidative wear, in which frictional heating during sliding causes oxidation of the surface, with wear occurring through the removal of oxide fragments [22]. Over continuous sliding, oxide wear debris fills the valleys on the pin surface and is compacted into a protective layer preventing metallic contact, and the wear rate of the composite drops accordingly [23].

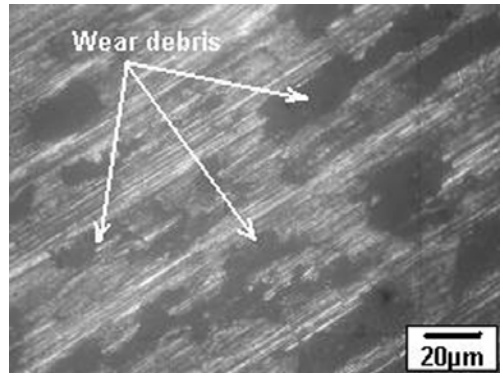

Fig. 14. Layer of oxide particles covering wear surface

Thermal softening and plastic deformation. At higher sliding speeds (95 $m \cdot min^{-1}$) and higher loads (14.7 N) material transfer is evident on the pin surfaces, indicating plastic deformation. This was observed predominantly during the wear test of the base matrix material and of MMC with a small amount of SiC.

Under the most severe sliding condition – 95m·min^{-1} and 14.7 N – associated with a longer contact time of the surfaces, gross plastic deformation of the pin surface occurs and the material is extruded from the interface before re-solidifying around the periphery of the pin as in Figure 15a. When the sliding speed and applied load reach certain critical thresholds, temperatures at contacting asperities nearly reach the melting point of the matrix alloy, causing a gradual softening of the matrix and an increasing in wear. This type of wear is predominantly observed in MMC specimens containing smaller amounts of SiC and in the base metal.

In pins tested at higher speeds and 14.7 N load, layers of material are seen protruding for the composite with 15% SiC and large protrusions can be observed for MMC with 5% SiC at the trailing edge, indicating thermal softening (Fig. 15b).

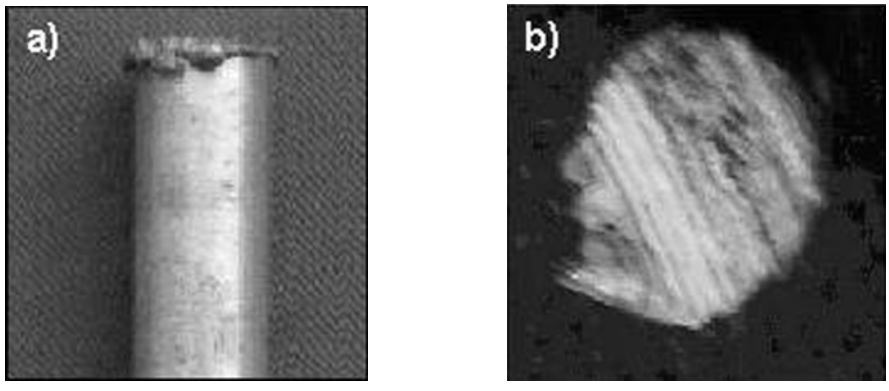

Fig. 15. Thermal softening and plastic deformation

Wear debris. The worn debris of the metal matrix composite with 15% of SiC is shown in Figure 16. A substantial quantity of wear debris was generated during the tests. The debris has three major morphologies: particle-like and flake-like aluminium, and a black powder of fractured SiC particles. A typical example of the flake type Al is shown in Figure 16a, namely flake-like wear debris obtained under 14.7 N and 95 m·min^{-1} on 15% SiC MMC specimens. These flakes have irregular shapes: some look like sponges, some are circular lumps, while some have sharp and angular features. On the other hand, Figure 16b shows flake-like aluminium debris of medium size collected from the same test. In fact, these two types of wear debris could be observed in all tests, the only difference being the relative amount of each type, and this could be influenced to a great degree by the normal load and sliding velocity. Figure 16c shows the dark powder-type mixture containing fractured SiC particles and small Al particles. As a whole, wear debris at 14.7 N load and 95 m·min^{-1} is dark in colour and mainly in the form of fine particles or flakes. At a load of 4.9 N, the debris formed consists of fine particles, which appear due to the shear fracture during the wear test. The volume of the wear debris increases with increasing normal load and sliding velocity, resulting in greater wear loss for higher loads and sliding velocities.

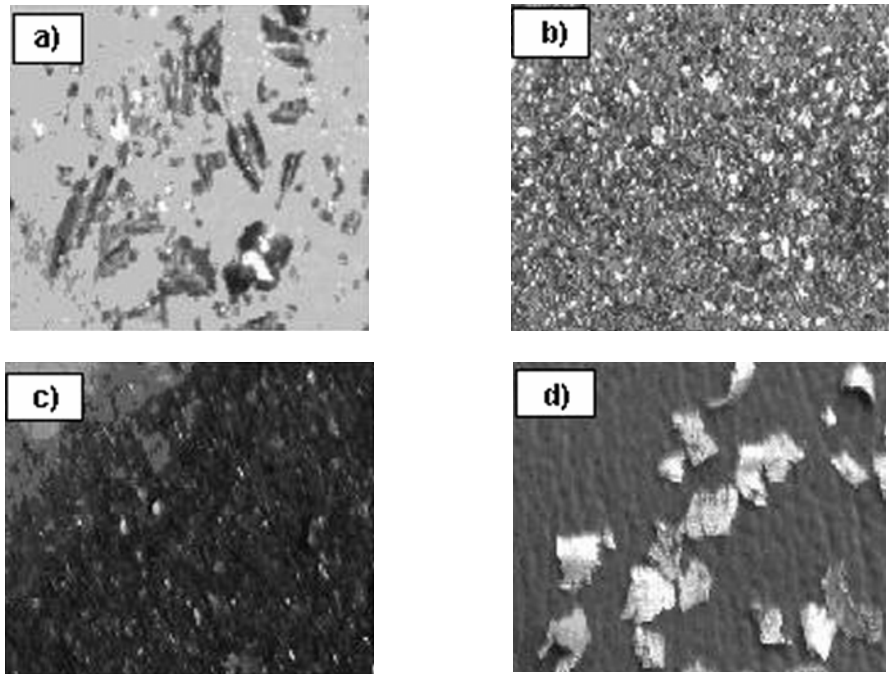

Fig. 16. Photomicrographs of wear debris

4.5. Slurry erosive wear

The results of slurry erosive wear are shown in Figure 17. The results show an increase in slurry wear resistance with increasing SiC content. Compared to the base metal, the composite with 15% SiC showed less weight loss. The presence of SiC particles essentially improved wear resistance during the initial 8–10 hours. After this time of testing, however, weight loss was found to be almost zero in all cases. The decrease in weight loss is due to the formation of a passive layer on the surface of the specimen, which retards wear by acting as a protective layer. The erosion–corrosion of MMCs usually proceeds by three different mechanisms: (i) corrosion of the matrix alloy, (ii) abrasion/erosion of the matrix as well as passive layer formation over the specimen, and (iii) fragmentation and removal of reinforcing agent dispersoids from the specimen surface by the impact of suspended erodent. Corrosion of the matrix takes place by an oxidation reaction [24], in which Al^{3+} is released from the matrix to the slurry. This results in the exposure of a large fresh area of the specimen surface to the slurry, and causes further removal of matrix alloy and hence a higher rate of weight loss during the initial stage. As time progresses, the slurry adjacent to the specimen surface becomes saturated with Al^{3+}, resulting in a reduction in the pH of the slurry. As a result, the dissolution rate of Al^{3+}in the slurry is reduced and the excess Al^{3+} is deposited over the specimen surface, which combines with OH^- to form $Al(OH)_3$ over the specimen surface. This passive layer, as long as it is not broken,

protects the matrix from direct contact with the slurry and lowers the rate of weight loss. Additionally [25, 26], the gas evolving during corrosion is entrapped in crater

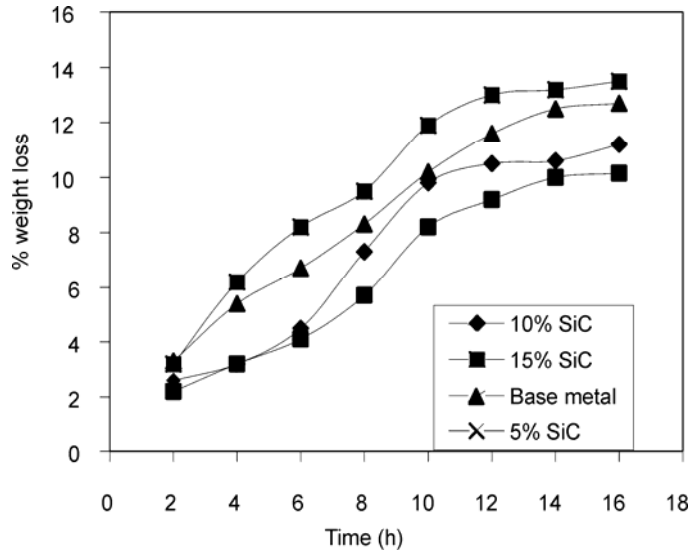

Fig. 17. Weight loss during slurry erosive wear as SiC content was varied

microsites (formed due to particulates escaping or the removal of matrix) and protects them from the slurry, which further lowers the rate of weight loss.

4.6. Fog corrosion

Figure 18 shows the results of a salt solution fog corrosion test. The resistance to corrosion is good in the non-reinforced specimens as compared to those being rein-

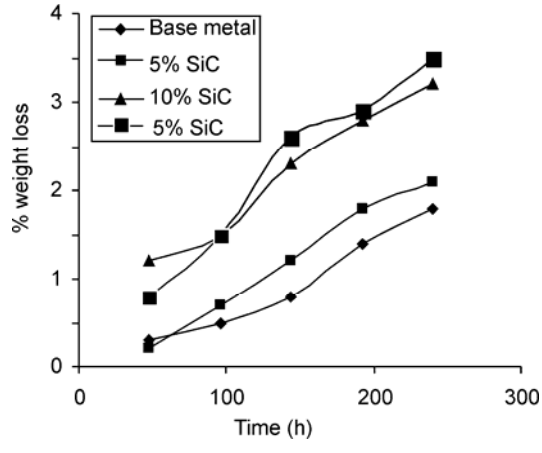

Fig. 18. Weight loss during fog corrosion test in samples with various SiC rates

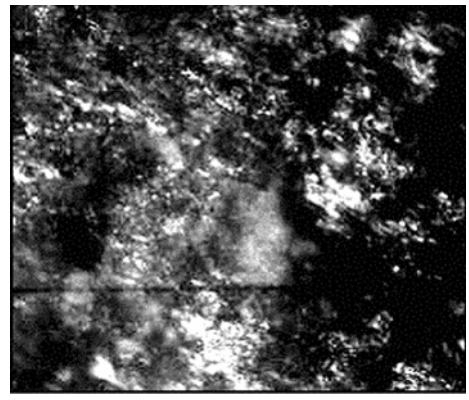

Fig. 19. Optical micrograph of corroded MMC

forced. The formation of an aluminium oxide layer is visible within 24 hours of commencing the test. The type of corrosion was found to be pitting corrosion. After 24 hours, it is observed that the formation of pit is more rapid in reinforced samples than in non-reinforced ones. SiC particles act as sites initiating pits. As is evident from Figure 19, there is a build up of corroded particle debris in the pits. Pits initiate at flaws within the surface film and at sites where the film is damaged mechanically under conditions when self-repair will not occur. Places where the matrix surface is broken on the interface between the reinforcement and the matrix will act as pit initiators. A corrosion pit is a unique type of anodic reaction and the autocatalytic process. The corrosion process within a pit produces conditions both stimulating and necessary for the continuing activity of the pit. This is illustrated schematically in Figure 20. Since pits arise at flaws, and the interface between matrix aluminium and a reinforced particle is a flaw, the metal aluminium is pitted by aerated sodium chloride solution. Rapid dissolution of aluminium occurs within a pit, while oxygen reduction takes place on adjacent surfaces. This process is self-stimulating and self propagating.

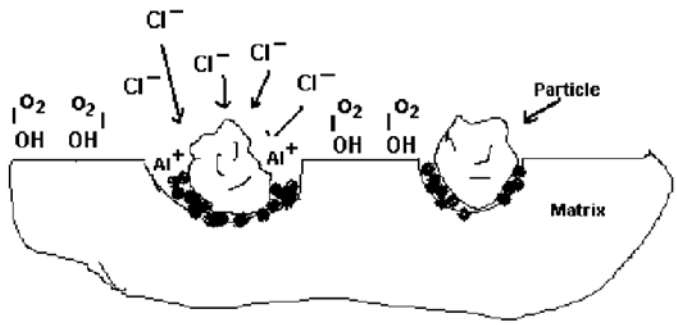

Fig. 20. Schematic autocatalytic process in pitting corrosion

A rapid dissolution of aluminium within the pit tends to produce an excess of positive charge in this area, resulting in the migration of chloride ions to maintain electro neutrality. Thus, there is a high concentration of aluminium chloride in the pit, and

a high concentration of hydrogen ions as a result of hydrolysis. Both hydrogen and chloride ions stimulate the dissolution of aluminium matrix and the entire process accelerates in time. Since the solubility of oxygen is virtually zero in concentrated solutions, no reduction of oxygen takes place within a pit. Cathodic oxygen reduction on surfaces adjacent to pits tends to suppress the corrosion there by protecting the matrix metal adjacent to the pit.

5. Conclusions

Metal matrix composites containing 5%, 10%, and 15% of SiC were synthesized successfully by the vortex method. Macrostructure and microstructure revealed a near uniform distribution of SiC particles in the centre portion of the casting. There was a slight agglomeration of SiC particles, however, on macroscopic scale. There was not much change in the density of MMC with the reinforcement of SiC particles. The bulk hardness and sliding wear resistance of MMC increase with increasing SiC content. Increasing normal load and sliding velocity increase the magnitude of wear. Different wear mechanisms were found to operate under different test conditions, varying in normal load, per cent of SiC content and sliding velocity. These are abrasion, oxidation, thermal softening, and plastic deformation. Slurry erosive wear resistance increases with increasing if SiC content. The formation of passive layers on the surface of the slurry erosive specimens decreased wear loss by forming protective layers against the impact of slurry. The corrosion resistance of reinforced samples decreases with increasing SiC content.

References

[1] SHIPWAY P.H., KENNEDY A.R., WILKES A.J., Wear, 216 (1998), 160.
[2] MA Z.Y., LIUNG Y.N., ZHANG Y.Z., LU Y.X., BI J., Mater. Sci. Tech, 12 (1996), 751.
[3] PARIMALA BAI B.N., RAMASESH B.S., SURAPPA M.K., Wear 157 (1992), 295.
[4] VENKATARAMAN S., SUNDARARAJAN S., Acta Mater., 44 (1996), 451.
[5] SATO A., MEHRAHIAN R., Metall. Trans. B, 7 (1976), 443.
[6] WANG A., RACK H.J., Mater. Sci. Eng., A247 (1991), 211.
[7] WILSON S., ALPAS A.T., Wear, 196 (1996), 270.
[8] MARTIN A., MARTINET M.A., LLORCA J., Wear, 193 (1996), 169.
[9] CHUNG S., HWANG B.H., Tribology Int., 27 (1994), 307.
[10] HUSKING F.M., FOLGAR PORTILLO F., WUNDERLIN R., MEHRABIAN R., J. Mater. Sci., 17 (1982), 477.
[11] SANNINO A.P., RACK H.J., Wear, 197 (l996), 151.
[12] SANNINO A.P., RACK H.J., Wear, 189 (1995), 1.
[13] DAS S., MONDAL D.P., DASGUPTA R., PRASAD B.K., Wear, 236 (1999), 295.
[14] SAXENA M., MODI O.P., PRASAD B.K., JHA A.K., Wear, 169 (1993), 119.
[15] MCINTYRE J.F., CONRAD R.K., GOLLEDGE S.L., Corrosion, 46 (1996), 902.
[16] TRAZASKOMA P.P., Corrosion, 46 (1996), 402.
[17] YU S.Y., ISHII H., CHUANG T.H., Metall. Mater. Trans., A 27 (1996), 2653.
[18] ROHATGI P.K., GUO R.Q., KESHAVARAM B.N., Key Eng. Mater., 104 (1995), 283.

[19] MANOHARAN S., LEWANDOWSKI J.J., Acta Metall., 38 (1990), 489.
[20] SURAPPA M.K., ROHATGI P.K., Metal Tech., 4 (1981), 41.
[21] QUINN T.J.F., J. Appl. Phys., 13 (1962), 33.
[22] STOTT F.H., WOOD G.C., Tribol. Int., 11 (1978), 211.
[23] SUH N.P., Wear 44 (1977), 1.
[24] SLREHBLOW H.H., International Congress on Metallic Corrosion, June 1984, National Research Council, Canada, 1984, p. 99.
[25] TURENNE S., SIMROD D., FIEST M., Wear, 149 (1991), 187.
[26] TURENNE S., CHATIGNY Y., SIMARD D., CARON S., MASOUNAVE J., Wear 141 (1990), 147.

Received 31 May 2005
Revised 10 July 2005

Materials Science-Poland, Vol. 24, No. 2/1, 2006

Progressive evolution from giant magnetoresistance to anisotropic magnetoresistance in CoNi–Al_2O_3 granular films

CH. WANG[1*], Y. RONG[2], T.Y. HSU (XU ZUYAO)[2]

[1]Department of Physics, Liaocheng University, Liaocheng City, Shandong Province, 252000, P.R.China

[2]School of Materials Science and Engineering, Shanghai Jiaotong University, Shanghai 200030, P.R.China

A series of CoNi–Al_2O_3 granular films were prepared with a magnetron controlled sputtering system. Their magnetic-transport properties were measured by the conventional four-probe method. Results indicate that the longitudinal GMR effect reaches a maximum of –2.1% at about 35 vol. % of CoNi. Meanwhile, the GMR effect is dominant when the volume fraction is less than about 50 vol. %, whereas AMR predominates in films when the volume fraction is larger than about 50 vol. %. This suggests that there exists a progressive evolution from GMR to AMR through the percolation region in CoNi–Al_2O_3 granular films.

Key words: *CoNi–Al_2O_3 granular film; giant magnetoresistance; anisotropic magnetoresistance*

1. Introduction

Extensive studies of spin-dependent transport properties were triggered recently by the discovery of the so-called giant magnetoresistance (GMR) effect. This novel effect which was first discovered in the magnetic Fe/Cr multilayer [1] and later in heterogeneous granular films with ferromagnetic granules embedded in a non-magnetic metallic matrix [2, 3] shows that the resistance of films could exhibit large changes – of the same order of magnitude as the resistance itself – upon applying a magnetic field and has potential technical applications in the information industry. Although the exact mechanism of GMR remains elusive, it is attributed to spin-dependent scattering being dominant at the interface between ferromagnetic granules and a matrix, as well as within the ferromagnetic granules [4]. Another direction in the research of spin-dependent transport phenomena in heterogeneous granular films is granular systems where small ferromagnetic granules are embedded in an immis-

*Corresponding author, e-mail: wcz102@sjtu.org

cible insulating matrix. Giant magnetoresistance and the relative magnetic properties of a mixture depend on the volume fraction of ferromagnetic granules. At low-volume fractions, ferromagnetic granules are isolated from each other and electric transport proceeds by intergranular tunnelling, thus in these systems the GMR effect is also called tunnelling magnetoresistance (TMR). When the volume fraction of ferromagnetic granules increases above a certain threshold, individual granules will form a network structure [5] with a continuous metallic conductance path. In the latter, the films will exhibit anisotropic magnetoresistance (AMR), an effect first discovered in ferromagnetic metals by Willam Thomson in 1857 [6] and used in magnetic field detectors for digital recording and magnetic bubbles.

Being different from the mechanism of GMR or TMR, the theoretical basis of AMR takes into account spin-orbit interaction and the d band splitting commonly found in bulk ferromagnetic materials [7]. Therefore, the GMR (or TMR) and AMR effects should have a certain relationship in granular films. Until now, however, little work has been done to study the relationship between GMR and AMR. Since CoNi –Ag alloys can exhibit both AMR and GMR effects [8] and Co–Al_2O_3 granular films can show a typical GMR effect [9], a new CoNi–Al_2O_3 granular system can be expected to be a good candidate for understanding the relationship between GMR and AMR. In this paper, we reported the transport properties of a series of CoNi–Al_2O_3 granular films. We found that they exhibit mainly GMR effects below the ferromagnetic percolation threshold and AMR effect above the ferromagnetic percolation threshold, and at the passage of the percolation threshold there is a progressive evolution of TMR to AMR.

2. Experimental procedure

The CoNi–Al_2O_3 granular films were sputtered onto a glass substrate at room temperature (300 K) with an spc350 multi-target magnetron controlled sputtering system. A CoNi target (the weight ratio of Co and Ni 1:1) and Al_2O_3 target (99.9% purity) were separately installed on two independently controlled R.F. cathodes, and were alternatively employed to sputter the films. The thickness of films for MR measurement was about 300 nm as measured by α-step meter. The volume fraction of CoNi in the CoNi–Al_2O_3 films was controlled by changing the sputtering power of the CoNi target and was determined by an energy dispersive spectrum (EDS) obtained with a JEM-2010 transmission electron microscope (TEM). The base pressure was about 3×10^{-3} Pa and the sputtering gas (Ar) pressure was 1.7×10^{-1} Pa. The MR effect was measured by the conventional four-probe method for applied fields up to 1.25 T.

3. Results and discussion

The variation of resistivity of CoNi–Al_2O_3 granular films as a function of volume fraction of granules was measured without any applied field at room temperature, as

shown in Figure 1. The resistivity can change by over four orders of magnitude when the volume fraction of ferromagnetic granules changes from about 17 vol. % to 65 vol. %. With the increasing volume fraction of granules, the resistivity decreases slowly at first, and changes sharply at about 50 vol. % when the percolation threshold of granular films is crossed [10], indicating that conduction proceeds by metallic conducting over a ferromagnetic network above 50 vol. % and by tunnelling conduction below 50 vol. %.

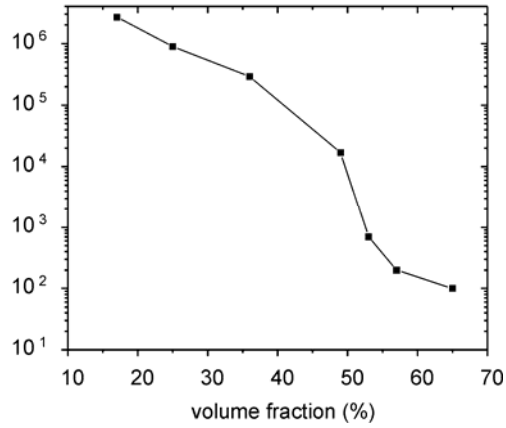

Fig. 1. Measured room resistivity vs. volume fraction of granules in CoNi–Al_2O_3 films

As mentioned above, it is clear that the conduction mechanism of CoNi–Al_2O_3 granular films varies with the volume fraction of granules, leading to the conclusion that the GMR or AMR effect dominates in granular films at different volume fractions. Figure 2 shows the dependence of longitudinal GMR and transverse GMR on the applied field for various volume fractions of CoNi granules. When the volume fraction of granules is less than about 49%, the longitudinal MR is negative (Fig. 2a–c), and for volume fractions above 49% it is positive (Fig 2d, e) except for a little part of negative MR at higher applied fields (Fig. 2d). On the other hand, transverse GMR is always negative in the above films.

Figure 3 shows the dependence of longitudinal GMR on the volume fraction of granules. Here, longitudinal GMR effects are calculated according to

$$\text{GMR} = \frac{\Delta\rho}{\rho} = \frac{\rho(H) - \rho(0)}{\rho(0)}$$

It is clear that longitudinal GMR first increases up to about –2.1% at the volume fraction of about 35% CoNi, and then decreases with the increasing volume fraction. Being different from longitudinal GMR, however, the AMR effect increases monotonically with increasing volume fraction, as seen in Figure 4. In this case

$$\text{AMR} = \frac{\rho_{\text{II}}(H) - \rho_{\perp}(H)}{\rho_{\text{II}}(0)/3 + 2\rho_{\perp}(0)/3}$$

where $\rho(H)$ and $\rho(0)$ stand for the resistivities in the applied field and initial zero field, respectively, and $\rho_{\parallel}$ and $\rho_{\perp}$ represent resistivities with the current parallel and perpendicular to the applied field in the plane of the samples [7].

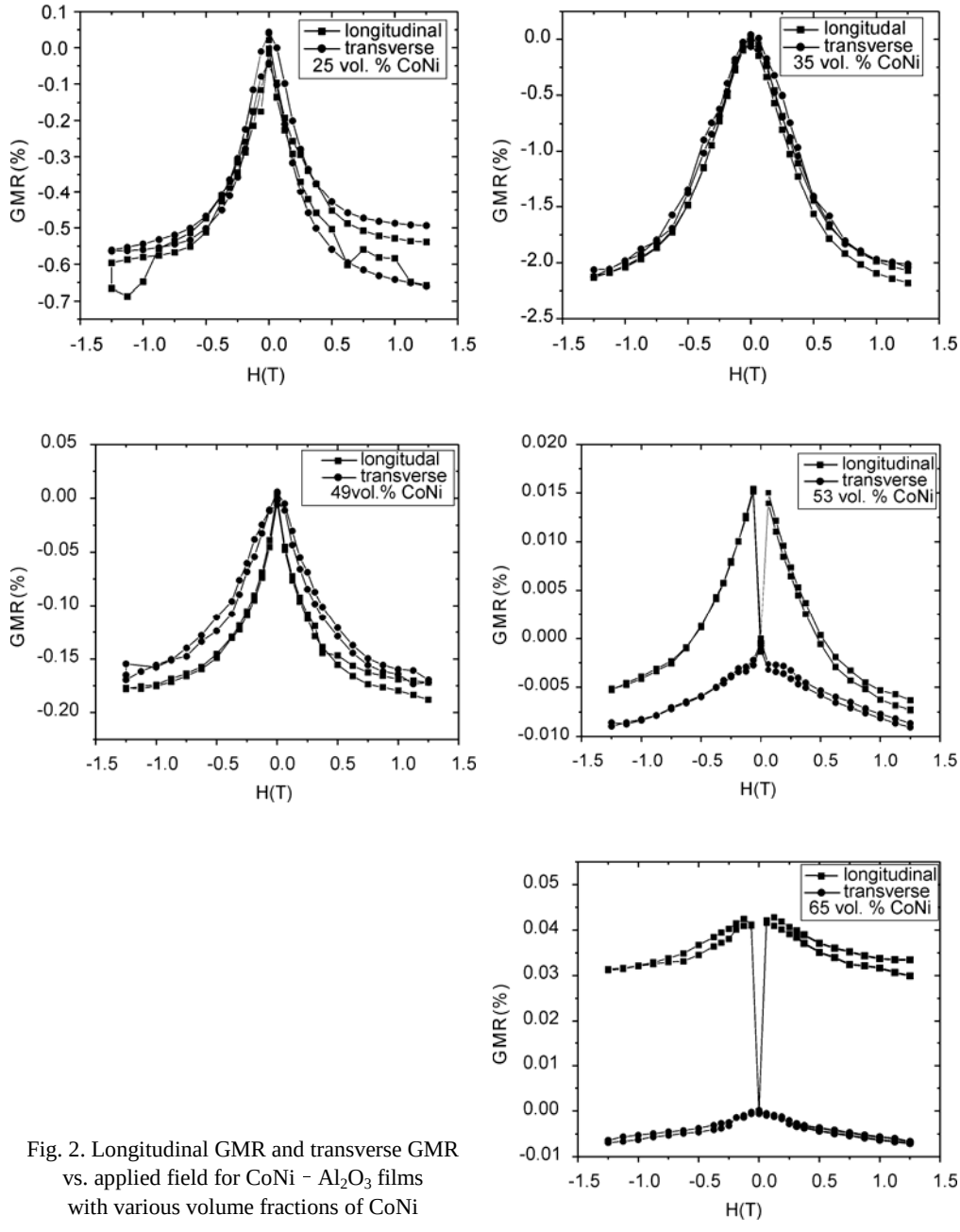

Fig. 2. Longitudinal GMR and transverse GMR vs. applied field for CoNi – Al_2O_3 films with various volume fractions of CoNi

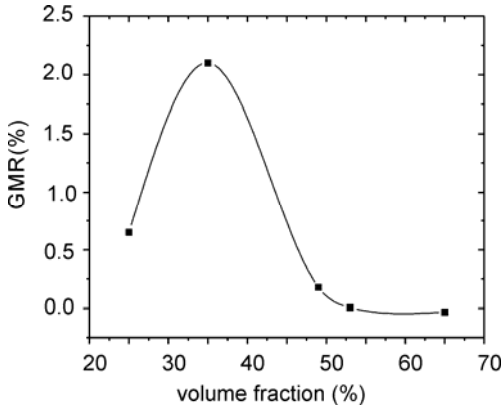

Fig. 3. Dependence of longitudinal GMR on the volume fraction of CoNi granules in CoNi–Al_2O_3 films

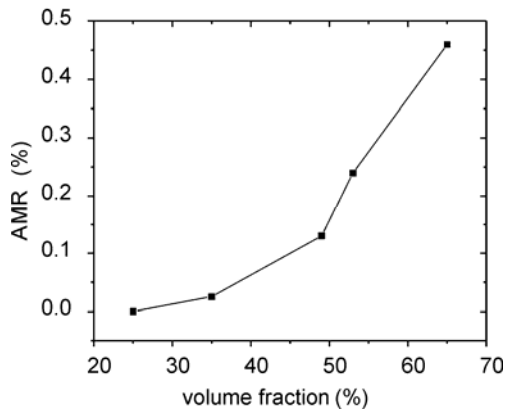

Fig. 4. Dependence of AMR on the volume fraction of CoNi granules in CoNi–Al_2O_3 films

All values of GMR and AMR were measured at H = 12.5 kOe (1×10^6 A/m). Comparing Figure 3 with Figure 4, it is apparent that in samples with lower volume fractions of granules, longitudinal GMR is negative while the AMR effect is negligible, indicating that GMR dominates in magnetic granular films. For the volume fractions of granules larger than 35 vol. %, the longitudinal GMR decreases, while AMR increases gradually and reaches 0.46% in our experiments at the volume fraction of 65 vol. %, indicating that the AMR effect predominates in films with higher volume fractions. The AMR effect will tend to the value of CoNi bulk alloy with increasing volume fraction, which can be expressed as follows. It is obvious that when the volume fraction of granules is larger than the percolation threshold, all CoNi particles coalesce and gradually form a connecting network with metallic conductance, and as a consequence, GMR vanishes. In the case of a connecting network, however, spin-orbit coupling can be enhanced as in the CoNi ferromagnetic bulk, and thus AMR dominates in granular films. When the volume fraction of granules gradually falls below the percolation threshold, electric transport will start to be governed by the tunnel current between CoNi particles separated by the Al_2O_3 matrix [11], since the connecting network is broken and large multidomain CoNi granules are separated into small single-domain or superparamagnetic granules. It follows that when these magnetic particles are magnetized under an applied field, the GMR effect will appear due to the spin-dependent tunnelling effect, and increase with decreasing granule volume fraction until a peak value is reached. After this, as the volume fraction decreases further, CoNi particles are far apart, i.e. the thickness of Al_2O_3 tunnelling barriers become larger than the spin diffusion length, and the spin-flip tunnelling process may occur, giving rise to a drop in GMR [12]. On the other hand, spit-orbit coupling gradually weakens due to granules being separated when their volume fraction is less than the percolation threshold, leading to a weak AMR effect.

4. Conclusions

In summary, in CoNi–Al_2O_3 films, the longitudinal GMR effect reaches a maximum of –2.1% at about 35 vol. % CoNi and the GMR effect is dominant when the volume fraction is less than about 50 vol. %, whereas AMR predominate in films when the volume fraction is larger than about 50 vol. %. This suggests that a progressive evolution from GMR to AMR occurs in the percolation region of CoNi–Al_2O_3 granular films.

Acknowledgements

The project was financially supported by the National Nature Science Foundation of China under Grant No.50071033 and Hi-Tech Research and Development Program of China under Grant No. 2004AA32G090.

References

[1] BAIBICH M.N., BROTO J.M., FERT A., NGUYEN VAN DAU F., PETROFF F., Phys. Rev. Lett., 61 (1988), 2472.
[2] BERKOWITZ A.E., MITCHELL J.R., CAREY M.J., YOUNG A.P., ZHANG S., SPADA F.E., PARKER F.T., HUTTEN A., THOMAS G., Phys. Rev. Lett., 68 (1992), 3745.
[3] XIAO J.Q., JIANG J.S., CHIEN C.L., Phys. Rev. Lett., 68 (1992), 3749.
[4] ZAHN P., BINDER J., MERTIG I., ZELLER R., DEDERICHS P.H., Phys. Rev. Lett., 80 (1998), 4309.
[5] ABELES B., SHENG P., COUNTS M.D., ARIE Y., Adv. Phys., 24 (1975), 407.
[6] Thomson W., Proc. Roy. Soc., 8 (1857), 546.
[7] MCGUIRE T.R., POTTER R.I., IEEE Trans. Magn., 4 (1975), 1018.
[8] NI G., XU Q.Y., YIN X.B., SANG H., TANG S.L., DU Y.W., Scripta Mater., 44 (2001), 1437.
[9] MITANI S., TAKAHASHI S., TAKANASHI K., YAKUSHIJI K., MAEKAWA S., FUJIMORI H., Phys. Rev. Lett., 81 (1998), 2799.
[10] CHIEN C.L., J. Appl. Phys., 69 (1991), 5267.
[11] OHNUMA M., HONO K., ONODERA H., PEDERSEN J.S., MITANI S., FUJIMORI H., Mater. Sci. Forum, 307 (1999), 171.
[12] YANG W., JIANG Z.S., DU Y.W., WANG W.N., Solid State Commun., 104 (1997), 479.

Received 23 June 2005
Revised 8 August 2005

Materials Science-Poland, Vol. 24, No. 2/1, 2006

Dry sliding wear behaviour of Al 2219/SiC metal matrix composites

S. BASAVARAJAPPA[1*], G. CHANDRAMOHAN[1], R. SUBRAMANIAN[2], A. CHANDRASEKAR[2]

[1]Department of Mechanical Engineering, PSG College of Technology, Coimbatore 641 004, India

[2]Department of Metallurgical Engineering, PSG College of Technology, Coimbatore 641 004, India

The present study deals with investigations relating to dry sliding wear behaviour of the Al 2219 alloy, reinforced with SiC particles in 0–15 wt. % in three steps. Unlubricated pin-on disc tests were conducted to examine the wear behaviour of the aluminium alloy and its composites. The tests were conducted at varying loads, from 0 to 60 N and a sliding speeds of 1.53 m/s, 3 m/s, 4.6 m/s, and 6.1 m/s for a constant sliding distance of 5000 m. The results showed that the wear rates of the composites are lower than that of the matrix alloy and further decrease with increasing SiC content. As the load increases, cracking of SiC particles occurs and a combination of abrasion, delamination, and adhesive wear is observed. The samples were examined using scanning electronic microscopy after wear testing and analysed.

Key words: *MMC; Al-based MMC; SiC; casting; wear; abrasion*

1. Introduction

The adoption of lightweight and high-performance metal matrix composites (MMCs) for aerospace, automobile, and consumer-related industries have been hindered by high costs of producing components of even minimally complex shape. Casting technology may be the key to overcome this problem, although several technical challenges exist. Achieving a uniform distribution of reinforcement within the matrix is one such challenge, which directly influences the properties and quality of the composite materials. Discontinuously reinforced aluminium metal matrix composites (DRAMMCs) are a class of composite materials that have desirable properties, such as low density, high specific stiffness, high specific strength, a controlled co-efficient of thermal expansion, increased fatigue resistance, and superior dimensional stability

* Corresponding author, e-mail: basavarajappas@yahoo.com

at elevated temperatures [1, 2]. The most commonly employed metal matrix composite system consists of an aluminium alloy reinforced with hard ceramic particles, the latter usually being silicon carbide, alumina [3, 4] or soft particles such as graphite or talc [5, 6]. These composite materials exhibit different strengthening mechanisms in comparison to conventional materials or continuous reinforced composites [7]. Thus, much research, both experimental and analytical, has been done to gain a better understanding of the mechanical behaviour of these composites and their excellent wear resistance. With continual development in fabrication techniques, MMCs have been able to replace more conventional metallic monolithic alloys (e.g., aluminium) in applications where light weight and energy saving are important design considerations. The presences of hard reinforcement phases (particulates, fibres, or whiskers) have endowed these composites with good tribological (friction and wear) characteristics. These properties, along with good specific strength and specific modulus, make them good candidate materials for many engineering applications where sliding contact is expected. All mechanical components that undergo sliding or rolling contact, such as bearings, gears, seals, guides, piston rings, splines, brakes and clutches, are subject to some degree of wear. Wear is a surface phenomenon that occurs by the displacement and detachment of material, because it usually implies a progressive loss of weight and alteration of dimensions over a period of time.

An extensive review work on the dry sliding wear characteristics of composites base on aluminium alloys have been undertaken by Sannino et al. [8], and abrasive wear behaviour by Deuis et al. [9]. In their studies and discussions, the effect of reinforcement volume fraction, reinforcement size, sliding distance, applied load, sliding speed, hardness of the counter face and properties of the reinforcement phase which influence the dry sliding wear behaviour of this group of composites are examined in greater detail. Sliding wear rate and wear behaviour were reported to be influenced by various wear parameters [10–13]. Lim et al. [14] studied the tribological properties of Al–Cu/SiC metal matrix composites and reported that along with increasing their mechanical properties, wear resistance also increased drastically, which effects the counter face.

In view of the above description, an attempt has been made in this study to improve the dry sliding wear behaviour of Al 2219 reinforced with SiC particles (SiCp) at different loads and speeds, such that it will be more relevant and appropriate for severe environments.

2. Experimental details

2.1. Materials

The metal matrix material selected for the present investigation was based on the Al–Cu–Mg matrix alloy, designated by the American Aluminium Association as

Al 2219. This matrix alloy was chosen, since it provides an excellent combination of strength and damage tolerance both at elevated and cryogenic temperatures. The SiC particles which were used to fabricate the composite had an average particle size of 25 μm and average density of 3.2 g/cm^3. The amount of SiC particle reinforcement varied from 0 to 15 wt. % in three steps. The nominal chemical composition of the matrix alloy is given in Table1.

Table 1. Composition of Al 2219 (wt. %)

Element	Si	Fe	Cu	Mn	Mg	Zn	V	Ti	Zr	Al
Content	0.20 max.	0.30 max.	5.8–6.8	0.2–0.4	0.02 max.	0.10 max.	0.05–0.15	0.02–0.1	0.1–0.25	balance

2.2. Preparation of the composite

The liquid metallurgy technique [15–17] was used to fabricate the composite specimens. This method is the most economical route to obtain composites with discontinuous fibres or particulates. In this process, the matrix alloy (Al 2219) was first superheated above its melting temperature to create a vortex in the melt using a stainless steel mechanical stirrer coated with aluminite (to prevent the migration of ferrous ions from the stirrer material to the aluminium alloy melt). At this stage, the preheated SiC particles were introduced into the slurry and the temperature of the composite slurry was increased until it was in a fully liquid state, and the stirring was continued for about five minutes at an average stirring speed of 300–350 rpm. Passing nitrogen subsequently degassed this melt. The melt was then superheated above the liquidus temperature (7 000 ºC) and finally poured into a permanent cast iron mould of 10 mm in diameter and 50 mm high.

2.3. Microscopy studies

The fabricated Al 2219/SiCp composites were subject to metallographic examination in order to establish their structural characteristics. The composite specimens

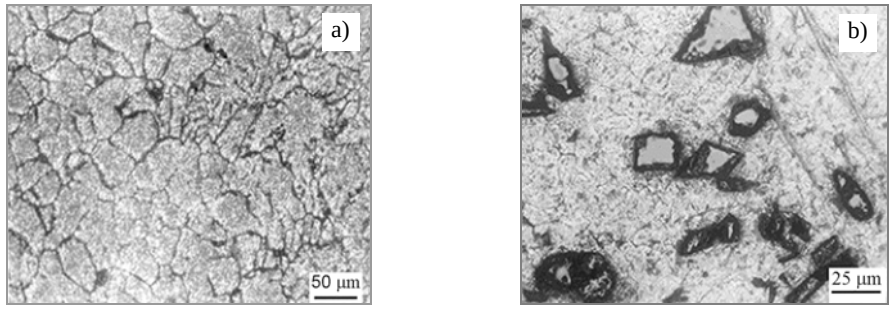

Fig. 1. Micrographs of: a) Al 2219, b) of Al 2219–10% SiCp

10 mm×20 mm in size were cut from the as-cast composite specimens for microstructural examinations. The specimens were carefully polished for metallographic examination. The samples were observed using a Carl Zeiss metallograph. Figures 1a, b show the optical micrographs of the Al 2219 alloy and its composite with a 10 wt. % of reinforcement. The figures show a uniform distribution of SiC particles in the aluminium matrix.

2.4. Wear testing of specimens

A pin-on-disc test apparatus was used to investigate the dry sliding wear characteristics of the aluminium alloy and Al-SiCp composites as per ASTM G99-95 standards. Wear specimen 10 mm in diameter and 40 mm high were cut from as-cast samples, machined, and then polished metalographically. Wear tests were conducted with loads ranging from 10 to 60 N and sliding speeds of 1.53 m/s, 3 m/s, 4.6 m/s, and 6.1 m/s for a sliding distance of 5000 m. All tests were conducted at room temperature. The initial weight of the specimens was measured using a single pan electronic weighing machine with an accuracy of 0.0001g. During the test, the pin was pressed against the counterpart rotating against an EN32 steel disc (hardness 65 HRc) by applying the load. All the specimens followed a single-track, 114mm in diameter, with a tangential force. A friction-detecting arm connected to a strain gauge held and loaded the pin specimen vertically into the rotating hardened steel disc. The frictional traction experienced by the pin during sliding was measured continuously by a PC-based datalogging system. After running through a fixed sliding distance, the specimens were removed, cleaned with acetone, dried, and weighed to determine the weight loss due to wear. The differences in weight measured before and after tests gives the wear of the composite specimen. The wears of the composite specimens were studied as a function of the volume percentage of reinforcement, sliding distance, applied load, and sliding velocity.

3. Results

3.1. Wear characteristics

Figure 2 shows the variation of wear volume loss with sliding distance for both as-cast aluminium alloy 2219 and Al-SiCp composites with varying percentages of SiCp reinforcement. It can be seen that as the sliding distance increases, the wear of both the composites as well as the unreinforced alloy increases. The wear of the unreinforced alloy is more than that of the composites for all sliding distances. Further, as the percentage of reinforcement increases, the wear of the composite decreases. There is not much change in wear during the initial phase of the sliding distance for composites with different percentages. The incorporation of SiCp particles into the Al 2219 alloy improves the sliding wear resistance as compared to the unreinforced alloy.

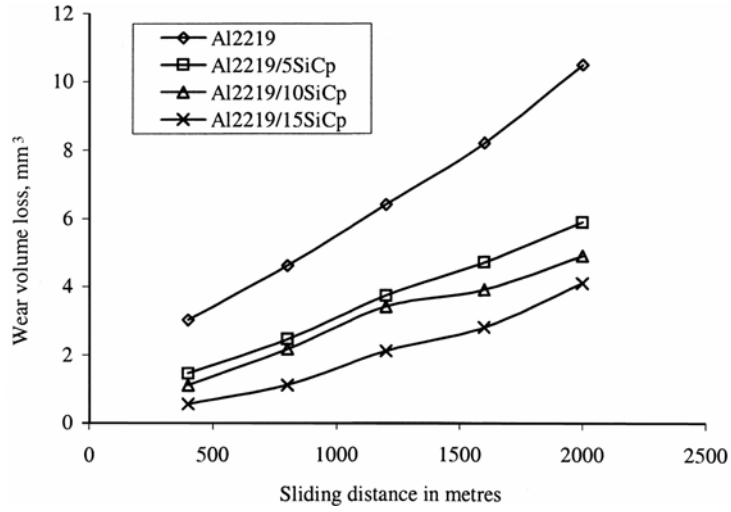

Fig. 2. Variation in volume loss with sliding distance for various composites and the alloy at a sliding speed of 1.53 m/s and load of 20 N

Figure 3 shows the variation in volume loss versus different percentages of SiCp reinforcement at different sliding distances at a constant sliding speed of 1.5 m/s and for a 40 N load for a fixed sliding distance of 5000 m. As the reinforcement content increases, the wear resistance of the composite increases. A drastic decrease in wear volume loss was observed for composites with 05 percent of SiCp. As the amount of reinforcement increases, the wear resistance increases for all sliding distances.

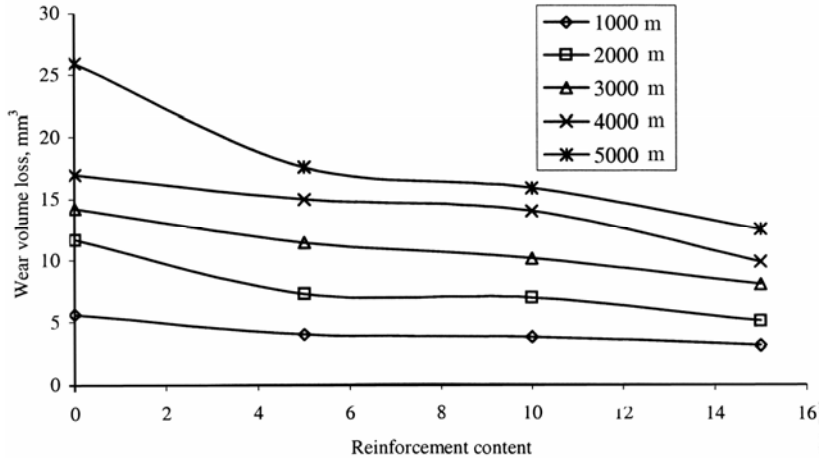

Fig. 3. Variation in volume loss vs. percentage of SiCp reinforcement at various sliding distances with a sliding speed of 1.5 m/s and 40 N load

Figure 4 shows the variation of the wear rate with sliding speed for the unreinforced alloy and for composites with different amounts of SiCp (5%, 10%, and 15%).

The wear rate of both unreinforced alloy and the composites decreases as the sliding speed increases up to 3 m/s. At a speed of 4.6 m/s, only the wear trend of the unreinforced alloy changes from mild to severe, while the composites continue to show the same trend. At a speed of 6.1 m/s, the composite wear rate curve pattern changes to severe wear. The unreinforced alloy shows seizes at 6.1 m/s, whereas as the composite does not. Further, the wear rate of the composite decreases as the amount of reinforcement. Heavy noise and vibration were observed during the process and transfer of the pin material to the disc was also observed.

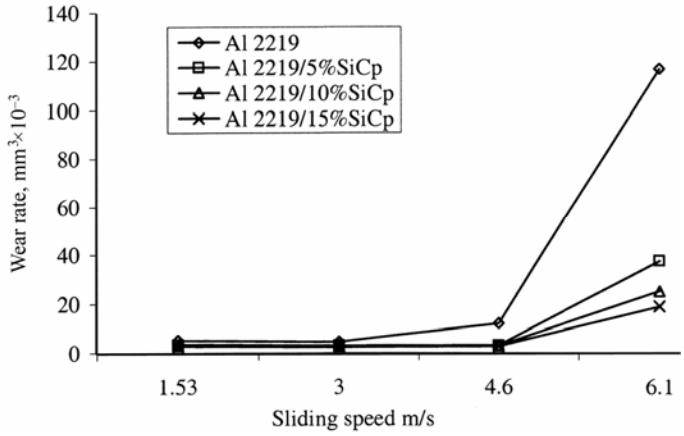

Fig. 4. Variation in wear rate with sliding speed for both composites and the alloy at a fixed load of 40 N and fixed sliding distance of 5000 m

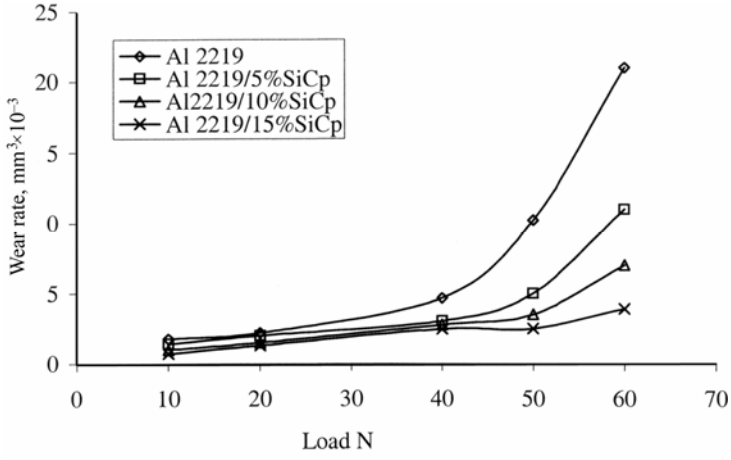

Fig. 5. Variation in wear rate with the applied load for various composites and the alloy for a fixed distance of 5000 m

Figure 5 presents the dependence of wear rate on the applied load for a fixed sliding speed of 3 m/s. Mild wear was observed for a small applied load, but as the load

was further increased up to 20 N, the wear rate of the unreinforced alloy and composite increased. At the load of 20 N, the wear pattern changes for the unreinforced alloy, while the composite follows the same trend up to 50 N (the unreinforced alloy seizes at this load). At a 60 N load, the SiCp reinforced composites show a change in the wear rate pattern to severe wear. The percentage of wear rate also decreases with further increasing the reinforcement content. From the above graphs, the positive effect of the reinforcing silicon carbide particles in reducing the wear rate of materials can be seen. A similar trend was also observed independently for different wear distances as a function of load and speed.

3.2. Examination of wear test specimens

Scanning Electron Microscope (SEM) studies of the worn specimens were carried out using a JEOL model SEM. SEM Micrographs are shown in Fig. 6 of the worn

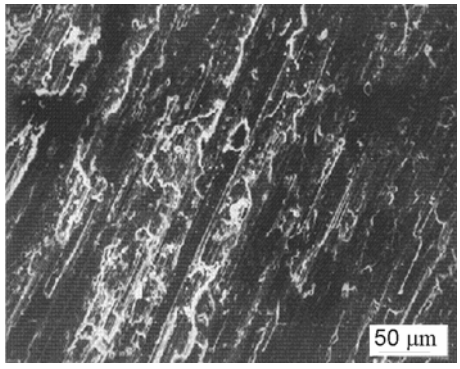

Fig. 6. The wear surface of the Al 2219/5% SiCp composite at a speed of 3 m/s and load of 20 N, after running for a distance of 5000 m

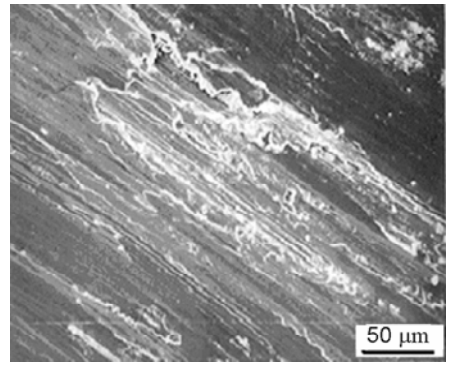

Fig. 7. SEM images of Athe l 2219/10% SiCp composite at a speed 3 m/s and a load of 40 N, after running for a distance of 5000 m

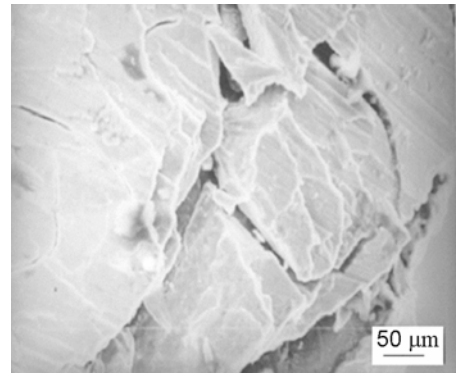

Fig. 8. SEM images of the worn surface of the composite containing 15% SiCp reinforcement after sliding 5000 m under the 40 N load and at a sliding speed of 3 m/s

surfaces of aluminium alloy 2219, for a load of 20 N, speed of 3 m/s, and distance of 5000 m. Figures. 7 and 8 show the wear track morphology of the specimens tested at a load of 40 N, sliding speed of 3 m/s, and a sliding distance of 5000 m, for 10% and 15% of SiCp reinforcement, respectively. The micrograph shows the interaction of SiCp particles with the surface of hard disc, such that the initial formation of the lubricant layer can be observed and the SiCp particles are projecting outside. The cracking of particles is also seen to initiate at a particular location. A large deformation and cracking of the surface can be observed in the specimen containing 15% reinforced composite, in which voids and particle clustering occurred. The same explanation holds even for the other composites, however, and with other sliding distances and loads. A large amount of plastic deformation was observed on the surface of the unreinforced alloy. In the case of composites containing 5% SiCp, 10% SiCp, and 15% SiCp, the worn out surfaces are not smooth. Grooves were formed by the reinforcing particles. On these surfaces, areas showing a fractured appearance can be observed.

It can be seen that a layer of material was removed as debris from the surface and that this debris is in the form of thin sheets. It has been reported that tearing (fracture) has influence on the formation of wear debris [18]. The specimen (Fig. 7) shows continuous wear grooves and cracking of flakes along the wear track. In some places, the diversion of wear grooves is also observed. When delamination wear occurs, the subsurface cracks, which may exist previously or become nucleated due to stress, propagate during the course of wear. When such subsurface cracks join with the wear surface, delamination becomes the dominant wear mechanism [19].

4. Discussion

The graphs from the wear tests show that the wear rate of the metal matrix reinforced with SiC particles reduces with increasing reinforcement content for dry sliding wear tests, and this has been confirmed by other researchers [20, 21]. The examination of the worn surfaces shows areas from where material has been removed. As the load increases, the morphology of the worn surfaces gradually changes from fine scratches to distinct grooves, and damaged spots in the form of craters can be seen [22]. The asperities of both the pin and counterface are in contact with each other and are subject to relative motion under the influence of applied load. Initially, both the surfaces are associated with a large number of sharp asperities, and contact between the two surfaces takes place primarily at these points. In the present case, the asperities of the pin also have a large number of reinforcements in the form of asperities. Under the influence of applied load and speed, when the asperities on each surface come in contact, they are either plastically deformed or remain in elastic contact. As the asperities have very sharp shapes, the effective stress on these sharp points may be more than the elastic stress, and then all these sharp asperities are plastically deformed at their contact points except for the partially projected points of the SiCp reinforcement. The other plastically deformed surface may fill the valley of the mate-

rial both on pin and counterface during the course of action. Thus, there is a possibility of fracturing a few asperities on both surfaces, leading to very fine debris particles. At lower loads, the projected SiC particles in the composites will be in contact with the counterface during the course of wear. The asperities of the sliding pin surface come into contact with the steel disc surface, and are work hardened under the applied load and speed due to cold working on the surface of the pin [23]. The SiC particles are very strong in compression than in tension. Therefore, instead of the surfaces of particles cracking, they will be pushed back into the soft Al 2219 alloy. The initial run in period in all cases, the wear rate is more due to the fact that a few highly projected broken SiC particles on the pin will act as debris and plough the surface, particularly in the Al 2219-SiCp composite specimen, leaving projecting SiC in the composite.

The stress on the surface of the Al 2219 alloy is almost uniform and contact between the pin and counterface results in a larger contact area and hence larger stress and wear. The wear rate is largest in the initial period, and as the speed increases for a constant load of 40 N, the wear rate slowly decreases in the case of composites and stays almost constant in the case of unreinforced Al 2219. At speeds above 3 m/s, the wear rate starts to increase in unreinforced specimens. It is evident from the study that a combination of abrasive and delamination wear is in operation. At speeds above 6.1 m/s, only severe delamination wear is in operation, leading to the seizure of the material [24].

In SiCp reinforced composites, the wear rate approaches a minimum as the speed increases up to 4.6 m/s, beyond which abrasive wear begins to operate, and the wear pattern changes to severe at speeds above 6.1 m/s. The wear rate at the beginning is larger, because the asperities of SiC particles are not projected and the entire surface is under the same amount of stress, so that the asperities deform easily and the fractured particles and un fractured SiC particles plough the surface of the counterface and pin. When the speed increases, the ploughed surface of the counterface (i.e. steel) reacts and forms Fe_3O_4, which causes SiC particles to crush and form very minute particles [14, 25]. Fe_3O_4, Fe, and minute particles of SiC form a layer between the work hardened pin and the counterface and reduce the wear rate up to a speed of 4.6 m/s. When the speed increases to 6.1 m/s, the surface film breaks for the same combination of speed and sliding distance, and the sub surface, which had work hardened, will be under severe stress. The microscopic projections or asperities at the sliding surface form a combination of abrasive and adhesive wear [26]. The sliding forces fractures bonds, tearing metal from the pin surface and minute projections of the Al 2219 on the counterface. This further leads to the seizure of the wear surface. Thus, due to plastic deformation and fracturing, the surface becomes smoother with increasing in sliding distance.

5. Conclusions

SiC particles can be used as reinforcement material to improve the properties of the Al 2219 alloy. The microstructure of the SiCp-reinforced composite showed

a reasonably uniform distribution of particles and good interfacial bonding of dispersed particles with the matrix alloy. The DRMMCs reinforced with SiCp exhibit better dry sliding wear resistance than the unreinforced Al 2219 alloy. In the present investigation, the 15% SiCp-reinforced composite exhibited better wear resistance than the other combinations of Al 2219 and SiCp. Wear rate decreases as the sliding speed increases up to 4.6 m/s for a load of 40 N, after which the wear rate also increases as the speed increases. This may be due to the work hardening of the surface, the formation of iron oxide, and crushing of the SiC particles.

The wear rate of both reinforced and unreinforced specimens increases as the load increases. The unreinforced alloy specimen seized much earlier than the composites. A combination of adhesion and delamination wear was in operation.

References

[1] IBRAHIM I.A., MOHAMED F.A., LAVERNIA E.J., J. Mater. Sci., 26 (1991), 1137.
[2] SINCLAIR I., GREGSON P.J., Mater. Sci. Technol., 3 (1997), 709.
[3] Ma T., YAMAURA T.H., KOSS D.A., VOIGT R.C., Mater. Sci. Eng. A., 360 (2003), 116.
[4] PARK B.G., CROSKY A.G., HELLIER A.K., J. Mater. Sci., 36 (2001), 2417.
[5] SRIVATSAN T.S., J. Mater. Sci., 31 (1996), 1375.
[6] SEAH K.H.W., SHARMA S.C., GIRISH B.M., Composites A., 29 (1997), 251.
[7] JHA A.K., DAN T.K., PRASAD S.V., ROHATGI P.K., J. Mater. Sci , 21 (1986), 3681.
[8] SANNINO A.P., RACK H.J., Wear, 189 (1995), 1.
[9] DEUIS R.L., SUBRAMANIAN C., YELLUP J.M., Wear, 201 (1996), 132.
[10] NARAYAN M., SURAPPA M.K., PRAMILA BAI B.N., Wear, 181–183 (1995), 563.
[11] SHIPWAY P.H., KENNEDY A.R., WILKES A.J., Wear, 216 (1998), 160.
[12] KORKUT M.H., Mater. Sci. Technol., 20 (2004), 73.
[13] VENKATARAMAN B., SUNDARARAJAN G., Wear, 245 (2000), 22.
[14] LIM S.C., GUPTA M., REN L.J., KWOK K.M., J. Mater. Proc. Technol., 89–90 (1999), 591.
[15] HASHIM J., LOONEY L., HASHMI M.S.J., Mater. Proc. Technol., 123 (2002), 251.
[16] ZHOU W., XU Z.M., J. Mater. Proc. Technol., 63 (1997), 358.
[17] SEAH K.H.W., SHARMA S.C., GIRESH B.M., LIM S.C., Mater. Design, 17 (1996), 63.
[18] KIOURTSIDIS G.E., SKOLIANOS S.M., Wear, 253 (2002), 946.
[19] DAS S., PRASAD S.V., RAMACHANDRAN T.R., Wear, 133 (1998), 173.
[20] MURATOGLU M., AKSOY M., Mater. Sci. Eng. A, 282 (2000), 91.
[21] PRASAD B.K., Wear, 252 (2002), 250.
[22] BASAVARAJAPPA S., CHANDRAMOHAN G., International conference on recent advances in composite materials, Bhanaras Hindu University, Bhanaras, India, 2004, 625.
[23] MOHAN S., PATHAK J.P., GUPTA R.C., SRIVASTAVA S., Metallkunde, 93 (2002), 1245.
[24] GUO M.L.T., TSAO C.-Y.A., Mater. Sci. Eng. A, 333 (2002), 134.
[25] FERHAT G., MEHMET A., Comp. Sci. Technol., 64 (2004) 959.
[26] RIAHI A.R., ALPAS A.T., Wear, 251 (2001), 1396.

Received 27 June 2005
Revised 21 November 2005

Materials Science-Poland, Vol. 24, No. 2/1, 2006

Aquo-organic sol-based F-doped SnO_2 (Sn:F = 90:10) coatings on glass

P. K. BISWAS*, L. DUA, A. DE, T. CHAUDHURI

Sol-Gel Division, Central Glass and Ceramic Research Institute, Kolkata 700 032, India

An aqueous precursor of F-doped SnO_2 was prepared starting with hydrated Sn (IV) chloride, ammonium fluoride and water. Polyvinyl alcohol (mol. wt. 22 000), a sol stabilizer, was used for better adherence to the glass substrate. Both the dipping and the spinning techniques were used to deposit layers of different thickness (from 200 to 650 ± 10 nm). Air drying and subsequent curing at ca. 450 °C in air yielded a tetragonal cassiterite phase of SnO_2 and a tetragonal Sn phase. The percentage of visible transmission of the spin-coated samples was relatively high (ca. 80 %). Incorporation of polyvinyl alcohol into the aqueous precursor minimized etching by fluoride ions, as revealed by SEM pictures. The surfaces of the developed films seemed to be porous, and the spin-coated sample was relatively less porous. The refractive index (RI) of the dip-coated samples was in the range 1.650–1.803, while the spin-coated samples had RI values in the range 1.670–1.823. The sheet resistance of the spin-coated films was in the range 3.3–1300 kΩ /□, and 1.4 – 2500 kΩ /□ in the case of dip coated samples.

Key words: *fluorine-doped tin oxide; sol-gel; SEM; polyvinyl alcohol*

1. Introduction

Thin films of SnO_2, In_2O_3 and their doped forms possess high transparency in visible and high electrical conductivity [1–4]. Fluorine-doped tin oxide films also yield high conductivity [4, 5]. These films can be produced by various deposition methods [6, 7]. Chemical vapour deposition (CVD) [7] has been exploited in the commercial production of F-doped SnO_2. The latest developments in sol-gel science and technology yield a simple method of film deposition [8, 9]. Indium tin oxide (ITO) and Sb-doped SnO_2 coatings on glass produced by sol-gel processing [10–13] have been intensively investigated, but the results concerning sol-gel F-doped tin oxide coatings on glass are scanty. As precursors for F-doped SnO_2 (FTO) coatings contain fluoride ions, there is a large probability of surface etching. Our previous work [14] discussed

*Corresponding author, e-mail: pkb@cgcri.res.in

severely corroded surface features of FTO developed from precursors having no organic binders. Polyvinyl alcohol (PVA), which acts as an organic binder, is partially resistant to fluoride ions. Therefore PVA may be used to overcome the corrosion problem. This work is an attempt to learn about FTO coatings prepared from precursors containing fluoride ions and an organic binder.

2. Experimental

Preparation of precursor sol. SiO_2 precursor sol of 7 wt. % equivalent silica in a mixture of 1-propanol and 2-butanol was prepared from tetraethylorthosilicate (TEOS). The details of preparation are given elsewhere [15].

The starting materials of the FTO precursor sols were $SnCl_4 \cdot 5H_2O$ (Loba Chemie, 98%), and aqueous HF solution (E. Merck India Ltd, 40%, GR). $SnCl_4 \cdot 5H_2O$ was initially dissolved in ethanol. The required amount of HF solution (Sn:F = 90.0:10.0) was then added to the above salt solution. Next, 2 wt. % aqueous solution of polyvinyl alcohol (PVA) (BDH, mol. wt. ca. 22 000) was added in such a way that the resulting solution contained 8.0–10.0 wt. % equivalent SnO_2. The mixed solution was stirred and finally aged to obtain the precursor sol.

Film deposition. Soda lime silica glass substrates (25 mm in diameter and 2–3 mm thick for spinning; 75 mm long, 22 mm wide, and 1–2 mm thick for dipping) were first treated with 1–2% Extran pure (E. Merck India Ltd.) solution in deionised water for 10–15 min and subsequently ultrasonicated in the same medium for 30 min. The substrates were then washed thoroughly with distilled water, followed by treatment with GR grade acetone (E. Merck India Ltd.). Finally, they were dried in an air oven at 100 ^{o}C for 10 min. The substrates were then preserved in a dry desiccator after cooling them to ambient temperature.

The barrier layer, ca. 0.2 μm thick, was deposited on soda lime silica glass (SLS) substrates by dipping (withdrawal speed 15–17 cm/min), utilizing the precursor (7 wt. % equivalent SiO_2). The gel film initially formed was cured at ca. 450 °C for 30 min in air. The FTO coatings were deposited on the above substrates already coated with a barrier layer by following the same dipping and the spinning methods and conditions used for the SiO_2 film. The lifting speed for the dipping and the RPM for the spinning were optimised to 5 cm/min and 3000, respectively. After each operation, curing was done at the same temperature under similar conditions. The dip coated samples were designated as Fd-1–Fd-6 (Table 1), according to the number of operations. Similarly, the spin-coated samples were designated as Fs-1–Fs-5.

The electrical conductivity of the films was tested by measuring sheet resistance using a two-probe system (Philips multimeter, model PM 2525). The thickness and refractive index of the films were measured at 632.8 nm with an Rudolph Auto EL II ellipsometer. An optically determined physical thickness of a higher order was considered and verified in some cases by measuring thickness with the Stylus method (Sloan Dektak FLM, USA), which measures the step-height of a film mechanically.

The vertical resolution of the equipment was ±2.5 nm. The spectral reflection and transmission of the samples in the UV–visible region were recorded using a Shimadzu UV-VIS-NIR spectrophotometer, model UV 3101 PC. Phase identification for the films was made with a Philips Expert pro X-ray diffractometer with CuK_α radiation. The microstructure of the films was studied utilizing a LEO S 430 I scanning electron microscope.

3. Results and discussion

In our earlier work [14], we have observed that F-doped SnO_2 (FTO) films prepared from the precursors Sn:F ranging from 97:3 to 99:1 were typically etched out by fluoride ions, resulting in relatively high sheet resistance even for large thickness (eg., 550 nm). In this case, we did not use any organic binder. To overcome the above difficulty, we deposited FTO from a precursor based on an organic binder. Polyvinyl alcohol (PVA) was used as the organic binder, as it may deactivate fluoride ion etching. In addition, the added HF has a tendency to evaporate during curing.

Table 1. Sample designation, refractive index, physical thickness and sheet resistance of the F-doped SnO_2 films

Sample designation	Physical thickness (nm)		Refractive index[1] (±0.003)[2] (at 632.8 nm)	Sheet resistance kΩ/□
	Ellipsometric method (±0.5)	Stylus method (±5)		
Fd-1	195.5–216.0	240	1.650–1.707	2500
Fd-2	230.5–254.0		1.663–1.726	40.0
Fd-3	412.0–449.5		1.672–1.733	20.0
Fd-4	454.0–479.5		1.660–1.752	3.4
Fd-5	575.0–610.0		1.657–1.803	2.7
Fd-6	631.0–652.5	580	1.680–1.781	1.4
Fs-1	74.5–85.5	105	1.670–1.789	1300
Fs-2	190.5–201.5		1.675–1.799	62.0
Fs-3	223.5–259.5		1.687–1.807	10.9
Fs-4	234.0–260.0		1.701–1.820	9.0
Fs-5	441.0–452.0	370	1.710–1.823	3.3

[1]The apparent inconsistency of the refractive index is due to the inhomogeneous density of the films. For each film, the R. I. range was obtained from measurements at different points (about 10) of the films deposited on glasses with dimensions of 25 mm x 25 mm for rectangular shape and 25 mm in diameter for circular shape.

[2]The instrumental accuracy of the R. I. measured at a single point.

Hence, in the presence of the binder we made an attempt to incorporate a relatively high content of fluoride ions (Sn:F = 90:10). In the case of dipping, severe inhomogeneity with staining below 1.0 mm was observed at the bottom edge of the substrate – excess sol, adhered to the gel layer during the withdrawal of the substrate from the sol bath, drifted down due to gravitation and rested in lower part of the sub-

strate. On the other hand, in the case of spinning, staining below 0.5 mm was generated at the periphery of the substrate, because excess sol was allowed to stay at the periphery after spinning off due to centrifugal force.

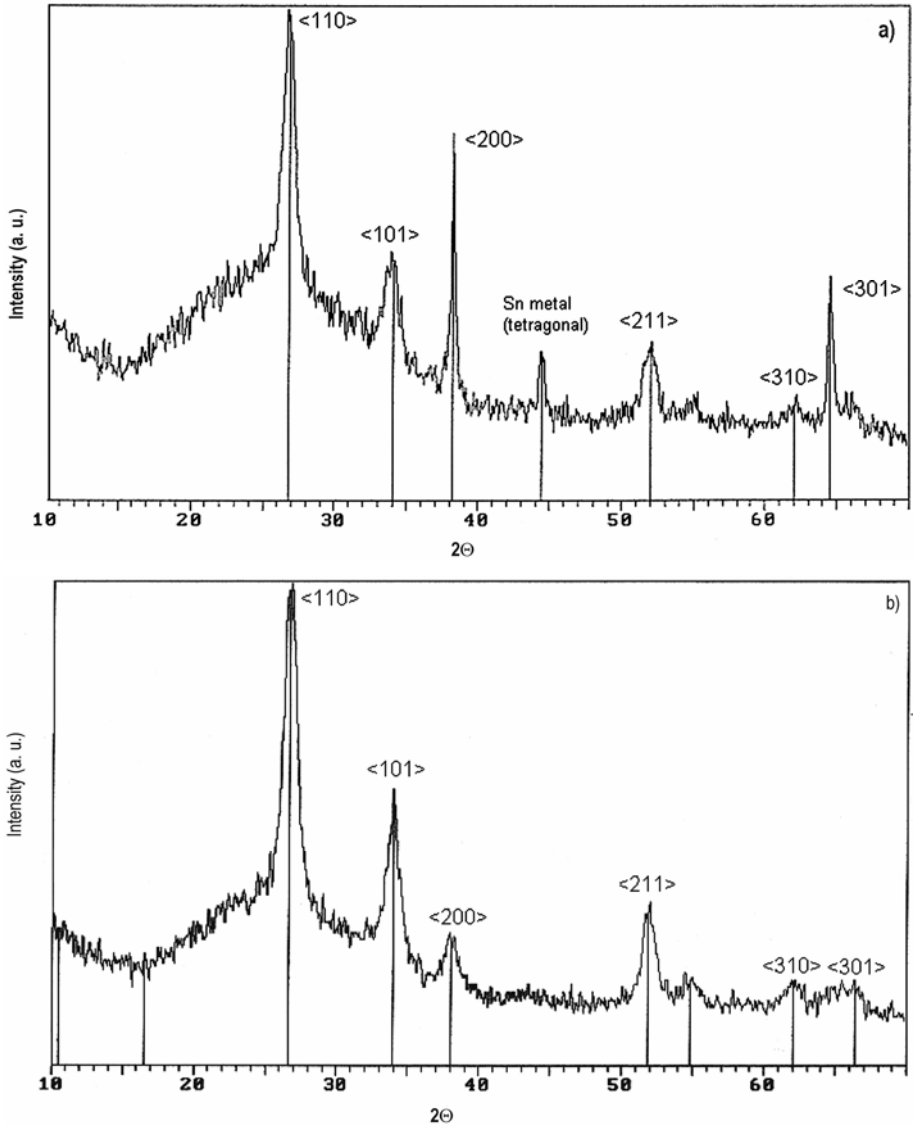

Fig. 1. XRD pattern of spin-coated Fs-5 (a) and dip coated, Fd-6 (b) F-doped SnO_2 samples

In Table 1, the sheet resistances of developed films with various thicknesses are given. The sheet resistance decreased considerably with increasing thickness. We were successful in depositing layer with the thickness above 600 nm by six-fold dipping, while we could not proceed beyond ca. 440 nm (five dipping operations) in the

case of spinning. Any attempt for additional operation beyond the above would result in the peeling of coated layers. Multiple coating operations were carried out in order to increase the physical thickness of the films. Surprisingly, multiple coating operations do not increase the physical thickness of films in a cumulative manner, especially after the 2nd and 4th operations for dip coated films and after 3rd and 4th operations for spin-coated films (Table 1). In the case of dipping, thickness seemed to increase effectively after each alternate coating operation. Since each coating operation was followed by a curing treatment, it can be concluded that curing a particular layer two times is more suitable for the effective addition of a subsequent layer. Spin-coated samples, however, do not show such regularity regarding the increment of physical thickness, but the effectiveness of multiple curing treatments instead of multiple layer depositions cannot be ruled out.

Films with relatively low thickness (> 240 nm) prepared under two different techniques did not show any characteristic peaks in their X-ray diffractograms (not shown here), since the diffractometer could not record very weak reflections of the film material. Figure 1 shows X-ray diffractograms of FTO films (Fd-6 and Fs-5, Table 1) of relatively high thickness (in the range 440–600 nm). The tetragonal cassiterite phase was more prominent in this case. It is interesting to note that the tetragonal phase of Sn-metal was mixed with the cassiterite phase of SnO_2 for coating with the spinning method. This metallic phase was not observed for the dip coated FTO. The formation of the Sn metal depends on the deposition technique.

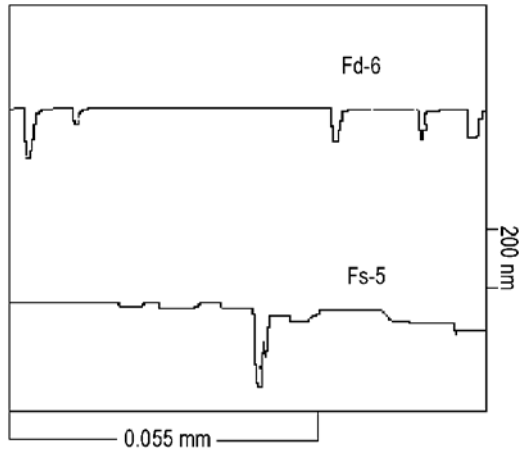

Fig. 2. Surface profiles of samples deposited with different sol-gel deposition methods: dipping, Fd-6 and spinning, Fs-5

It has been reported [1] that tin dioxide coatings behave as transparent films with little surface roughness. We have observed [14] etching of film surfaces due to doping with F^-, resulting in surface roughness. In the present report, we conclude that surface roughness decreases after adding an organic binder to the precursor, as evident from the surface profiles (Fig. 2) of the coated samples. The spin-coated surface is smoother than the dip coated surface, because there are fewer pores in the case of spin-coated system. There is a lowering trend for thickness at the edge of the substrate

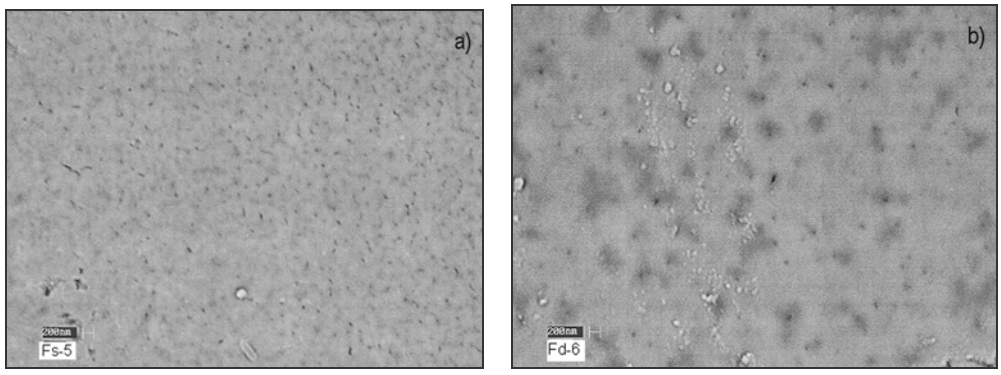

Fig. 3. SEM pictures of spin-coated Fs-5 (a) and dip coated Fd-6 (b) samples

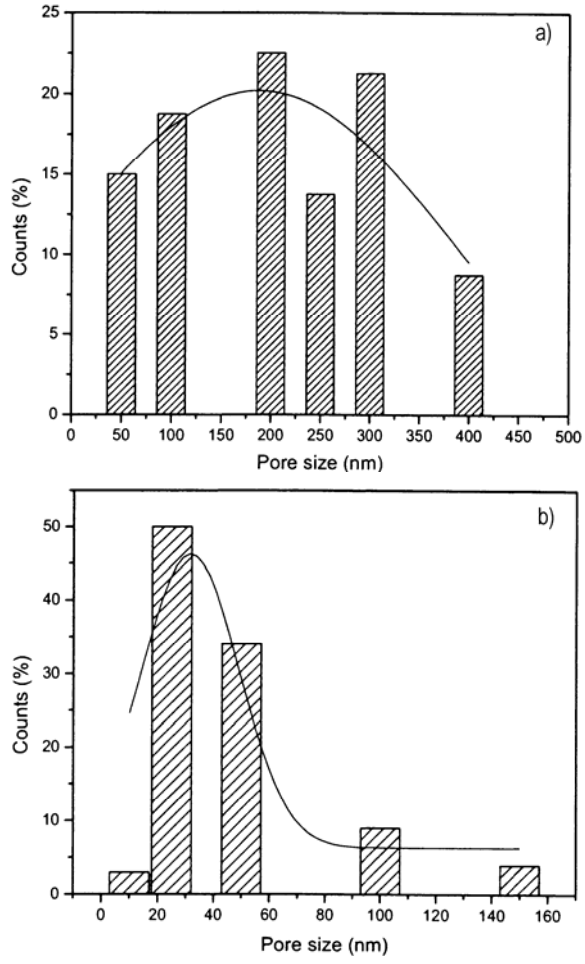

Fig. 4. Pore size distributions of the dip coated Fd-6 (a) and spin-coated Fs-5 (b) samples

due to spinning. As a result, the stylus moves downwards in the radial direction. The surface features revealed by SEM (Fig. 3) also confirm the surface smoothness of the spin-coated sample – the average pore size distributions (Fig. 4) of the spin-coated films were smaller (32 nm) than those of dip coated films (190 nm). Physical thicknesses of the films were measured ellipsometrically, and verified in a few cases by the stylus method. They did not increase linearly with the number of coating operations. The successive deposition of an FTO based on an organic binder would possibly require surface treatment, which would increase the adherence of the layers. This feature requires detailed work, which is under progress.

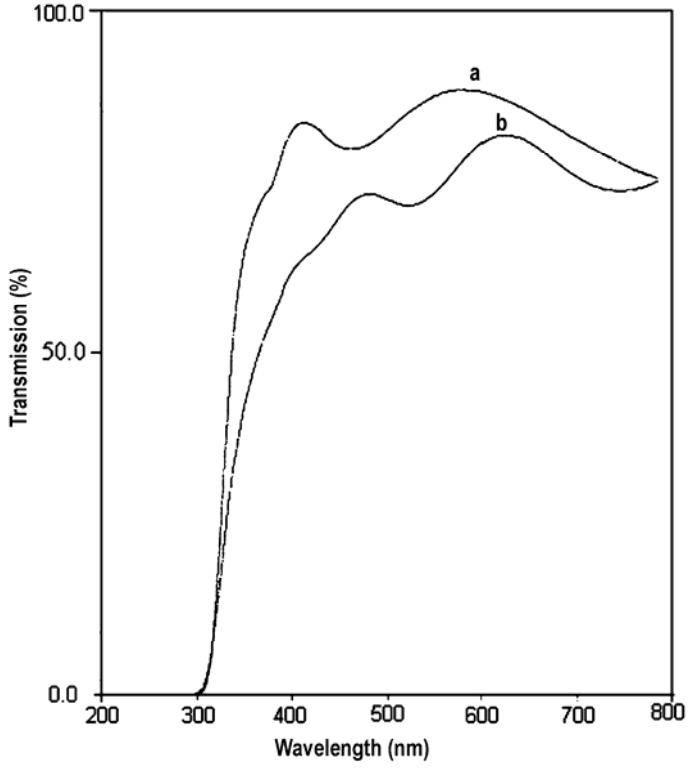

Fig. 5. Transmission spectra of spin-coated Fs-5 (a) and dip coated Fs-6 samples (b)

The refractive index of the films increased with increasing thickness from 1.650 to 1.823. The transmission of the dip/spin-coated samples decreased with increasing physical thickness (not shown here). Typical examples of the transmission spectra of dip and spin-coated samples with maximum physical thickness are shown in Fig 5. The lowering of transmission for the dip coated sample may be caused by scattering by the pores observed in the surface profiles (Fig. 2) and SEM images (Fig. 3). When the sheet resistance for films with almost the same thickness and prepared by the two techniques is compared, it can be seen that the dip coated films exhibit relatively high

sheet resistance (20 kΩ/□ for the thickness of 412–450 nm) with respect to the spin-coated films (3.3 kΩ/□ for the thickness of 441–452 nm). This may be due to the presence of porous microstructures.

4. Conclusions

Fluorine-doped tin oxide thin films with high contents of fluorine (Sn:F = 90:10) were prepared by simple sol-gel dipping and spinning techniques. The surface roughness due to etching by fluoride ions was minimized by adding an organic binder, polyvinyl alcohol (PVA), to the precursor. This approach helped to develop crystallized FTO in a simpler way. Consequently, the electrical conductivity increased. The surface profiles as determined by SEM and the stylus method also reveal rather smooth surfaces. The spin coating technique yielded coatings of better performance.

Acknowledgments

Thanks are due to ZAE Bayern, Bavarian Centre for Applied Energy Research, Würzburg, Germany for sponsoring the Indo-German collaborative project, under which this work was performed. Authors are thankful to the Directors of CGCRI, Kolkata, India and ZAE Bayern, Germany for their constant encouragement and permission to present this paper at the 5th ICCG, 2004.

References

[1] HAITJEMA H., WOERLEE G.F., Thin Solid Films, 169 (1989), 1.
[2] UPADHYAY J.P., VISHWAKARMA S.R., PRASAD H.C., Thin Solid Films, 169 (1989), 195.
[3] CHOPRA K.L., MAJOR S., PANDYA D.K., Thin Solid Films, 102 (1981), 1.
[4] SHANTHI E., DUTTA V., BANERJEE A., CHOPRA K.L., J. Appl. Phys., 51 (1980), 6243.
[5] DAWAR A.L., JOSHI J.C., J. Mat. Sci., 19 (1984), 1.
[6] HAITJEMA H., ELICH J., Solar Energy Mat., 16 (1987), 79.
[7] POPOVA L.I., MICHAILOV M.G., GUEORGUIEV V.K., SHOPOV A., Thin Solid Films, 186 (1990), 107.
[8] CHATELON J.P., TERRIER C., ROGER J.A., BERJOAN R., J. Sol-Gel Sci. Tech., 10 (1997), 55.
[9] CHATELON J.P., TERRIER C., BERNSTEIN E., BERJOAN R., ROGER J.A., Thin Solid Films, 247 (1994), 162.
[10] LIU J., RADLEIN E., FRISCHAT G.H., Phys. Chem. Glasses, 40 (1999), 277.
[11] ROY-RAMANAN S.R., Thin Solid Films, 389 (2001), 207.
[12] OREL B., LAVRENČIČ-ŠTANKGAR U., CRNJAK-OREL Z., BUKOVEC P., KOSEC M., J. Non-Cryst. Solid., 167 (1994), 272.
[13] GONZALEZ-OLIVER C.J.R., KATO I., J. Non-Cryst. Solid., 82 (1986), 400.
[14] CHAUDHURI T., DE P. K., BISWAS A., Trans. Indian Ceram. Soc., 62 (2003), 208.
[15] BISWAS P.K., KUNDU D., GANGULI D., J. Mater. Sci. Lett., 8 (1989), 1436.

Received 27 July 2005
Revised 2 December 2005

Materials Science-Poland, Vol. 24, No. 2/1, 2006

Characterization of sol-gel derived yttrium-doped n-ZnO/p-Si heterostructure

N. KUMAR[1], R. KAUR[2], R. M. MEHRA[3*]

[1]Department of Electronics, Sri Venkateswara College, University of Delhi, New Delhi 110021, India

[2]Department of Physics and Electronics, Deen Dayal Upadhayay College, University of Delhi, New Delhi 110015, India

[3]Department of Electronic Science, University of Delhi South Campus, New Delhi 110021, India

The paper reports the experimental and theoretical analysis of current–voltage characteristics of n-ZnO/p-Si (100) heterostructures. Yttrium-doped ZnO films were deposited on p-Si by the sol-gel process using the spin coating technique. Their structural and electrical properties were studied as a function of annealing temperature. The experimental data were analysed by modifying the current voltage relation predicted by Perlman and Feucht. An estimate of the defect density at the ZnO/Si interface was made using Mott–Schottky (C^{-2}–U) plots.

Key words: *sol-gel; yttrium-doped ZnO; heterostructure; I–U characteristics; C–U characteristics*

1. Introduction

It is well recognized that a reliable and mass-produceable blue-ultraviolet semiconductor diode laser will have a major importance in information storage, display, photochemistry, and other areas of technology. GaN-based lasers and LEDs are already achieving commercial realization and undergoing improvements in lifetime and synthesis techniques. ZnO has been used for decades in powder form for phosphors and in polycrystalline form for varistors. ZnO has a direct band gap of 3.3 eV at room temperature, comparable to that of GaN. It is refractory, with a melting point of 1975 °C compared to 1100 °C for ZnSe, leading us to expect that it will be more robust with regard to defect generation under electronic and thermal stress. In contrast to GaN, large single crystals of ZnO can easily be grown. The exciton binding energy in ZnO is 60 meV, three times larger than that of ZnSe or GaN, and more than twice as

* Corresponding author, e-mail: rammehra2003@yahoo.com

large as *kT* at room temperature (RT) [1]. This means that the recombination and luminescence properties of ZnO should retain exciton characteristics at and above RT, including the substantial enhancement of oscillator strength. ZnO thin films can be prepared by a wide variety of techniques, including sputtering [2], reactive evaporation [3], chemical vapour deposition [4], spray pyrolysis [5], and the sol-gel [6] process. In particular, the sol-gel method has advantages over the other processes, because of its simplicity and low equipment cost. With regards to the transparent and conducting window layer for optoelectronic devices, ZnO has an additional advantage over ITO – it is able to tolerate reducing chemical environments. For instance, ZnO films are more stable than ITO-based films in the presence of hydrogen plasma. They can match, if not exceed, optical and electrical properties of ITO. Furthermore, the components of ITO, namely In and Sn, are limited in supply and are more expensive than zinc.

A renewed interest in the luminescence and electrical properties of ZnO/Si heterostructures has also emerged. There have been reports on undoped n-ZnO/p-Si heterostructures fabricated by magnetron sputtering, chemical vapour deposition and spray pyrolysis. Jeong et al. [7] and Lee et al. [8] have reported the fabrication of an undoped n-ZnO/p-Si photodiode by sputter deposition. They have also reported that the fabricated photodiode exhibits good photoelectric performance when ZnO is deposited at 480 °C. It has also been concluded that the photodiode exhibits an induced photocurrent proportional to the reverse bias for UV illumination and saturation at moderate bias for visible illumination. Park et al. [9] have reported that there is an effective reduction in the dark leakage current after implanting Si^+ ions into the device structure of insulating ZnO and semiconducting n-ZnO overlayers on p-Si. Thin film ZnO/InP and ZnO/Si heterojunctions obtained by thermal decomposition of Zn acetylacetonate have been investigated by Purica et al. [10] for optoelectronic device applications. Baik et al. [11] have studied Al-doped ZnO/n-Si junction solar cells prepared by spin coating.

In the present work, n-type ZnO films, pure and yttrium-doped, have been grown on p-silicon substrates by spin coating, using zinc acetate and ethanol as the precursors and DEA as the stabilizer. The effects of yttrium doping on the structural, electrical and optical properties of the films are reported.

The *I–U* characteristics of n-ZnO/p-Si heterostructures have been studied as a function of annealing temperature, and analysed by taking into account the diffusion and generation recombination current [12]. An estimate of the defect density at the ZnO-Si interface has been made using capacitance-voltage(*C–U*) measurements [13].

2. Experimental

The precursor solution of ZnO (0.2 M) was prepared from zinc acetate ($Zn(CH_3CO_2)_2{\cdot}2H_2O$, purity 99.5%) dissolved in anhydrous ethanol. Yttrium nitrate hexahydrate ($Y_2NO_3{\cdot}6H_2O$) was used as the dopant (3 wt. %). The mixture so ob-

tained was stirred with a magnetic stirrer for about 4 h at room temperature, after which it remained milky. An equimolar amount of diethanolamine (DEA) was added to the solution drop by drop which eliminated the obtained turbidity and precipitates completely. The resultant solution was very clear, transparent, and homogenous. The solution was left to age for 48 h to obtain optimum viscosity before film deposition. The corning glass (7059) substrates, after being cleaned with acetone and methanol in an ultrasonic bath for 20 minutes, were rinsed with deionised water for 5 min and dried in a nitrogen atmosphere. The Si (2–4 Ω×cm resistivity) samples were cleaned in trichloroethylene, acetone and isopropyl acetate consecutively for 10 min in an ultrasonic bath. The substrates were rinsed in overflowing deionised water for 10 min and treated with a 2% HF solution in order to remove the native oxide, then washed with deionised water for 20 minutes, and dried with dry nitrogen gas. The deposition of yttrium-doped zinc oxide (YZO) film was carried at room temperature with a spinning speed of 2700 rpm for 20 sec. The films were left in air for 10 min to hydrolyse (by esterification) and then dried in air at 250 °C in order to gel. The process was repeated 12 to15 times to obtain the film thickness of ca. 250 nm. The films were annealed in air in the temperature range 300–600 °C for an hour. The YZO films so developed exhibit n-type conductivity [14].

The structural properties of the films were investigated with an X-ray diffractometer. The thickness of the ZnO layer was measured with a Dekteck$^{3\text{-}ST}$surface profilometer. The *I–U* characteristics of these heterostructures were recorded using a Keithley Source Meter (2400) and *C–U* measurements were carried on a Biorad *C–U* meter (DL 4600) using a voltage source (4140 V) and a Boonton capacitance meter. Optical transmittance measurements were carried out in the wavelength range 200–800 nm using a double beam spectrophotometer (Shimadzu 330).

3. Result and discussion

3.1. Structural properties

The X-ray diffraction patterns of pure and doped films annealed in air at various temperatures are shown in Figure 1. As-grown n-YZO films exhibited an amorphous nature, whereas annealing at 350 °C caused the conversion from the amorphous to the polycrystalline structure with (100), (002), and (101) peaks. It was observed that with an increase in annealing temperature from 350 to 450 °C, the (002) reflection peak became more intense and sharper as compared to the other peaks, indicating a preferential *c*-axis orientation.

Figure 2 shows the variation of the full-width half-maximum (FWHM) of the (002) peak with annealing temperature. The decrease of FWHM with increasing annealing temperature indicates an improvement in the crystallinity of the ZnO layer. No further improvement in crystallinity was observed at annealing temperatures above 450 °C (up to 600 °C).

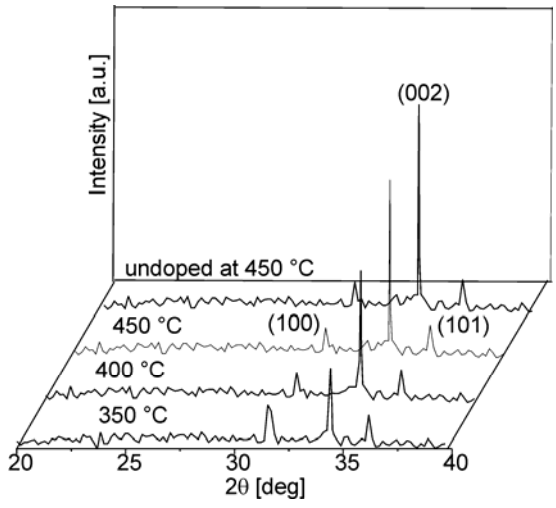

Fig. 1. XRD patterns of a YZO film on a Si substrate annealed at various temperatures

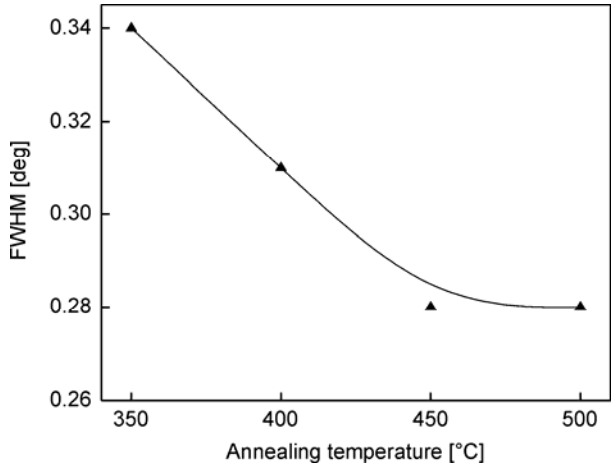

Fig. 2. Effect of annealing temperature on the FWHM of the (002) peak of a YZO film on a Si substrate

3.2. Optical transmittance

The transparency and homogeneity of pure and yttrium-doped ZnO thin films can be tested by optical transmittance measurements in the UV, VIS, and NIR ranges. The optical transmittance of pure and doped films on corning glass is shown in Figure 3. The films exhibit high transparency (>80%) in the visible region 400–800 nm. In the UV region, the optical transmittance falls sharply, indicating the onset of absorption in this region. The threshold of optical absorption shifts toward shorter wavelengths

for yttrium-doped ZnO films, suggesting an increase in the band gap due to yttrium doping. The observed optical interferences in the transmittance curve indicate a homogenous nature of the film.

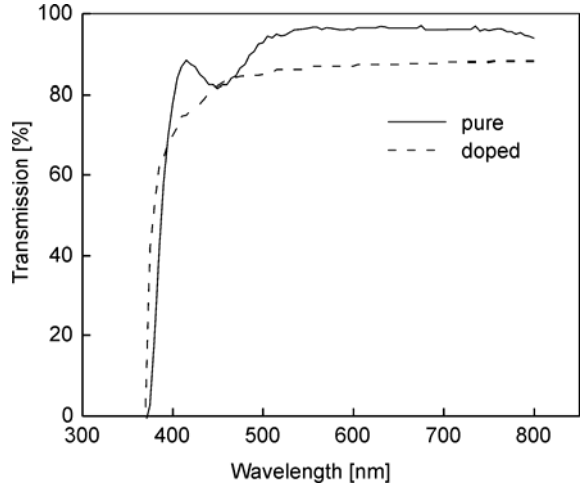

Fig. 3. Transmittance curves for pure and Y-doped ZnO films on corning glass annealed at 450 °C in air

3.3. Electrical properties

The electrical properties of the n-ZnO/p-Si heterostructures were investigated by *I–U* and *C–U* measurements. An attempt has been made to analyse the data theoretically. The *I–U* characteristics (*I* vs. *U* semi-logarithmic plots) of the heterojunction

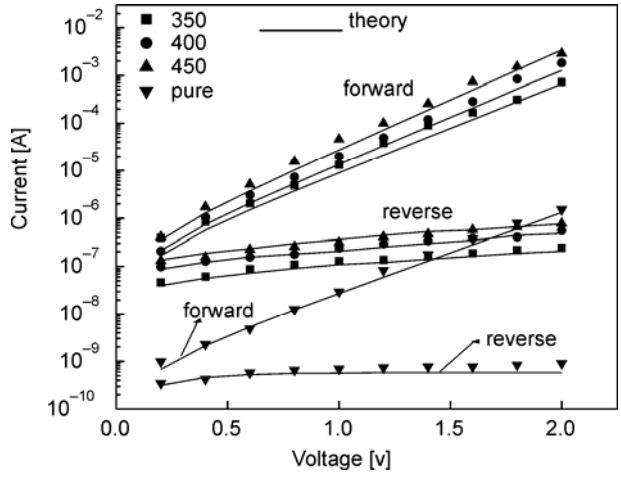

Fig. 4. Experimental and theoretical semi-logarithmic plots of *I–U* curves for the n-ZnO/p-Si heterostructure annealed at 350, 400, and 450 °C

n-ZnO/p-Si at various annealing temperatures are shown in Figure 4. A typical rectifying behaviour was observed for these heterostructures. With increasing annealing temperature, the current was found to increase both in the forward and reverse directions. The increase in the current can be caused by preferential *c*-axis growth of the n-ZnO films and/or a reduction of defect density at the interface with annealing temperature.

The energy profile of the heterojunction of the two semiconductors having different energy gaps is shown in Figure 5 in the equilibrium conditions. E_g, ε, χ, and ϕ represent the energy gaps, dielectric constants, electron affinities, and work functions of the two semiconductors, respectively. It can be seen from the figure that the discontinuity in the conduction band edges (ΔE_c) is equal to the difference in the electron affinities of the two semiconductors. The total built-in voltage (U_d) due to the difference in the work function ($\phi_1 - \phi_2$) is equal to the sum of built-in voltages on both sides.

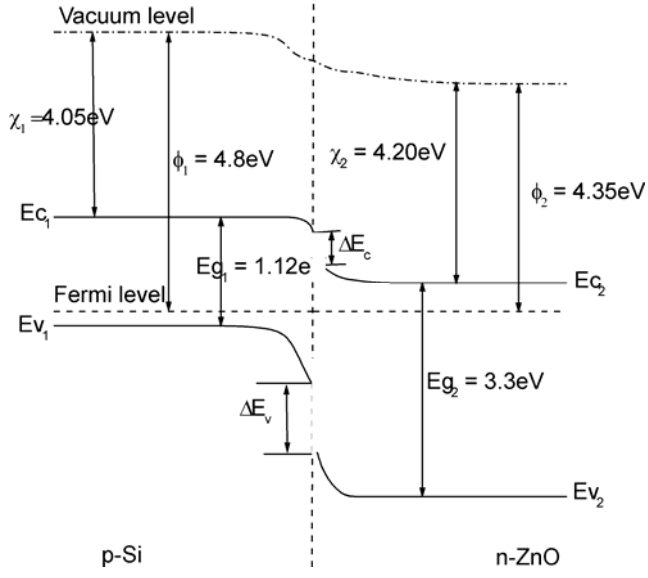

Fig. 5. Energy band profile of the n-ZnO/p-Si heterostructure

The current–voltage relation for the studied heterojunction, for which $\chi_1 < \chi_2 < \chi_1 + E_{g1}$ and $\phi_1 > \phi_2$, has been obtained by Perlman and Feucht [14] and is given below:

$$I = A\exp\left[\frac{-q(\Delta E_c + U_d)}{kT}\right] \times \left[\exp\left(\frac{qU}{kT}\right) - 1\right] \tag{1}$$

where

$$A = aqXN_d\left(\frac{D_n}{\tau_n}\right)^{1/2}, \qquad \Delta E_c = \chi_2 - \chi_1$$

U_d is the total built-in voltage, q is the electron charge, k is the Boltzman constant, T is temperature, a – the area of the diode, X – the transmission of electrons across the interface D_n if the diffusion constant, and τ_n is the lifetime of electrons in p-type materials. It may be mentioned that the experimental current values are much smaller than those predicted by this equation. The observed low values of current could be due to imperfections in the two semiconductors, resulting in defect states near the interface. Therefore, the current–voltage equation should be modified by introducing the imperfection parameter β ($\beta \geq 1$):

$$I = A\exp\left[\frac{-q\left(\Delta E_c + U_d\right)}{kT}\right] \times \left[\exp\left(\frac{qU}{\beta kT}\right) - 1\right] \tag{2}$$

Using the above equation, the *I–U* characteristics were theoretically obtained. The values used for various parameters are given in Table 1. It was found that the value of β decreases from 9 to 8 as the annealing temperature increases from 350 to 450 °C for a unit area of the diode. The decrease in β suggests an improvement in heterostructure and reduction of defect state density at the interface with annealing. The defect density of states for the heterostructure annealed at the temperature of 450 °C was estimated by the *C–U* measurements.

Table 1. Physical parameters used to fit the electrical data of the n-ZnO/p-Si heterostructure

Annealing temperature [ºC]	Donor concentration N_d [cm^{-3}]	β
450 (undoped)	2.4×10^{16}	10
350	5.1×10^{18}	9
400	5.95×10^{18}	8.5
450	9×10^{18}	8

To investigate the effect of annealing on the *I–U* characteristics, the values of N_d as obtained from Hall measurements were used in theoretical calculations. In the case of the undoped ZnO/Si heterostructure, the value of β was found to be 10, which is higher than that obtained for doped heterostructures.

The Mott–Schottky plot of a YZO/p-Si diode annealed at 450 °C and measured in the dark at room temperature is shown in Figure 6. The capacitance of the heterojunction is found to obey an approximately linear C^{-2}–U relationship in the reverse bias condition. This linear relationship implies that the depletion region in the vicinity of the heterojunction interface expands with increasing reverse bias. Since the band bending is primarily on the Si side, the C^{-2}–U intercept on the x-axis is essentially equal to the diffusion potential U_d within the Si. The slope of the line gives an estimate for defect density. At room temperature, the values of U_d and N were found to be 0.45 eV and 9.4×10^{14} cm^{-3}, respectively. The data was analysed using the Anderson model.

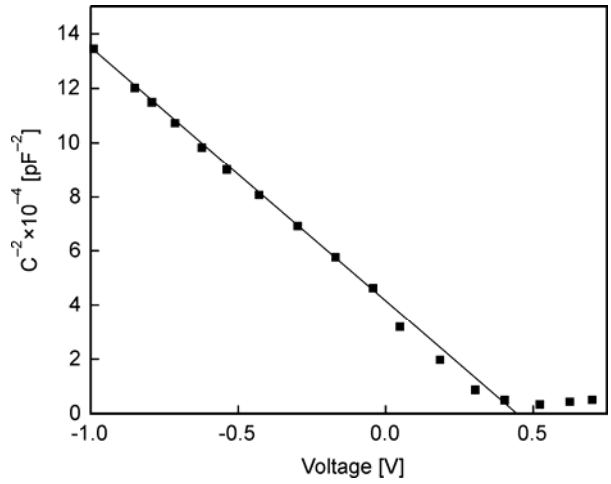

Fig. 6. C^{-2}–U curve for the n-ZnO/p-Si heterostructure at room temperature (300 K)

The C–U characteristics, as described by conventional heterojunction theory, can be expressed as

$$C^2 = \frac{q\,N\,\varepsilon_1\varepsilon_2}{2}\,\frac{1}{(U_d - U_R)} \tag{3}$$

where U_R is the applied reverse voltage. Using this equation, we can estimate the effective density of defects from the slope of C^{-2}–U_R relationships. The value of 9.4×10^{14} cm^{-3} is obtained for $\varepsilon_1 = 9$ and $\varepsilon_2 = 11.9$, the electric permittivities of ZnO and Si, respectively. The potential barrier at the junction, as determined from the C^{-2}–U characteristics as the intercept on the x-axis, was found to be 0.45 eV. Anderson model [13] predicts that this is the energy difference of the work functions between Si and ZnO. The Fermi level below the vacuum level is 4.8 eV for p-Si and 4.35 eV for n-ZnO, as shown by the energy band profile of the heterojunction. These experimental results suggest that the junction between the n-ZnO thin film and p-Si substrate is governed by conventional heterojunction theory.

4. Conclusions

Yttrium-doped n-ZnO/p-Si heterostructures have been fabricated by depositing n-ZnO films on p-Si (100) using the sol-gel process. The I–U characteristics are found to improve with improving crystallinity of the ZnO films during annealing. The calculated height of the potential barrier at the junction, using C–U measurements, is found to be equal to the difference in the work function of ZnO and silicon. The imperfec-

tion parameter β, in the present case, is found to decrease with increasing annealing temperature. The defect density at the interface, as calculated from the Mott–Schottky plot at an annealing temperature of 450 °C, was found to be nearly 10^{15} cm^{-3}.

Acknowledgements

The authors wish to acknowledge the financial support of DRDO, Govt. of India, India.

References

[1] XIONG G., WILKINSON J., TUZEMEN S., UCER K.B., WILLIAMS R.T., Proc. SPIE (2002), p. 4644.
[2] SATO H., MINAMI T., TAKATA S., Thin Solid Films, 220 (1992), 327.
[3] PETROU P., SINGH R., BRODIE D.E., Appl. Phys. Lett., 35 (1979), 930.
[4] HU J., GORDON R.G., J. Appl. Phys., 71 (1992), 880.
[5] NUNES P., MALIK A., FERNANDES B., FORTUNATO E., VILARINHO P., MARTINS R., Vacuum, 52 (1999), 45.
[6] TANG W., CAMERON.D.C., Thin Solid Films, 238 (1994), 83.
[7] JEONG I.S., HOON K.J., SAONGIL I., Appl. Phys. Lett., 83 (2003), 2946.
[8] LEE J.Y., CHOI Y.S., CHOI W.H., YEOM H.W., YOON Y.K., KIM J.H., SAONGIL I., Thin Solid Films, 420 (2002), 112.
[9] PARK C.H., JEONG I.S., KIM J.H., SAONGIL I., Appl. Phys. Lett., 82 (2003), 3973.
[10] PURICA M., BUDIANU E., RUSU E., Thin Solid Films, 383 (2001), 284.
[11] BAIK D.G, CHO S.M., Thin Solid Films, 354 (1999), 227.
[12] PERLMAN S.S., FEUCHT D.L., Solid State Electron., 7, (1964), 911.
[13] ANDERSON R.L., Solid state Electron., 5 (1962), 283.
[14] KAUR R., SINGH A.V., MEHRA. R.M., Mater. Sci.-Poland, 22 (2004), 201.

Received 23 September 2005
Revised 4 December 2005

Materials Science-Poland, Vol. 24, No. 2/1, 2006

Synthesis and hardening of fluoralinite cement

A. KANTAUTAS*, D. PALUBINSKAITĖ, G. VAICKELIONIS

Faculty of Chemical Technology, Kaunas University of Technology,
Radvilenų str. 19, 50254 Kaunas, Lithuania

The synthesis of fluoralinite cement and its hydration properties are presented. It was determined that fluoralinite is obtained after 4 hrs of burning at 1100 °C by using an initial composition of 0.89% Al_2O_3, 1.78% MgO, and 0.89% Fe_2O_3 additions. Specimens formed from fluoralinite clinker and ground sand (with a mass ratio of 1:3), hydrothermally cured at 175 °C for 4 hrs, had the highest strength (4.68 MPa). Thus, fluoralinite cement is usable for hydrothermal curing articles. X-Ray analysis showed that after hardening of the mixture of fluoralinite and quartz sand for 28 days in normal conditions, quartz, tobermorite gel, portlandite $Ca(OH)_2$, and CaF_2 prevail in the samples. This mixture hardens in hydrothermal conditions, in calcium hydrosilicate $(0.8–1.5)CaO{\cdot}SiO_2{\cdot}(0.5–2.5)H_2O$ (C–S–H (I)) and $Ca(OH)_2$ forms.

Key words: *fluoralinite; mortar; hydration*

1. Introduction

For Portland cement clinker production, 3200 to 3400 kJ/kg of energy is usually needed. It is feasible to diminish energy consumption by adding flux, i.e. additives reducing the temperature of cement formation, into the initial load. Materials containing fluorine compounds may be used as flux [1]. During burning of the mixture of Portland cement raw materials containing fluorine compounds, the following intermediate compounds may be formed: fluorspurite $(2CaO{\cdot}SiO_2)_2{\cdot}CaF_2$; fluoralinite $(3CaO{\cdot}SiO_2)_3{\cdot}CaF_2$ and fluoralumocalciumsilicate $11CaO{\cdot}7Al_2O_3{\cdot}CaF_2$ [2]. Fluorspurite is an analogue of calcium chondrodite $(2CaO{\cdot}SiO_2)_2{\cdot}Ca(OH)_2$. This compound is hydraulically inactive and stable up to 1040 °C. At higher temperatures, it decomposes into α'-$2CaO{\cdot}SiO_2$ and CaF_2 [3].

In the system of $CaO–SiO_2–CaF_2$, $(3CaO{\cdot}SiO_2)_3{\cdot}CaF_2$ is richest in calcium. Due to its similarity to chloralinite $(3CaO{\cdot}SiO_2)_3{\cdot}CaCl_2$, it has been called fluoralinite. Various difficulties arose in synthesizing pure fluoralinite. Gillioli et al. [4] applied the reagent $CaCO_3$, amorphous SiO_2, and CaF_2 for the synthesis of the pure compound. Insignificant quantities of fluoralinite are formed by heating the initial mixture at

*Corresponding author, e-mail: aras.kantautas@ktu.lt

1200 °C for 24 days. By using an initial mixture of alite $3CaO{\cdot}SiO_2$ and CaF_2, anhydrous $(3CaO{\cdot}SiO_2)_3{\cdot}CaF_2$ was obtained after 2 hrs of exposure at 1130 °C. In both cases, due to the volatility of fluorine, the synthesis was carried out in soldered platinum dishes.

Pure fluoralinite could be synthesized only by applying a special method for preparing the reagents (drying in hot kerosene) [5]. According to the author of [5], pure fluoralinite synthesized with this procedure is stable at temperatures above 1103±3 °C. According to [6], pure fluoralinite is unstable at temperatures lower than 1130 °C and higher than 1175 °C. Cooled slowly, it decomposes into CaO, CaF_2, and $2CaO{\cdot}SiO_2$. Above 1185 °C, fluoralinite decomposes, forming monoclinic alite – $3CaO{\cdot}SiO_2$, containing some fluorine ions and CaF_2. An additive of MgO, Al_2O_3, Fe_2O_3 reduces the temperature of formation of fluoralinite to 950–1000 °C [7]. It was synthesized from the mixture of MgO (1%), Al_2O_3 (1%), Fe_2O_3 (1%), and Mn_2O_3 (2%) additives. Akaiwa et al. [8] have noticed that this compound forms in raw materials containing fluorine already at 850 °C. At 1100 °C, fluoralinite containing magnesium, iron and aluminium in the crystal lattice decomposes into CaF_2 and alite $3CaO{\cdot}SiO_2$.

Therefore, on burning initial mixtures containing fluorine, fluorine-containing intermediate minerals of clinker are formed. The hydration of these minerals has not been investigated properly. After investigating properties of fluorine-containing minerals of clinker and their hydration, an optimal composition of clinker and optimal conditions of its synthesis should be possible to determine. Currently, more attention has been paid to the modification of clinker and its minerals. Cement with a larger amounts of fluorine, iron, sulphur, and chlorine can be produced by burning initial mixtures at reduced temperatures.

The aim of this work was to determine conditions of the synthesis of fluoralinite cement and to investigate its properties, such as fluoralinite paste setting and the hydration of mortar formed from mixtures of fluoralinite clinker and ground quartz sand at room temperature and in hydrothermal conditions.

2. Experimental

The materials used in the research were: $CaCO_3$ (POCh S.A., Poland; min. 99% $CaCO_3$; pure p.a.); amorphous $SiO_2{\cdot}nH_2O$ (loss of mass on ignition 20.4%; Krasny Khimik Sankt Petersburg, Russia; pure); Fe_2O_3 (POCh S.A., Poland; min. 96% Fe_2O_3; pure); $Al(OH)_3$ (Poch S.A., Poland; min. 63–67% Al_2O_3; pure p.a.); $MgCO_3$ (POCh S.A., Poland; min. 24% Mg; pure p.a.); CaF_2 (POCh S.A., Poland; min. 98% CaF_2; pure).

X-ray diffraction analysis was carried out using a DRON-6 diffractometer with Ni-filtered CuK_α radiation. The radiation angle 2Θ was changed in the range 4–60°. Thermographic investigations were carried out by using an STA 409 PC differential scanning calorimeter from Netzsch. The maximum temperature was 1500 °C, and the rate of temperature change was 10 °C/min. IR spectra were recorded with a Perkin

Elmer FT-IR System spectrometer. For the IR analysis, 1 mg of the substance was mixed with 200 mg of KBr and compressed in a forming press under vacuum. Hardening of the samples was carried out in hydrothermal conditions in an autoclave at 175 °C for 4 h. The compression strength was determined by using a model R-05Y4.2 device. The amount of free CaO in the burned samples was determined by the accelerated determination of free CaO.

The chemical content of the initial mixture was chosen (Table 1) according to the theoretical probability of $(3CaO{\cdot}SiO_2)_3{\cdot}CaF_2$ formation. The amount of additives (MgO, Al_2O_3 and Fe_2O_3) corresponds to the solubilities of these oxides in the tricalcium silicate lattice.

Table 1. The chemical composition of the initial mixture, wt. %

Oxide	CaO	SiO_2	Al_2O_3	Fe_2O_3	MgO	F_2
Percentage	63.22	21.99	0.89	0.89	1.78	11.23

The fluoralinite mixture of the initial dry components was thoroughly mixed in a porcelain mill for 1.5 hrs. After milling, the powder was pressed into cylindrical tablets. Then, in an electric stove, part of them were burned at 1050 °C for 1 h, and another part at 1100 °C for 4 h. After burning, the samples were cooled to room temperature, ground and sieved through No. 008 (80 μm) sieve.

3. Results and discussion

Fluoralinite forming conditions. Thermal analysis of the initial fluoralinite mixture has shown (Fig. 1) that a dehydration occurs at 90–100 °C (loss on ignition of the mixture at 90–150 °C was 6%, ΔH = 154 J/g). At 306 °C, a partial dehydration of β-$Al_2O_3{\cdot}3H_2O$ (bayerite) occurs and α-AlO(OH) (bemite) is formed (ΔH = 95.21 J/g, the mass loss of the mixture at 280–340 °C was 5.38%), and at 524 °C bemite completely dehydrates (ΔH = 32.11 J/g, the mass loss at 500–550 °C 0.82%). At 800 °C, γ-Al_2O_3 recrystallizes into α-Al_2O_3. The exothermic effect is suppressed, however, by the endothermic dissociation of $CaCO_3$. The decomposition of $CaCO_3$ into CaO and CO_2 starts approximately at 700 °C (ΔH = 694.2 J/g, mass loss of the mixture at 700–880 °C was 21.32%). The process being slow at the beginning, intensifies at 800 °C and at 857.7 °C its rate reaches a maximum. The total mass loss of the mixture at 90–1000 °C is 33.52%.

On burning the initial mixture at 1050 °C for 1 h, $CaCO_3$ decomposes into CaO, a part of which reacts with amorphous SiO_2 and forms belite β-$2CaO{\cdot}SiO_2$ (Fig. 2, curve 1) (CaO = 20.44%). If fluorine compounds are present in the initial mixture, belite forms at lower temperatures than in the batches without fluorine compounds. In accordance with literature data [1, 3], fluorspurite $(2CaO{\cdot}SiO_2)_2{\cdot}CaF_2$ may

also exist, though it has not been detected under the conditions of our experiments. Increasing the temperature to 1100 °C and prolonging the burning time to 4 h, results in fluoralinite $(3CaO{\cdot}SiO_2)_3{\cdot}CaF_2$ and γ-$2CaO{\cdot}SiO_2$ prevailing in the mixture (Fig. 2, curve 2). Also, intangible quantities of CaF_2 and CaO (CaO = 6.53%) remain. The samples disintegrate on cooling because additives with fluorine compounds promote the polymorphic transition of β-$2CaO{\cdot}SiO_2$ into γ-$2CaO{\cdot}SiO_2$.

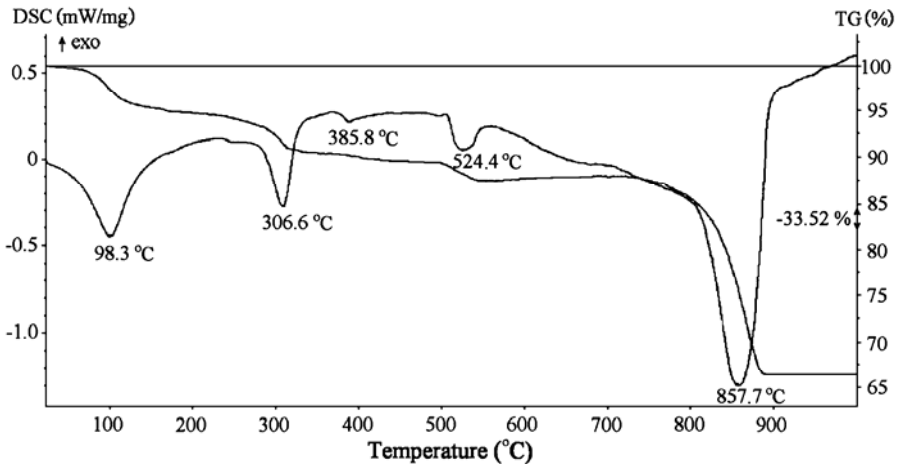

Fig. 1. Thermograms of unburned fluoralinite mixtures

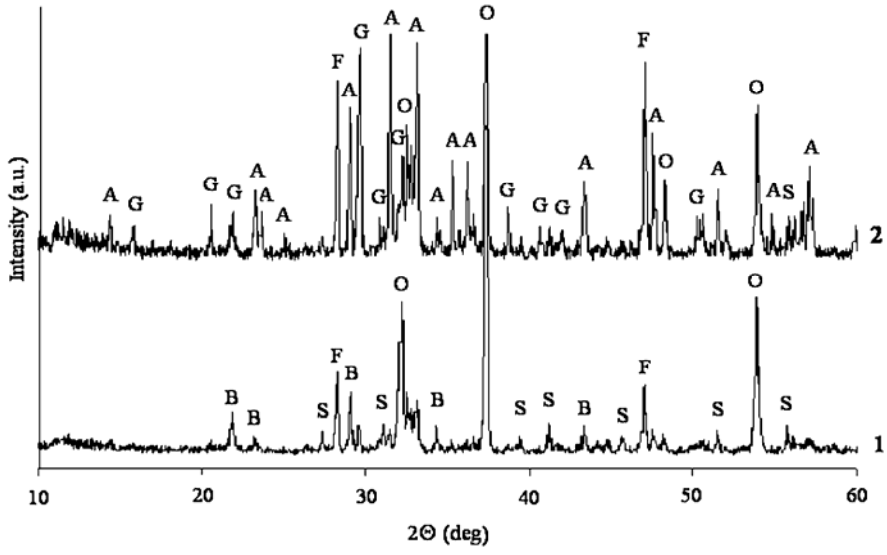

Fig. 2. X-Ray diffraction patterns of fluoralinite mixtures: 1 – burned at 1050 °C for 1 h; 2 – burned at 1100 °C for 4 h; F – CaF_2; O – CaO; B – β-$2CaO{\cdot}SiO_2$; G – γ-$2CaO{\cdot}SiO_2$; A – fluoralinite $(3CaO{\cdot}SiO_2)_3{\cdot}CaF_2$; S – SiO_2

Hydration of fluoralinite mortar. The binding and hardening of cement is the result of interaction between cement powder and water. After mixing Portland cement with water, constituent minerals form various hydrated compounds. The binding properties of fluoralinite clinker have been investigated according to the Portland cement investigation methods [5]. The specific surface area of ground fluoralinite clinker was 460 m^2/kg. Its pastes were prepared using standard water. The consistency and setting time were determined directly using a Vicat apparatus. For fluoralinite clinker paste, the initial set of normal consistency was 9 h, while the final set was 10 h. Compared to the requirements for Portland cement, the initial set of binding was late. Approximately after 10 h from the onset of hydration, a sudden hydration starts and the water in the paste is used to form the new crystals.

The dough of the mortar is formed from the mixture of the fluoralinite clinker and ground quartz sand (with the specific surface area S = 352 m^2/kg), in various ratios: 1:1 (mix 1), 1:2 (mix 2), and 1:3 (mix 3). The ratio of water to solid substances, V/K, was 0.5. The fresh dough of the mixture was moulded in 2 cm steel cubes. Part of them were cured in 90% relative humidity (RH) at 20 ºC for 24 h, then specimens were remoulded and cured under tap water for 3, 7, 14, and 28 days at 20 ºC, and finally broken. Another part of them was processed for 4 h at 175 °C in hydrothermal conditions, i.e. under saturated water vapour. After exposure, their compression strengths were determined. Six samples were measured for each test, and the mean values were considered.

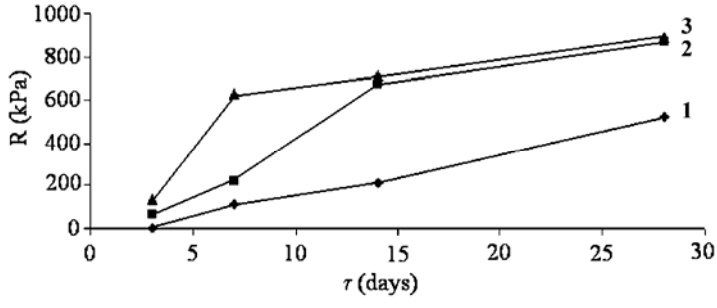

Fig. 3. Compression strength of fluoralinite mortar during hardening in normal conditions with ratios of fluoralinite mix to quartz sand: 1 – 1:1; 2 – 1:2; 3 – 1:3

It was determined that the strengths of all specimens increased, but the rate of strength increase was not constant (Fig. 3). At the initial stage of the experiment (until 7 days), the specimen strength increases depending on the amount of quartz sand. The samples having been formed from the mixture of fluoralinite and quartz sand with the ratio of 1:3 (mix 3) developed a compression strength of about 650 kPa, while the smallest strength was obtained for the specimen with the least amount of sand (the strength of mix 1 was approximately 110 kPa). After 14 days, the compression strengths of mixtures 2 and 3 reached approximately 710 kPa, and slightly increased further after 28 days by reaching ca. 880 kPa. The strength of the specimens of mix-

tures in which the fluoralinite cement and quartz sand ratio is 1:1 (mix 1)grew slower and after 28 days of hardening reached only 500 kPa. From the obtained results, a positive influence of sand additive on sample strength is evident.

For the 1:1 ratio of fluoralinite to sand, it was determined that the compression strength was 1.34 MPa after hardening at 175 °C (τ_{iso} = 4 h) in saturated water vapour. In normal conditions, the largest compression strength of approximately 520 kPa was recorded after 28 days. By increasing the quantity of sand in the mixture to the ratio of 1:2, the compression strength of autoclave products was increased to 2.31 MPa. The most significant compression strength, 4.68 MPa, was attained for the optimal ratio of 1:3 (Fig. 4).

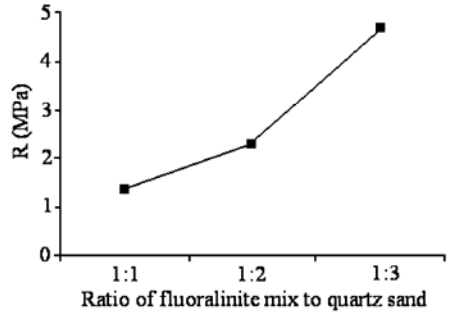

Fig. 4. Compression strength of fluoralinite mortar hardened at 175 °C for 4 h

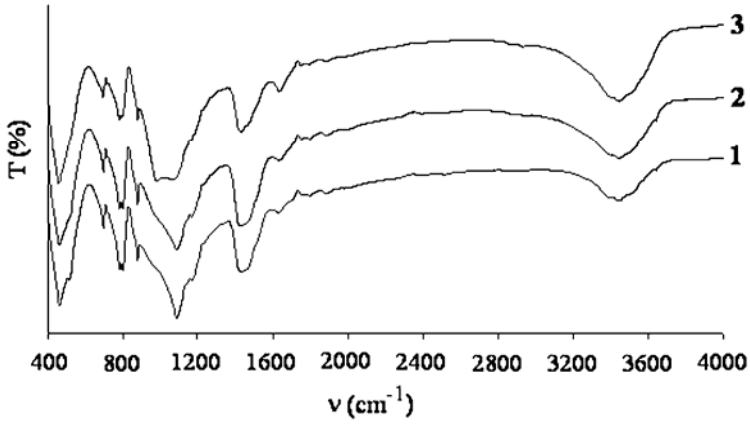

Fig. 5. IR spectra of the mortar dough of mixture 1: 1 – after 3 days of hydration; 2 – after 28 days of hydration, 3 – cured at 175 °C for 4 h

When investigating the differences in the structures of crystal materials, valuable information can be derived from infrared (IR) spectra. The IR spectra (Fig. 5) of mixture 1 are nearly identical. The most important difference appears in the spectra of the samples processed hydrothermally at 175 °C for 4 h (Fig. 5, curve 3) differ most con-

siderably. The distinct band of selective absorption in the frequency range 1250–830 cm^{-1} indicates valence vibrations of Si–O and Al–O bonds. The band at 450 cm^{-1} is typical of the active inner vibrations in the SiO_4^{4-} tetrahedron. Moving on from the island, group, and ring silicates to chain, layer, and network ones (quartz), the IR absorption band in the range 1250–830 cm^{-1} shifts to higher frequencies). In all samples the ν_1 vibrations of CO_3^{2-} are dominant for the 875 cm^{-1} frequencies, and ν_2 (CO_3^{2-}) prevail in the range 1400–1500 cm^{-1}.

A typical double band of the Si–O–Si bond is seen in the range 770–790 cm^{-1} of the IR spectrum. On the basis of IR spectra, water forms are ascertained. Absorption bands at 1650 cm^{-1} indicate deformation vibrations of simple water molecules, and broader absorption bands in the range 2800–3700 cm^{-1} imply vibrations of OH^- groups.

In the IR spectra of mixture 2, the same changes occur as for mixture 1, only the vibrations of CO_3^{2-} are different. Also, during the hardening of the sample in normal conditions, there is no absorption band at 1650 cm^{-1}, typical of deformation vibrations of simple water molecules. It appeared, however, in samples cured at 175 °C for 4 h. Since water present in the mixture is not bound by hydrogen bonds, a narrow absorption band at 3700 cm^{-1} exists, which corresponds to the vibrations of isolated OH^- groups.

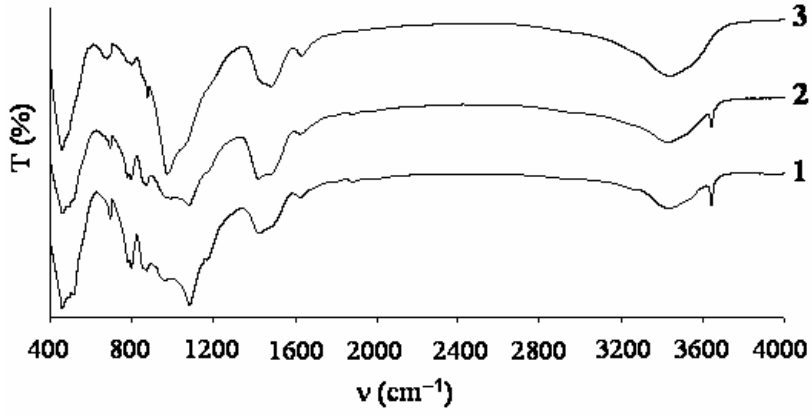

Fig. 6. IR spectra of the mortar dough of mixture 3: 1 – after 3 days of hydration; 2 – after 28 days of hydration, 3 – cured at 175 °C for 4 h

By analysing the IR spectra (Fig. 6) of mixture 3, it has been established that the spectra of silicon-oxygen compounds are typical and consist of two distinct selective absorption bands: in the range 1250–830 cm^{-1} (valence Si–O bonds and Al–O vibrations) and in the range 590–500 cm^{-1} (deformation vibrations of Si–O bonds).

Absorption bands at 1650 cm^{-1} represent deformations of simple water molecules. The absence of an absorption band at 3700 cm^{-1} indicates that there are no isolated OH groups in mixture 3.

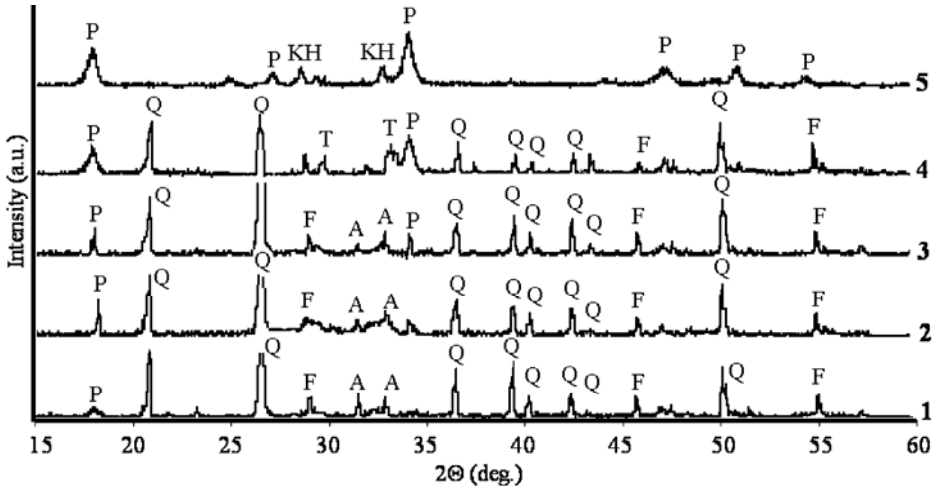

Fig. 7. X-Ray diffraction patterns of the hydration of mixture 3: 1 – after 3 days of hydration; 2 – after 7 days of hydration, 3 – after 14 days of hydration; 4 – after 28 days of hydration; 5 – cured at 175 °C for 4 h. F – CaF_2; P – $Ca(OH)_2$; A – fluoralinite $(3CaO{\cdot}SiO_2)_3{\cdot}CaF_2$, KH – C-S-H(I) calcium silicates hydrate; Q – SiO_2 (quartz); T – tobermorite gel

Based on the X-ray analysis of mixture 3 mortar (Fig. 7), it was established that after 3 days of hydration, quartz, $Ca(OH)_2$, and CaF_2 prevail in the specimen. They remain stable after 28 days of hydration at normal conditions. During the primary stages of hardening, until 14 days of hydration, fluoralinite $(3CaO{\cdot}SiO_2)_3{\cdot}CaF_2$ was still detected. After 28 days of hydration at normal conditions, it was no longer found and new hydration products, namely tobermorite gel and portlandite $Ca(OH)_2$, were formed.

During the hardening of the fluoralinite mortar in hydrothermal conditions (in an autoclave), portlandite $Ca(OH)_2$ forms and, together with the calcium oxide present in the clinker, reacts with quartz. Consequently, low base calcium hydrosilicate C–Si–H (I) is formed. After hydrothermal processing, spectral features of neither quartz nor fluoralinite are recorded.

The X-ray diffraction patterns of the hydration products of mixtures 1 and 2 are similar.

4. Conclusion

The mixture of Al_2O_3 (0.89%), Fe_2O_3 (0.89%), MgO (1.78%), and CaF_2 (11.23%) additives in cement batch burned at 1100 °C for 4 h gives fluoralinite. At 1050 °C, attempts of synthesizing fluoralinite were unsuccessful.

In the conditions of our experiments, samples formed from fluoralinite clinker and quartz sand (1:3), autoclaved at 175 °C for 4 h, have the largest strength (4.68 MPa). Thus, fluoralinite clinker is appropriate for being used in autoclave products.

X-Ray analyses have shown that when the mixture of fluoralinite and quartz sand is hardened for 28 days in normal conditions, quartz, tobermorite gel, portlandite $Ca(OH)_2$, and CaF_2 prevail in the samples. When the fluoralinite mortar is hardened in hydrothermal conditions (in an autoclave), portlandite $Ca(OH)_2$ and low base calcium hydrosilicates C-S-H (I) are formed.

Bonds between Si–O, Al–O, Si–O–Si, OH^-, and CO_3^{2-} prevail in the obtained samples of fluoralinite mortar.

References

[1] LUDWIG U., URBONAS L., Zement-Kalk-Gips, 46 (1993), 568.
[2] MOIR G.K., Phil. Trans. Roy. Soc. Lond., 310 (1983), 127.
[3] OLDEL J., ABDUL-MAULA S., J. Amer. Ceram. Soc., 70 (1987), 39.
[4] GILLIOLI C., MASSAZZA F., PEZZUOLI M., Cem. Concr. Res., 9 (1979), 295.
[5] GORSHKOV V.S., TIMASHEV V.V., SAVELJEV V.G., *Physical and Chemical Analysis Methods of Binding Materials* (in Russian), Vysshaya Shkola, Moscow, 1981.
[6] GUTT W., OSBORNE J.P., Trans. Brit. Ceram. Soc., 67 (1968), 125.
[7] KIM Y.M., HONG S.H., KIM H., J. Amer. Ceram. Soc., 85 (2002), 1941.

Received 30 September 2005
Revised 21 February 2006

Materials Science-Poland, Vol. 24, No. 2/1, 2006

Influence of tribomechanical milling and activation of primary mixtures on the synthesis of calcium silicate hydrates

D. PALUBINSKAITĖ*, A. KANTAUTAS

Faculty of Chemical Technology, Kaunas University of Technology,
Radvilenų str. 19, 50254 Kaunas, Lithuania

Minerals of the tobermorite group with double [Al^{3+}+Na^{+}] substitutions were synthesized using both, non-ground raw mineral mixtures and mixtures ground in a colloidal mill. The synthesis of calcium silicate hydrate is more effective when dry primary mixtures ground in a colloidal mill are taken, because compositions of higher degree of crystallinity are synthesized under the same conditions. In the latter case, tobermorite is formed after 24 h. It is thought that grinding a mixture of CaO, SiO_2 and Al_2O_3 in a colloidal mill induces activation centres which later activate synthesis via hydrothermal processing. It is reasonable to grind dry reactants used for synthesising tobermorite in a colloidal mill before hydrothermal processing. Under our experimental conditions, tobermorite was formed more effectively when the specific surface was lower than 547 $m^2 \cdot kg^{-1}$. Use of finer particles of reactants does not enhance the reaction rate because of the stabilising influence of $(0.8–1.5)CaO \cdot SiO_2 \cdot (0.5–2.5)H_2O$ (C–S–H (I)) on the overall reaction rate of the synthesis of tobermorite.

Key words*: [Na^{+} + Al^{3+}]- inserted tobermorite; hydrothermal synthesis; mechanical processing*

1. Introduction

Tribomechanics is a branch of physics investigating phenomena appearing during grinding in dynamic conditions. Tribomechanical milling and activation at room temperature has been investigated for several primary material mixtures ground in colloidal mills. The results have demonstrated that tribomechanical processing is the cause of a noticeable decrease in particle size, changes in particle distribution and increase of their specific surface area. Mechanical activation of solid-phase reactions was first investigated almost one and a half centuries ago. Along with the development of theo-

*Corresponding author, e-mail: danute.palubinskaite@ktu.lt

retical mechanochemistry, its technical use in modifying mineral resources, chemical catalysis, and syntheses of new materials were studied.

Mechanical impact on reagents in solid phases comes in various forms: dispersing larger particles by grinding or by blows, pressing of powders, cold processing of metallic and non-metallic materials, forming by blast, etc. The practical importance of dispersion is that a decrease of the particle size results in an increase surface areas and, consequently, in shortening of the diffusion paths of the reagents. Due to this, several process occur as lower temperatures, hence the energy used can be lower [1, 2].

Of all activating methods, dispersion or grinding is used most often. A decrease of particle dimensions is not the only result of the grinding process. As the particle size decreases, the structure of the crystal lattice may change, energy levels are modified, and electron emission and other processes may appear.

Under forces exerted by grinding bodies, solid particles undergo elastic and, later, plastic deformation until the pressure becomes larger than the material can withstand. The particles then split into much smaller ones, and those smaller particles undergo a further dispersion at a certain rate. The mechanical energy is thus distributed into elastic and plastic deformations, while new surfaces appear due to breaking chemical bonds and movement of particles [1].

A reduction of particle size often causes an increase in the process rate because the id decreases the diffusion paths of reactants and products of a reaction to and from surfaces. In practice, the reaction rate depends on the sizes of particles of all reactants, in rare cases it depends on only one of the components [1]. Unfortunately, all mechanical dispersion methods have a common disadvantage which becomes especially noticeable while processing materials sensitive to micro-dashes. Therefore, along with mechanical milling, ultrasound and electro-erosive treatment is used [3].

Phases consisting of CaO, SiO_2, and H_2O are called calcium silicate hydrates (KSH). In industry, tobermorite is usually obtained by processing mixtures of $Ca(OH)_2$ and SiO_2 in an autoclave, at a temperature of saturated water vapour from 120 °C to 200 °C. In our experiments, tobermorite was synthesized by processing a mixture of CaO, SiO_2 and water, taken in various proportions of calcium hydroxide and silica, in a Fritch–Pubversirte planetary mill. The frequency of drum revolutions was 700 rpm. According to the chemical reaction of tobermorite synthesis

$$5Ca(OH)_2 + 6SiO_2 \rightarrow Ca_5(OH)_2Si_6O_{16}\cdot 4H_2O$$

the stoichiometric CaO to SiO_2 molar ratio is $C/S = 5/6$. The ratio of water to solid reagents was $V/K = 1/4$. Examining X-ray diffraction patterns, it was found that after 45 minutes milling, a peak for tobermorite appears, becoming more intense after 1.5 h, whereas the $Ca(OH)_2$ peak gradually fades. After 5 hours, the primary materials react almost completely and convert into tobermorite. This has been proved by comparing samples of tobermorite obtained mechanochemically with the ones obtained in the autoclave: deviations from stoichiometry were insignificant [4].

The effect of Al_2O_3 and NaOH on the formation of 1.13 nm tobermorite under hydrothermal conditions was studied. Also, the ion exchange capacity of tobermorites with and without Al^{3+} as well as with double [$Na^+ + Al^{3+}$] substitutions in relation to heavy metal ions was investigated [7]. The effect of inorganic additives on the system $CaO–SiO_2–H_2O$ has been investigated by many authors [8–10]. Among inorganic additives containing aluminium and sodium, oxides play a significant role in the mechanism and kinetics of the synthesis of calcium silicate hydrate [11].

There has been a lack of data in the literature on the influence of mechanical activation of primary mixtures by using [$Na^+ + Al^{3+}$] ions as additives in tobermorite synthesis. Therefore, the aim of this work was to synthesize tobermorite group minerals with [$Na^+ + Al^{3+}$] ions inserted into the crystalline lattice and to investigate the influence of their mechanical processing on tobermorite synthesis.

2. Materials and methods of testing

Reactants of p.a. purity were used in this work: silica gel $SiO_2 \cdot nH_2O$ (loss on ignition – 23.5%, SiO_2 – 76.5%), amorphous Al_2O_3 (obtained by heating $Al(OH)_3$ at 550 °C for 0.5 hour, specific area S = 505 $m^2 \cdot kg^{-1}$), calcium oxide (CaO – 98%, obtained by calcination of calcium carbonate at 1000 °C), NaOH aqueous solution (33.5 wt.%).

X-ray diffraction analysis was conducted with a DRON-6 diffractometer. The investigation was carried out within a 2Θ angle range of 4–60°, with Ni-filtered CuK_α radiation. A DuPont 990 thermal analyser was applied for differential scanning calorimetry (DSC) studies, with the rate of temperature increase of 10 °C/min and maximum temperature of 1200 °C. The specific surface area of the raw materials was determined by Blain's method. Particle distribution and the average diameter of grains were determined by means of a laser granulometer ("FRITCH Analysette 22", Germany). Samples were kept in water for 20 s. The mode of ultrasound dispersion was 250 relative units. The mixer turning speed was 300 rpm. The mode of pump operation was 200 relative units. The synthesis of calcium silicate hydrates was executed by mixing suspensions in a 250 ml autoclave, the turning speed of which was 16 rpm.

3. Results and discussion

The rate of reaction depends primarily on the particle sizes of primary components. For the synthesis of tobermorite with inserted [$Na^+ + Al^{3+}$] ions, a mixture of primary components (1) (S = 212 $m^2 \cdot kg^{-1}$) was used, its composition being: $C/(S + A)$ = 0.83 and $A/(S + A)$ = 0.025 in molar rations (here C, S and A stand for number of moles of CaO, SiO_2 and Al_2O_3, respectively). A part of the mixture was ground using different grinding modes in a colloidal mill, producing three additional mixtures (2), (3), and (4), with S = 547, 750, and 1040 $m^2 \cdot kg^{-1}$, respectively.

Results obtained on samples synthesised with [Na^+ + Al^{3+}] added were compared with those obtained without the addition. In the latter case, the molar ratios were *C/S* = 0.83, and the specific surface areas were 230, 650, and 900 kg/m^2. The distribution curves and average grain diameters were determined for non-ground and mechanically processed mixtures 2, 3, and 4 (Fig. 1). According to granulometric analysis, it can be seen that although the character of the granulometric distributions is similar, in mixture 1 domensions of most particles range from 114 to 133μ, whereas in mixture 2 from 97 to 114 μ, in mixture 3 from 60 to 70 μ, and in mixture 4 from 50 to 60 μ.

According to the X-ray diffraction analysis, CaO prevailed in the non-ground mixture. After grinding in a colloidal mill, amorphous silica gel, CaO and $Ca(OH)_2$ prevailed (Fig. 2, curves 2, 3). Grinding, resulting in higher specific surfaces of the samples (mixture 4), causes almost all CaO convert into $Ca(OH)_2$ with H_2O taken from silica gel (Fig. 2, curve 4).

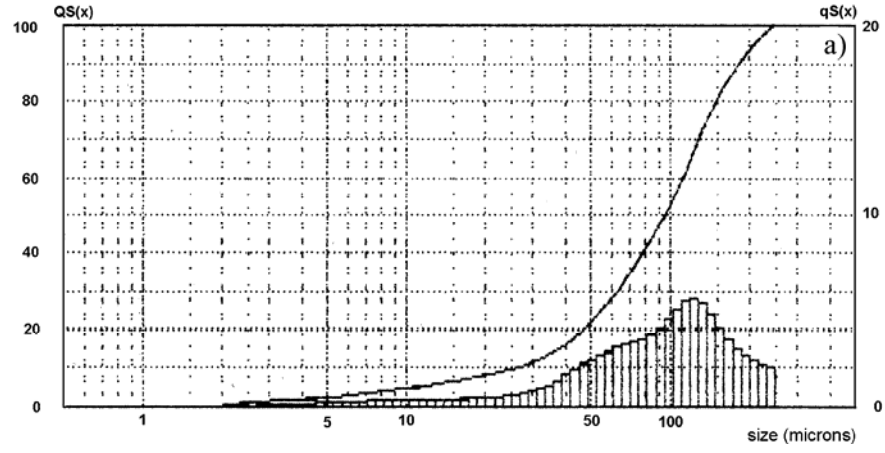

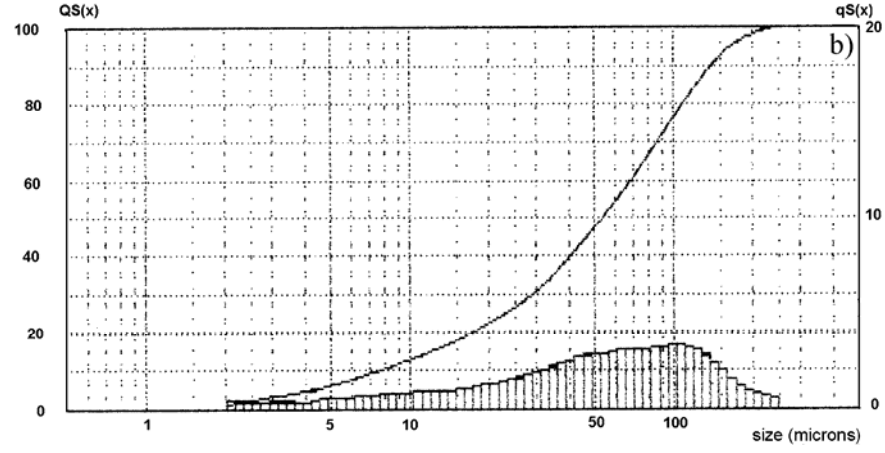

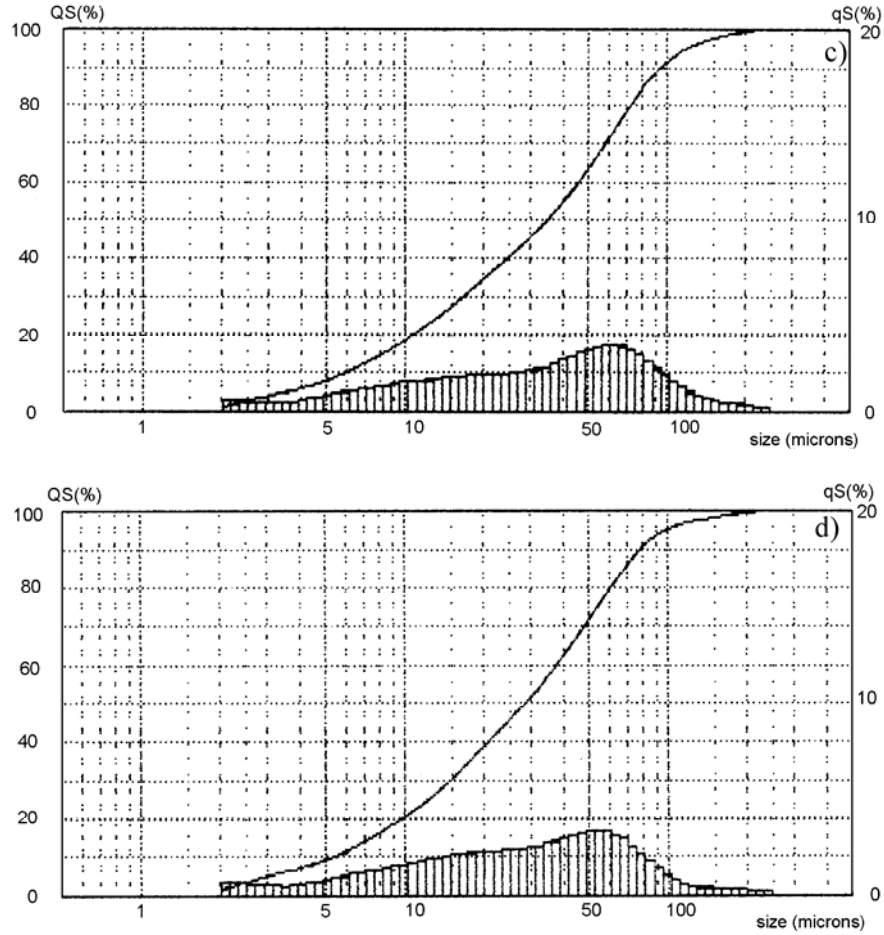

Fig. 1. Distribution of the particles in the mixture ($SiO_2 \cdot nH_2O$ + CaO + Al_2O_3). Specific surfaces S ($m^2 \cdot kg^{-1}$) of the mixtures were: a) 212, b) 547, c) 750, d) 1040

Therefore, the cubic lattice of CaO in the primary mixtures transforms into the hexagonal $Ca(OH)_2$ lattice during grinding and dispersing due to the chemical reaction. According to the literature [5], the unit cell volume practically does not change during the transition. The noticed increase in the volume of the system is therefore related to the dispersion of CaO during the topochemical reaction and the increase in intergrain porosity.

After conducting the thermal analysis of the three dry mixtures, it appeared that the DTA and TG curves are nearly identical for all the mixtures (Fig. 2, b). The endothermic peak at 480 °C is due to the dehydratation of $Ca(OH)_2$. Since dry mixtures containing either CaO and $SiO_2 \cdot nH_2O$, or CaO + $Ca(OH)_2$ and $SiO_2 \cdot nH_2O$ were used, water in the silica gel had apparently reacted with CaO and formed $Ca(OH)_2$. For this reason, the DSC and TG curves of all mixtures were very similar.

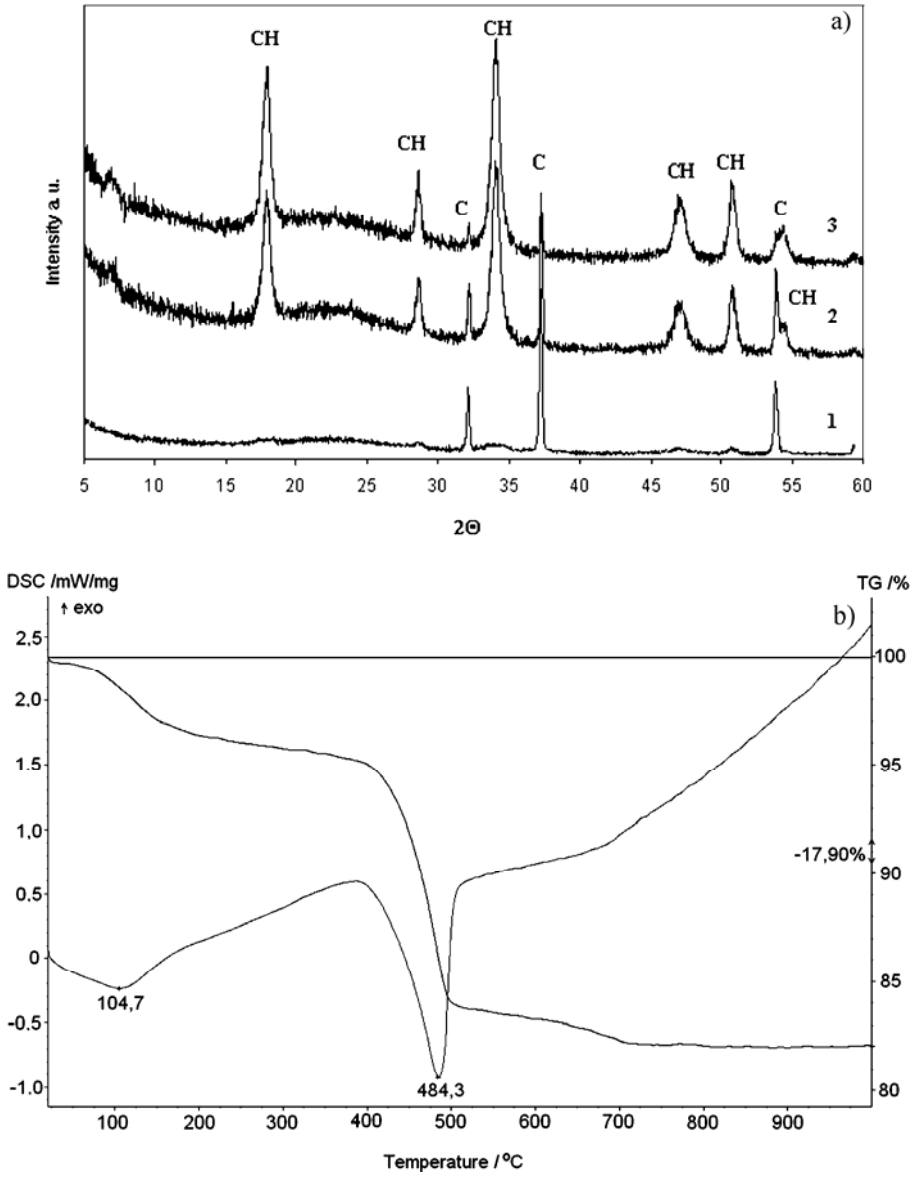

Fig. 2. X-ray diffraction patterns (a) and thermogram (b) of initial dry mixtures (CaO, amorphous $SiO_2 \cdot nH_2O$ and Al_2O_3): 1 – non-ground with S = 212 $m^2 \cdot kg^{-1}$, 2 – ground to S = 547 $m^2 \cdot kg^{-1}$, 3 – ground to S = 750 $m^2 \cdot kg^{-1}$, 4 – ground to S = 1040 $m^2 \cdot kg^{-1}$; CH – $Ca(OH)_2$; C – CaO

Mechanically activated primary mixtures necessary for KSH synthesis, of different degree of dispersion, were mixed with water in the water (W) to solid suspension (S) weight ratio W/S = 10. This was supplemented by an addition of 5% Na_2O according to the mass of the dry materials. The suspension so obtained was mixed before the synthesis. The hydrothermal synthesis was accomplished in 4, 6, or 24 hours, at

175 °C or 200 °C. After hydrothermal processing, the products of synthesis were filtered and dried at 105±5 °C.

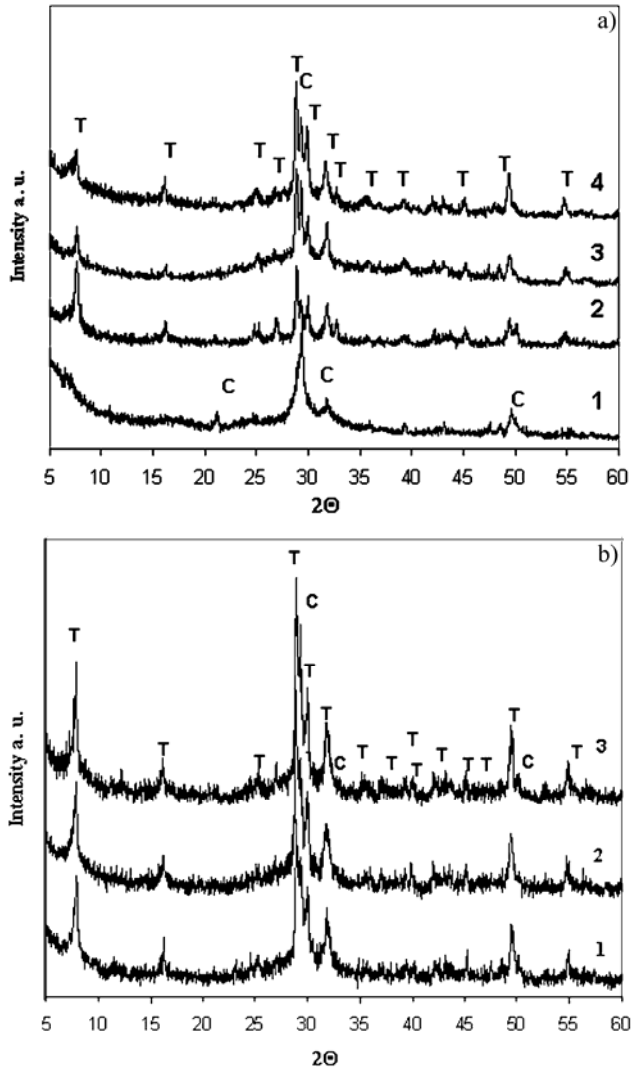

Fig. 3. X-ray diffraction patterns of calcium silicate hydrates modified with [Na^+ + Al^{3+}] (a) and without additives (b), synthesized for 24 hours at 175 °C. The specific surfaces *S* ($m^2 \cdot kg^{-1}$) were: a) 1 – 212, 2 – 547, 3 – 750, 4 – 1040, b) 1 – 230, 2 – 625, 3 – 900 .
T – tobermorite; C – (0.8–1.5)$CaO \cdot SiO_2 \cdot$(0.5–2.5)H_2O (C–S–H (I))

From a comparison of X-ray diffraction patterns (Fig. 3), it has been established that addition of [Na^+ + Al^{3+}] slows down tobermorite formation, and that the fineness of the reactant mixture affects the product formation. A large amount of crystalline tobermorite without any [Na^+ + Al^{3+}] addition (Fig. 3b) is formed in all cases and the

effect of grinding is small. Using a non-ground mixture (curve 1) or the one with a 900 $m^2 \cdot kg^{-1}$ specific surface area (curve 3) results, however, in no tobermorite C–Si– H (I).

It can be noticed that the fineness of the reactant mixtures does affect [$Na^+ + Al^{3+}$] substituted tobermorite synthesis. When using materials of a greater specific surface (750 and 1040 $m^2 \cdot kg^{-1}$) for synthesis (Fig. 3), calcium silicate hydrates of a lower degree of crystallinity were formed (the peaks in X-ray diffraction patterns are less intense 1.13; 0.297 0.280 nm), i.e. the processes proceeded more slowly and $(0.8–1.5)CaO \cdot SiO_2 \cdot (0.5–2.5)H_2O$ (C–S–H (I)) has not had time to recrystallise into tobermorite.

Butt and Raskovic [6] recommend using quicklime for silicate hydrate synthesis because fresh slack lime has a larger specific surface and exhibits a better reactivity, solubility, and activity than $Ca(OH)_2$ prepared in advance and well crystallised.

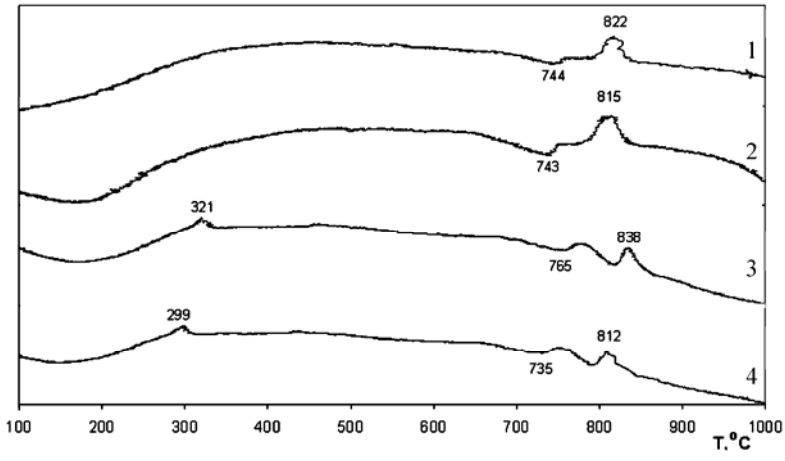

Fig. 4. Thermograms for modified calcium silicate hydrate for a primary mixture with the specific surface S = 1040 $m^2 \cdot kg^{-1}$ and synthesis modes: 1 – 175 °C, 24 h, 2 – 175 °C, 4 h, and in case of a primary mixture with the specific surface of S = 750 $m^2 \cdot kg^{-1}$: 3 –175 °C, 24 h, 4 –175 °C, 4 h

Along with X-ray diffraction pattern analysis, thermal analysis has also been conducted (Fig. 4). The analysis confirms the X-ray data: when the specific surface of the mixture is lower than 547 $m^2 \cdot kg^{-1}$, i.e. when CaO, SiO_2 and Al_2O_3 prevail in the mixture, products with a higher degree of crystallinity are synthesized. In the picture above, all the exothermic peaks in the range 812–838 °C suggest the crystallisation of C–S–H (I). The endothermic ones at 794 and 818 °C point to the decomposition of $CaCO_3$, and the peaks in the rage 735–765 °C are associated with the dehydration of tobermorite.

We can assert that in mixtures with large specific surfaces SiO_2 dissolves very rapidly in an autoclave while increasing the temperature, and reacts with $Ca(OH)_2$ while the semi-crystal C–S–H (I) is forming up. The crystallisation of this combination into 1.13 nm tobermorite takes a longer time. In addition, Al^{3+} ions insert themselves into the C–S–H(I) composition, and are located among the chains of the crystal grid thus, stabilising them.

4. Conclusions

It seems reasonable to grind dry component mixtures used for synthesising [Na^+ + Al^{3+}]-substituted tobermorite in a colloidal mill, before hydrothermal processing, but under experimental conditions of this work tobermorite was formed more effectively when the specific surface was lower than S = 547 $m^2 \cdot kg^{-1}$. Use of mixtures of finer primary materials is useless because of the stabilising effect of C–S–H (I) on the kinetics of tobermorite formation.

It has been determined that the addition of [Na^+ + Al^{3+}] slows down tobermorite formation. In this case, the fineness of primary material mixture strongly influences product formation. High crystalline tobermorite forms in all cases without the addition of [Na^+ + Al^{3+}] and the grinding influence of the primary material mixture is small.

When a non-ground mixture of the primary materials (with [Na^+ + Al^{3+}] added) is synthesised for 24 h at 175 °C, products with a higher degree of crystallinity are formed than in case of mixtures ground in a colloidal mill. [Na^+ + Al^{3+}]-substituted calcium silicate hydrate synthesis is more effective when dry primary mixtures ground in a colloidal mill are taken because compositions with a higher degree of crystallinity are synthesized in the same conditions. In this case, [Na^+ + Al^{3+}]-substituted tobermorite forms after 24 h. It is believed that grinding a mixture of CaO, SiO_2 and Al_2O_3 in a colloidal mill induces activation centres which later activate the synthesis in the process of hydrothermal processing.

References

[1] TRETYAKOV J.D., *Solid-State Reactions*, Moscow, Khimiya, 1985 (in Russian).
[2] GORSHKOV V.S., SAVELEV V.G., FEDOROV N.F., *Physical Chemistry of Silicates and Other Hardly Fusible Compounds*, Moscow, Vysshaya Shkola, 1988 (in Russian).
[3] BUTYAGIN P., Colloids Surf. A: Physicochem. Eng. Aspects, 160 (1999), 107.
[4] MI G. M., SAITO F., HANADA M., Powder Technology, 93 (1997), 71.
[5] MARTUSEVIČIUS M, KAMINSKAS R., MITUZAS J. A., *Chemical Technology of Binding Materials*, Kaunas, Tekhnologiya, 2002 (in Lithuanian).
[6] BUTT J.M., RASHKOVICH L.N., *Hardening of Binding Materials at High Temperatures*, Moscow, Stroiizdat, 1965 (in Russian).
[7] SIAUCIUNAS R., JANICKIS V., PALUBINSKAITE D., IVANAUSKAS R., Ceramics – Silikaty, 48 (2004), 76.
[8] NOCUŃN-WCZELIK W., Cement Concrete Res., 29 (1999), 1759.
[9] NELSON E.B., Cement Concrete Res., 7 (1977), 687.
[10] COLEMAN N. J., Mater. Res. Bull., 40 (2005), 2000.
[11] NOCUŃ-WCZELIK W., Cement Concrete Res., 27 (1997), 83.

Received 30 September 2005
Revised 21 February 2006

Materials Science-Poland, Vol. 24, No. 2/1, 2006

Preparation and upconversion properties of Er^{3+}, Yb^{3+}:$Y_2Si_2O_7$ nanocrystallites embedded in PVA polymer nanocomposites

D. HRENIAK[1*], P. GŁUCHOWSKI[1], W. STRĘK[1], M. BETTINELLI[2], A. KOZŁOWSKA[3], M. KOZŁOWSKI[3]

[1]Institute of Low Temperature and Structure Research, Polish Academy of Sciences, 50-422 Wrocław, Poland

[2]Dipartimento Scientifico e Tecnologico, Università di Verona and INSTM, UdR Verona, Ca' Vignal, Strada Le Grazie 15, I-37134 Verona, Italy

[3]Wrocław University of Technology, Materials Recycling Center of Excellence, 50-422 Wrocław, Poland

The preparation of polymer nanocomposites consisting of a poly(vinyl) alcohol (PVA) network and RE^{3+}:$Y_2Si_2O_7$ nanocrystalline particles (RE = Yb, Er) is presented. Optical properties of the nanocomposites were preliminarily studied. In particular, efficient upconversion was observed in Er^{3+} and Yb^{3+} co-doped $Y_2Si_2O_7$ nanoparticles embedded in the polymeric PVA host. It was found that the luminescence features of the RE^{3+}:$Y_2Si_2O_7$ nanoparticles were affected by the polymeric host, resulting in a shortening of their luminescence lifetimes. This effect is discussed in terms of the effective refractive index.

Key words: *nanocomposite; luminescence; upconversion process; rare earths*

1. Introduction

A nanocomposite is a mixture of different component materials, in which at least one being of nanometer scale. Such materials may display combined features of all components or quite new properties resulting from mutual interactions between components. Organic-inorganic polymer composites have recently found wide technological applications. In the last years, a special interest has been focused on nanocomposites based on polymer networks involving nanoparticles being characterized by different electric, magnetic, or optical features. Different kinds of materials, among which are sulfides, organic compounds, and oxides nanocrystals, have been proposed

[*]Corresponding author, e-mail:D.Hreniak@int.pan.wroc.pl

as nano-fillers in these composites [1, 2]. It is well known that yttrium disilicate doped with rare earth ions, especially Eu^{3+} and Tb^{3+}, is a very efficient phosphor material [3, 4]. Besides excellent luminescent properties, the morphology of these luminophors is important for perspective applications, and a spherical shape of the grains is preferred. For such applications, it is important to use particles not being aggregated and characterized by a narrow size distribution [5].

In the present paper, we report the preparation of polymer-based nanocomposites involving nanocrystalline RE^{3+}-doped $Y_2Si_2O_7$ particles, where Er^{3+} and Yb^{3+} are chosen as the active ions. Our interest was primarily focused on the upconversion effect, resulting in visible emission after infrared excitation. Such an effect has found application in the development of upconversion lasers [6] and for the labeling of products [7, 8].

2. Experimental

In the first stage of the process, a nanopowder of $Y_2Si_2O_7$ co-doped with 10% mol Yb^{3+} and 2% Er^{3+} ions was obtained. Tetraethoxysilane (TEOS), yttrium (Y_2O_3), and rare-earth oxides (Yb_2O_3 and Er_2O_3) were used as the starting materials. Samples of the nanocrystalline powders were obtained using the preparation method of yttrium disilicate described elsewhere [9]. Yttrium and lanthanides nitrates were obtained by reacting stoichiometric amounts of their oxides with nitric acid. TEOS was hydrolyzed by stirring the mixture $Si(OC_2H_5)_4$:H_2O:HCl (in the volume ratio of 7.5:10:0.002) at 50 °C for 2 hours. The obtained sols were mixed with yttrium and lanthanides nitrates (dissolved in 10 ml of H_2O) in a 1:1 molar ratio of (Y + Yb + Er) to Si. The sols were left for one week at room temperature for gelation. After this time, the obtained wet gels were dried at 90 °C for a week. The cracked gels obtained during drying were annealed at 1100 °C for 4 h to yield the silicate in crystalline form.

The polymer used in the study was poly(vinyl alcohol) PVA (Kurray, Japan). Nanocomposites were prepared by a solution casting method. Initially, the polymer was dissolved in water with a concentration of 15 wt. %, after which the nanofiller was added. Finally, the suspension was mixed with a high shear rate. The resulting slurry was poured out on a flat surface with high surface tension and the solvent was removed by evaporation. The polymer nanocomposite and undoped matrix in the form of thin films with the thicknesses of 0.14 μm and 0.10 μm, respectively, were evaluated for their optical properties by means of luminescence investigations. The nominal volume fraction of nanoparticles embedded in the polymer was estimated to be ~2%.

Overall phase compositions were determined by X-ray powder diffraction with a Siemens D5000 diffractometer and $CuK_{\alpha 1}$ radiation. The transmission spectrum was recorded using a Cary 5 spectrophotometer. Emission spectra were recorded, using a Jobin Yvon TRW 1000 spectrophotometer equipped with a laser diode (978 nm) as an excitation source, and a Hamamatsu R928 photomultiplier. Emission kinetics were measured with a Tektronics TDS 3052 oscilloscope, using an OPO laser system Continuum Surelite as the excitation source.

3. Results and discussion

Figure 1 shows the XRD pattern of the $Y_2Si_2O_7$ nanopowder annealed at 1100 °C in air. A well-defined α-$Y_2Si_2O_7$ structure was confirmed. Only a small shift in the diffraction peaks due to the replacement of Y^{3+} ions by smaller Yb^{3+} and Er^{3+} ions was observed. No structural impurities of other polymorphs of $Y_2Si_2O_7$ were found. The size of the grains was determined using Scherrer's equation and gave the average of 40 nm. Analogous materials were also proven to be nanostructured by TEM measurements in our previous work [9].

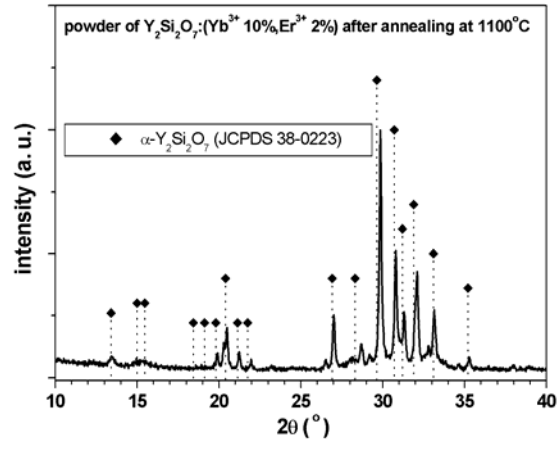

Fig. 1. XRD pattern of the $Y_2Si_2O_7$ powder after annealing at 1100 °C

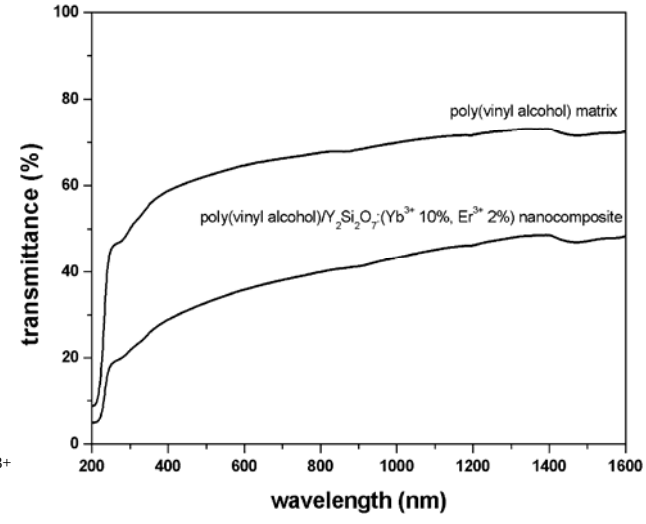

Fig. 2. Transmittance spectrum of a poly(vinyl alcohol) matrix and a poly(vinyl alcohol)/$Y_2Si_2O_7$:Yb^{3+} 10%, Er^{3+}, 2% nanocomposite

The transmission spectrum of the PVA polymer film is shown in Figure 2. One can see that transparency in this kind of matrix in the examined spectral range is rela-

tively high and comparable to that reported elsewhere [10]. The ~10% lower transmittance observed here is due to surface roughness, resulting from the casting of the PVA film. A significant decrease in transmittance, observed for the composite sample, is due to Rayleigh scattering from the embedded particles (their average size was 40 nm). No attenuation due to the scattering effect could be expected for particles smaller than 15 nm [11]. Additionally, a part of the agglomerated grains, with sizes close to the used wavelength, can provide Mie scattering. There is still sufficient transmittance both for infrared excitation around 1 μm and visible emission in the red spectral range. This means no important effects should appear in the emission characteristics due to light attenuation in the polymer matrix. In order to confirm this conclusion, the emission spectra of both the nanopowder and nanocomposite composed of the same nanopowder were recorded and compared.

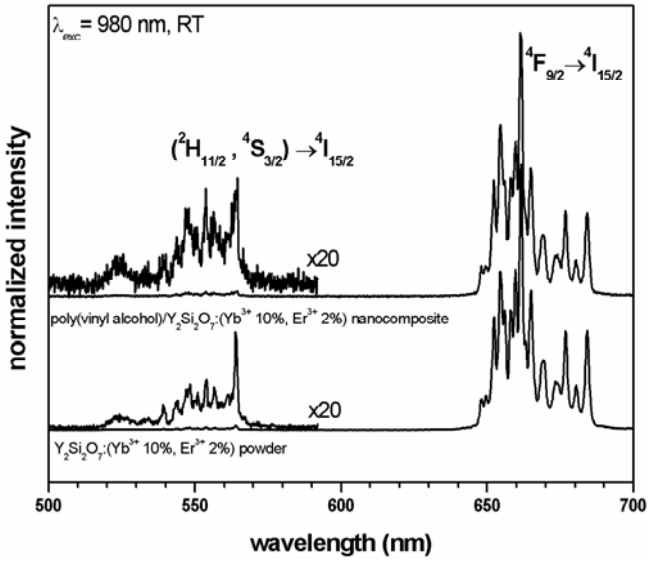

Fig. 3. Emission spectra of Er,Yb:$Y_2Si_2O_7$:as-made powder (bottom) and embedded into PVA polymer (top)

The luminescence spectra of polymer nanocomposite films were measured at room temperature when excited with a IR laser diode operating at 980 nm (Fig. 3). It is well known that at this excitation energy (10 204 cm^{-1}) there is a very efficient upconversion from the excited level $^2F_{5/2}$ of the Yb^{3+} ion (~ 10200 cm^{-1}), populating the $^2H_{11/2}$ level of the Er^{3+} ion (~ 20400 cm^{-1}), converting IR excitation into visible light [12, 13]. According to this mechanism, $^4F_{9/2}$ is populated by multiphonon relaxation from $^4S_{3/2}$. An additional upconversion mechanism directly populates the $^4F_{9/2}$ level without populating either $^2H_{11/2}$ or $^4S_{3/2}$ [14]. The scheme of the upconversion mechanisms in the Er^{3+} + Yb^{3+} codoped material is shown in Fig. 4.

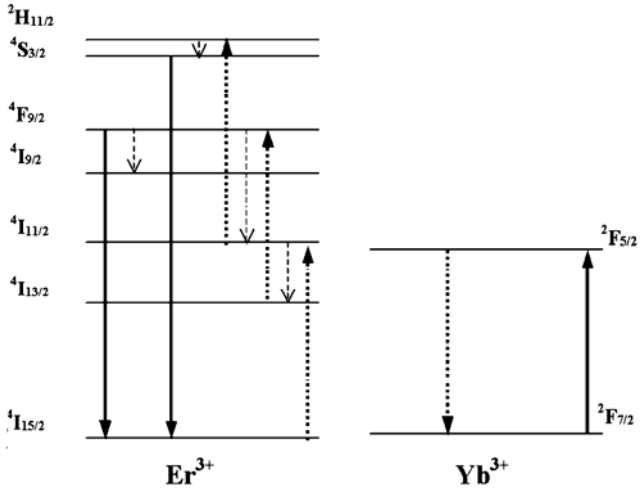

Fig. 4. Schemes of upconversion processes in the Er, Yb system

In the system under investigation, we have observed an efficient red luminescence centered at 670 nm, corresponding to the emission from the excited $^4F_{9/2}$ to the ground level $^4I_{15/2}$. Moreover, a weak emission in the green range (540–560 nm), assigned to the $(^2H_{11/2},^4S_{3/2})\rightarrow{}^4I_{15/2}$ transition, was recorded. The green emission is much weaker compared to the red one and was invisible with the naked eye. We measured the ratio of the integral red emission band intensity to the green band one, β, the ratio

$$\beta = \frac{I\left(^4F_{9/2} \rightarrow {}^4I_{15/2}\right)}{I\left(^4S_{3/2}, {}^2H_{11/2} \rightarrow {}^4I_{15/2}\right)} \tag{1}$$

to be 32 for the nanocomposite, whereas for the nanopowder it was slightly higher (~43). This means that for the nanocomposite the intensity of the green emission decreased compared to the red one. We point out that the fine structure of the observed transition is identical for the nanopowder and nanocomposite, indicating that the sites accommodating the dopant ions are identical for the two materials.

To get insight into the role of the host in affecting the emission transitions of the Er^{3+} ion, we have measured the emission decay curves of the red and green transition bands of Er, Yb:$Y_2Si_2O_7$ nanopowders and polymer nanocomposite films. They were measured at room temperature under the excitation of an OPO laser operating at 975 nm (Figs. 5 and 6).

We found that the decay curves were almost perfectly exponential. The measured emission lifetimes, given in the figures, are significantly shorter for both transitions in the case of the polymer nanocomposite as compared to the nanopowder. The measured luminescence lifetime was reduced by 23% (from 22 μs to 17 μs) for the more energetic $(^2H_{11/2},^4S_{3/2})\rightarrow{}^4I_{15/2}$ transition, and by 19% (from 38 μs to 31 μs) for the less energetic $^4F_{9/2}\rightarrow{}^4I_{15/2}$ transition.

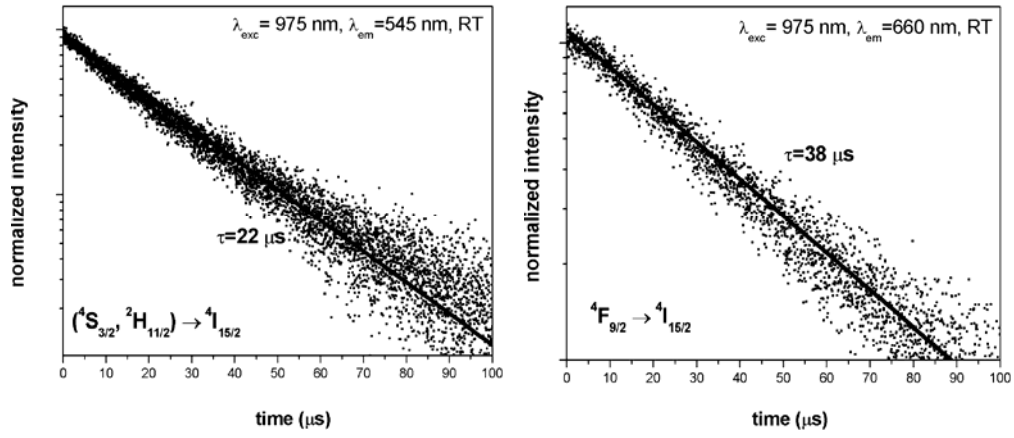

Fig. 5. Luminescence decays of the Er,Yb:$Y_2Si_2O_7$ powder

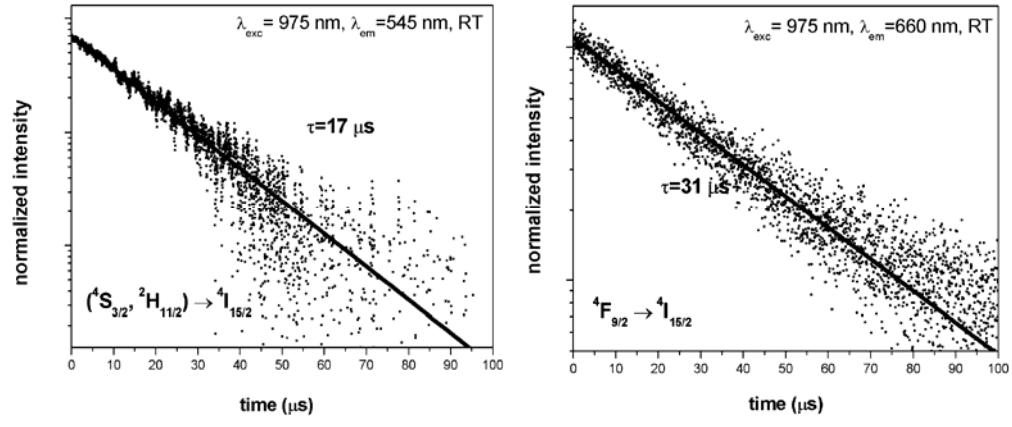

Fig. 6. Luminescence decays of Er,Yb:$Y_2Si_2O_7$ embedded into PVA polymer

Since the Er^{3+} ion is well-shielded form the high frequency vibration of the polymer, this behaviour indicates that the radiative decay rate of the dopant ions presumably increases for the polymer nanocomposite. Following recent results [15–18], we suppose that the host affects the radiative transition rate via enhancing the effective refractive index. The effective refractive index for nanocrystals embedded in host materials has been defined by Vetrone et al. [16] as

$$n_{\text{eff}}(x) = x\, n_{Y_2Si_2O_7} + (1-x) n_{\text{med}} \tag{2}$$

where x is the "filling factor" connected to the specific surface of the dispersed particles, illustrating the interface of nanocrystals and the medium, and n_{med} is the refractive index of the medium in which the nanocrystals are embedded. According to this relationship, given the refractive indices of the components ($n_{\text{PVA}} \sim 1.5$ [19], $n_{Y_2Si_2O_7} \sim 1.8$ [20], $n_{\text{air}} = 1$), the effective refractive index for nanocrystals of $Y_2Si_2O_7$ dis-

persed in PVA should be higher than for nanopowders in air (assuming a high surface of the powder, as observed in [16]). It can be easily checked that for each $x \neq 0$ used, n_{eff} (for $n_{\text{med}} > 1$) is higher than n_{eff} in air. As a result, by using n_{eff} in the place of n [21], the radiative lifetime τ_{R} of the electric dipole transitions, can be expressed as

$$\tau_R \propto \frac{1}{f(\text{ED})} \frac{\lambda_0^2}{\left[\frac{1}{3}(n^2+2)\right]^2 n} \tag{3}$$

$$\tau_R \propto \frac{1}{f(\text{ED})} \frac{\lambda_0^2}{L} \tag{4}$$

where

$$L = \left[\frac{1}{3}\left(\left(n_{Y_2Si_2O_7} + (1-x)n_{\text{med}}\right)^2 + 2\right)\right]^2 \left(n_{Y_2Si_2O_7} + (1-x)n_{\text{med}}\right) \tag{5}$$

and where f(ED) is the oscillator strength for the electric dipole transition, λ_0 is the wavelength in vacuum, and n is the refractive index of the material.

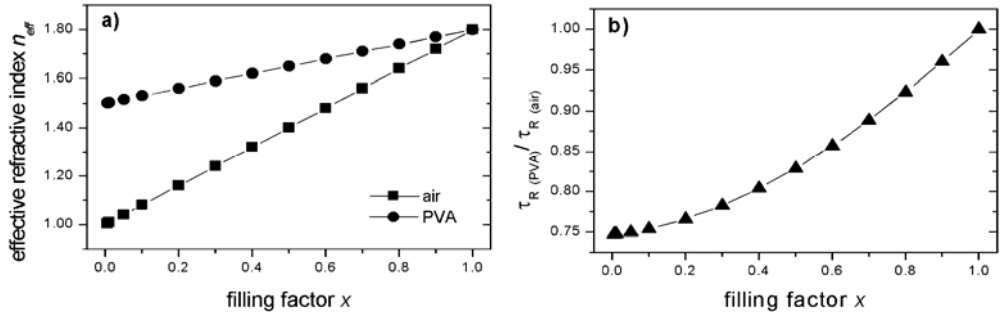

Fig. 7. Dependence of the calculated effective refractive index n_{eff} (a) and change in radiative lifetimes $\tau_{R(\text{PVA})}/\tau_{R(\text{air})}$ (b) on the filling factor x

The radiative lifetime should be lower for the composite material than for the nanocrystalline powder in air. Assuming that only L is a variable in Eq. (4) and that the surface areas of the powder nanocrystals PVA are the same, we can find how the radiative lifetime changes by changing n_{med} from 1 (n_{air}) to 1.5 (n_{PVA}). The calculated dependence of the effective refractive index n_{eff} and calculated relative change of radiative lifetimes $\tau_{R(\text{PVA})}/\tau_{R(\text{air})}$ on a filling factor x is plotted in Figure 7. It was estimated that the observed change in the luminescence lifetime of ~20% could correspond to $x \approx 0.4$.

4. Conclusions

The purpose of the present work was to obtain transparent polymer films with embedded nanocrystallite powder anti-Stokes luminophores, demonstrating efficient up-conversion luminescence under infrared excitation. Such nanocomposite films can be used for optoelectronic devices and security systems. As the nanocrystalline luminophores, yttria disilicate ($Y_2Si_2O_7$) doped with Yb and Er ions were chosen. The fabrication of Er,Yb:$Y_2Si_2O_7$:PVA polymer nanocomposite materials was described. Their morphology and optical transparency were determined. In particular, the up-conversion luminescence of Er^{3+} after exciting Yb^{3+} with an infrared laser diode was investigated. The up-conversion spectra of Er,Yb:$Y_2Si_2O_7$:PVA, manifested by two Er^{3+} luminescence transition bands in the red and green range, were similar to those measured for the nanocrystalline powder, in spite of the fact that the luminescence decay times were significantly decreased. The process was discussed in terms of the host effect enhancing the effective refractive index. A method for estimating the filling factor from relative changes in luminescence lifetimes for nanopowders in air and embedded in host materials was proposed.

Acknowledgements

This work was supported by KBN grant PBZ-KBN-095/T08/2003. We would like to thank Dr. M. Wołcyrz for the XRD measurements and Dr. P. Solarz for his help in the luminescence decay measurements.

References

[1] RAY S.S., OKAMOTO M., Prog. Polym. Sci., 28 (2003), 1539.
[2] KICKELBICK G., Prog. Polym. Sci., 28 (2003), 83.
[3] CHOI Y.Y., SOHN K.-S., PARK H.D., CHOI S.Y., J. Mater. Res. 16 (2001), 881.
[4] ZHANG Q.Y., PITA K., BUDDHUDU S., KAM C.H., J. Phys. D. App. Phys., 35 (2002), 3085.
[5] KANG Y.C., LENGGORO I.W., PARK S.B., OKUYAMA K., J. Solid State Chem., 146 (1999), 168.
[6] SCHEIFE H., HUBER G., HEUMANN E., BAR S., OSIAC E., Opt. Mater., 26 (2004), 365.
[7] SUYVER J.F., AEBISCHER A., BINER D., GERNER P., GRIMM J., HEER S., KRAMER K.W., REINHARD C., GUDEL H.U., Opt. Mater., 27 (2005), 1111.
[8] PODBIELSKA H., STRĘK W., Proc. SPIE 3314 (1998), 247.
[9] HRENIAK D., STRĘK W., OPALIŃSKA A., NYK M., WOŁCYRZ M., ŁOJKOWSKI W., MISIEWICZ J., J. Sol-Gel Sci. Techn., 32 (2004), 1.
[10] ABD EL-KADER K.A.M., ABDEL HAMIED S.F., J. Appl. Polym. Sci., 86 (2002), 1219.
[11] BRAUN M.M., PILON L., Thin Solid Films 496 (2006), 505.
[12] SCHEPS R., Prog. Quant. Electr., 20 (1996), 271.
[13] CHENG Z.X., ZHANG S.J., SONG F., GUO H.C., HAN J.R., CHEN H.C., J. Phys. Chem. Solids 63 (2002), 2011.
[14] CHEN X., NGUYEN T., LUU Q., DI BARTOLO B., J. Lumin. 85 (2000), 295.
[15] YANG H.S., HONG K.S., FEOFILOV S.P., TISSUE B.M., MELZER R.S., DENNIS W.M., J. Lumin., 83–84 (1999), 139.
[16] MELTZER R.S., HONG K.S., Phys. Rev. B, 61 (2000), 3396.
[17] SCHNIEPP H., SANDOGHDAR V., Phys. Rev. Lett., 89 (2002), 257403.

[18] VETRONE F., BOYER J.-C., COPOBIANCO J.A., SPEGHINI A., BETTINELLI M., Nanotechnology, 15 (2004), 75–81.
[19] KUMAR R., SINGH A.P., KAPOOR A., TRIPATHI K.N., Opt. Eng., 43 (2004), 2134.
[20] CHING W.Y., OUYANG L., XU Y.-N., Phys. Rev. B, 67 (2003), 245108.
[21] MELTZER R.S., FEOFILOV S.P., TISSUE B.M., YUAN H.B., Phys. Rev. B, 60 (1999), R14012.

Received 30 September 2005
Revised 21 February 2006